Electronic Thesis and Dissertation Repository

4-23-2019 10:00 AM

Towards on-line plan adaptation of unified intensity-modulated arc therapy using a fast-direct aperture optimization algorithm

Michael MacFarlane, *The University of Western Ontario*

Supervisor: Chen, Jeff Z., *The University of Western Ontario*
Joint Supervisor: Battista, Jerry J., *The University of Western Ontario*
A thesis submitted in partial fulfillment of the requirements for the Doctor of Philosophy degree in Medical Biophysics
© Michael MacFarlane 2019

Follow this and additional works at: https://ir.lib.uwo.ca/etd

Part of the Medical Biophysics Commons

Abstract

External beam radiotherapy (EBRT) plays a vital role in the treatment of cancer, with close to half of all cancer patients receiving EBRT at some point over their course of treatment. Although EBRT is a well-established form of treatment, there are a number of ways in which EBRT could still be improved in terms of quality and efficiency for treatment planning and radiation dose delivery. This thesis reports a series of improvements made to EBRT.

First, we developed and evaluated a new treatment planning technique called unified intensity-modulated arc therapy (UIMAT) which combines the optimization and delivery of rotational volumetric modulated arc therapy (VMAT) and fixed-gantry intensity-modulated radiation therapy (IMRT). When retrospectively compared to clinical treatment plans using VMAT or IMRT alone, UIMAT plans reduced the dose to nearby critical structures by as much as 23% without compromising tumour volume coverage. The UIMAT plans were also more efficient to deliver. The reduction in normal tissue dose could help lower the probability of treatment-related toxicities, or alternatively could be used to improve tumour control probability, via dose escalation, while maintaining current dose limits for organs at risk.

Second, we developed a new fast inverse direct aperture optimization (FIDAO) algorithm for IMRT, VMAT, and UIMAT treatment planning. FIDAO introduces modifications to the direct aperture optimization (DAO) process that help improve its computational efficiency. As demonstrated in several test cases, these modifications do not significantly impact the plan quality but reduced the DAO time by as much as 200-fold. If implemented with graphical processing units (GPUs), this project may allow for applications such as on-line treatment adaptation.

Third, we investigated a method of acquiring tissue density information from cone-beam computed tomography (CBCT) datasets for on-line dose calculations, plan assessment, and potentially plan adaptation using FIDAO. This calibration technique accounts for

patient-specific scattering conditions, demonstrated high dosimetric accuracy, and can be easily automated for on-line plan assessment.

Collectively, these three projects will help reduce the normal tissue doses from EBRT, improve the planning and delivery efficiency, and pave the way for application like on-line plan assessment and adaptive radiotherapy in response to anatomical changes.

Keywords:

Co-Authorship Statement

Chapter 2 was adapted from the published article entitled "Evaluation of unified intensity-modulated arc therapy for the radiotherapy of head-and-neck cancer" by Michael MacFarlane, Douglas A. Hoover, Eugene Wong, Nancy Read, David Palma, Varagur Venkatesan, Alex Hammond, Jerry J. Battista, and Jeff Z. Chen, *Radiotherapy and Oncology,* **119** (2): 331-336 (2016). Michael MacFarlane developed the planning algorithm, performed the retrospective planning study, performed the statistical analysis, and wrote the manuscript. Douglas Hoover, Eugene Wong, Jerry Battista, and Jeff Chen provided input on the planning study design and helped edit the manuscript. Nancy Read, David Palma, Varagur Venkatesan, and Alex Hammond provided the patient datasets and helped edit the manuscript.

Chapter 3 was adapted from the published article entitled "A fast inverse direct aperture optimization algorithm for intensity-modulated radiation therapy" by Michael MacFarlane, Douglas Hoover, Eugene Wong, Pedro Goldman, Jerry J. Battista, and Jeff Z. Chen, *Medical Physics*, **46** (3): 1127-1139 (2019). Michael MacFarlane developed the algorithms, performed the planning study, and wrote the manuscript. Douglas Hoover, Eugene Wong, Pedro Goldman, Jerry Battista, and Jeff Chen provided input on the algorithm and the study design and helped edited the manuscript.

Chapter 4 was adapted from an unpublished technical note entitled "A fast inverse direct aperture optimization algorithm for volume modulated arc therapy" by Michael MacFarlane, Douglas Hoover, Eugene Wong, Jerry J. Battista, and Jeff Z. Chen. Michael MacFarlane developed the algorithms, performed the planning study, and wrote the manuscript. Douglas Hoover, Eugene Wong, Jerry Battista, and Jeff Chen provided input on the algorithm and the study design and helped edited the manuscript.

Chapter 5 was adapted from the published article entitled "Patient-specific calibration of cone-beam computed tomography data sets for radiotherapy dose calculations and treatment plan assessment" by Michael MacFarlane, Daniel Wong, Douglas A. Hoover, Eugene Wong, Carol Johnson, Jerry J. Battista, and Jeff Z. Chen, *Journal of Applied*

Dedication

To my parents, Mary and James MacFarlane.

Acknowledgments

I would like to first and foremost thank my supervisors, Drs. Jeff Z. Chen and Jerry J. Battista. I am eternally grateful for the support and guidance that they have provided me over these years, and for having the confidence in me to pursue a medical physics career. I also would like to extend my gratitude to my advisory committee members, Drs. Michael Lock, Douglas Hoover, and Eugene Wong, for all their valuable time, thoughtful suggestion and clinical feedback on my work.

A sincere thank you to all of my collaborators over the years: Carol Johnson, Karl Bzdusek (of Philips Radiation Oncology group), Daniel Wong, Dr. Pedro Goldman (Ryerson University), Dr. Nancy Read, Dr. David Palma, Dr. Varagur Venkatesan, and Dr. Alex Hammond. Many of these projects would not have been possible if it weren't for their contribution.

I would like to extend my deepest gratitude to all the members in the Department of Physics and Engineering at the London Regional Cancer Program; as well as the staff, administrators and teachers in the Department of Medical Biophysics at the University of Western Ontario. I would like to particularly thank the CAMPEP director, Dr. Rob Stodilka, who has been a great mentor. I would also like to acknowledge the various sources of funding that have helped support this research and my graduate studies. This includes the London Regional Cancer Program; the London Health Research Institute (LHRI), Phillips Healthcare, and the Government of Ontario who provided funding through the Ontario Research fund (OCAIRO Project); and the Canadian Institutes for Health Research (CIHR).

Last of all, I would like to thank all my friends – both near and far – who have made these last few years special. In particular, Kevin Pichler, who has long been an inspiration to me and who is deeply missed. Finally, thank you to my parents, Mary and Jim; to my sisters, Katherine, Sarah, and Heather, and their wonderful families; and to my partner, Derek, for all their unconditional love, patience and support.

Table of Contents

List of Tables

List of Figures

List of Appendices

List of Units and Abbreviations (in order of use)

Gy	Gray (1 joule per kilogram)
EBRT	External Beam Radiotherapy
Linac	Linear Accelerator
MLC	Multileaf Collimator
3D	Three Dimensional
HU	Hounsfield Unit
CT	Computed Tomography
MRI	Magnetic Resonance Imaging
PET	Positron Emission Tomography
TPS	Treatment Planning System
DIR	Deformable Image Registration
GTV	Gross Tumour Volume
CTV	Clinical Target Volume
PTV	Planning Target Volume
IMRT	Intensity Modulated Radiation Therapy
VMAT	Volumetric Modulated Arc Therapy
OAR	Organ at Risk
CP	Control Point
MU	Monitor Unit
FMO	Fluence Map Optimization
DAO	Direct Aperture Optimization
CCC	Collapsed Cone Convolution
SVD	Singular Value Decomposition
DVH	Dose Volume Histogram
ROI	Region Of Interest
QA	Quality Assurance
CBCT	Cone-Beam Computed Tomography
GPU	Graphical Processing Unit
MCO	Multi-criteria Optimization
ART	Adaptive Radiotherapy
UIMAT	Unified Intensity Modulated Arc Therapy
FIDAO	Fast Inverse Direct Aperture Optimization
SS	Step-and-Shoot
RTOG	Radiation Therapy Oncology Group
QUANTEC	Quantitative Analyses of Normal Tissue Effects in the Clinic
CI	Conformity Index
CPU	Central Processing Unit
FIDO	Fast Inverse Dose Optimization
IPOPT	Interior Point Optimization
COIN-OR	Computational Infrastructure for Operations Research
CORT	Common Optimization for Radiation Therapy
NVBB	Non-Voxel-based Broad-Beam
SBRT	Stereotactic Body Radiation Therapy

SRS	Stereotactic Radiosurgery
reCT	Re-planning CT
PSC	Patient Specific Calibration
kVp	Kilovoltage Potential
FoV	Field of View
OBI	Onboard Imaging System
FDK	Feldkamp-Davis-Kress
MANOVA	Multivariate Analysis of Variance
ANOVA	Analysis of Variance
CI	Confidence Interval
DMPO	Direct Machine Parameter Optimization
DASSIM-RT	Dense Angularly Sampled and Sparse Intensity-Modulated Radiation Therapy
AMRT	Arc Modulated Radiation Therapy
IMAT	Intensity Modulated Arc Therapy

List of Symbols

$\bar{D}$	Mean Dose Metric
D_{max}	Max Dose Metric
D_x	Dose to x percent or volume (in cubic centimeters)
V_x	Volume (in percent) receiving x dose or more
γ	Index used in the gamma analysis Minimum radial distance between the measurement dose point and the calculation dose points
$\boldsymbol{d}_{xi}$	Dose calculation matrix Describes the dose deposited to voxel x by pencil beam i
τ_i	Fluence Map Describes pencil beam i's intensity
p_{ROI}	Penalty weight assigned to the region of interest's (ROI) objective
d_{ptv}	Dose prescribed to the PTV
$\boldsymbol{H}[f], \boldsymbol{\alpha}$	Hessian matrix of the objective function (f)
δ	Kronecker delta function
$\vec{\beta}$	Gradient vector of the objective function
$\vec{l}, \vec{w}$	Aperture MLC positions and weight, respectively
$\boldsymbol{T}_{jv}$	Transmission through pencil beam j by aperture v
Θ	Heaviside function
d_{min}	Minimum dose

Chapter 1 – Introduction

1.1 Cancer statistics

Cancer is a highly prevalent disease and a leading cause of death worldwide [1-5]. In 2018, the Canadian Cancer Society projects that about one in two Canadians will be diagnosed with cancer at some point in their lifetime, and about one in four Canadians will die with this disease [1]. Fortunately, the cancer mortality rates are declining in many countries – including Canada – due to earlier detection and intervention, greater access to treatment, and from advancements in cancer treatments, including radiation therapy [4,5].

1.2 Radiation Therapy Overview

Radiation therapy plays a vital role in the treatment of cancer, with more than half of all cancer patients receiving radiation therapy at some point over their course of treatment [3,5]. In radiation therapy, the patient is exposed to one or more sources of ionizing radiation (i.e. high-energy x-rays, gamma rays, and/or charged particles). This ionizing radiation can penetrate through the patient's body, damaging and killing cells along its trajectory [6,7]. The goal of radiation therapy is to preferentially deliver radiation to the tumour volume while minimizing the amount of healthy tissue exposed and collaterally damaged by treatment.

A commonly used metric in radiation therapy is the absorbed dose. Absorbed dose measures the amount of energy (in joules, J) that is deposited per unit mass of an absorber (in kilogram, kg), by ionizing radiation [6]. Absorbed dose is measured in the SI unit Gray (Gy), where 1 Gy = 1 J/kg. The higher the absorbed dose in a volume, the more likely that lethal cell damage will occur in that volume, and the more likely that cells within that volume will transform or perish [7]. Therefore, the goal of radiation therapy is to achieve a high absorbed dose in defined target regions containing cancerous tissue, and a lower absorbed dose in regions containing normal tissue.

Radiation treatments are often administered over multiple treatment sessions. The motivation for this fractionation comes from various radiobiological principles [7]. For

instance, healthy tissue can repair faster from radiation damage than most cancerous cells [7]. Therefore, by administering the treatment over multiple treatment sessions, we can offer the healthy tissue more repair than cancerous cells. Furthermore, between treatment sessions, the tumour volume can re-oxygenate, and its cells can enter into more radiosensitive phases of the cell division cycle. As a result, the tumour volume becomes more susceptible to radiation damage in future treatment sessions, and the therapeutic ratio can be improved with fractionated-radiotherapy. A typical radiation treatment will deliver 60 Gy to the tumour volume over 30 sessions (i.e. in 2 Gy / fraction over 30 fractions).

Radiation therapy can be administered in one of two ways: externally, through a treatment known as external beam radiotherapy (EBRT), or internally, through a procedure known as brachytherapy [6]. In brachytherapy, radioactive sources are permanently or temporarily implanted in the patient, within or in close contact with the tumour volume [6]. As the radionuclide decays, it emits ionizing gamma rays and/or charged particles capable of damaging the nearby cells [6,7]. By placing the radionuclides near or within the tumour volume, the absorbed dose is highest in the cancerous tissue and reduces rapidly in the distal healthy tissue. Due to the invasiveness of this procedure, brachytherapy is often only performed in a subset of patients where the surgical procedure is well tolerated or minimally invasive (e.g. cervical, esophageal, or localized prostate cancer) [6]. Instead, most cancer patients are treated using EBRT. This thesis will focus exclusively on EBRT. In EBRT, beams of high-energy x-rays or charged particles are generated by a medical linear accelerator and directed towards the patient's cancerous tissue [6]. While medical linear accelerators (also referred to as a linacs) can be used to deliver megavoltage electron or x-ray beams, this thesis will deal exclusively with x-ray beams. A medical linear accelerator and its treatment head (collimator) is shown in Figure 1.1. To reach deeply seated tumours, the x-ray beam must first travel through – and deposit dose into – healthy tissue. Due to the dosimetric properties of x-rays, more dose will be deposited in the shallow healthy tissue than in the deep-seated cancerous tissue [6]. To minimize the healthy tissue dose, EBRT treatments will use multiple cross-fired beams, delivered from various gantry, couch and collimator angles,

that intersect at the tumour volume. By doing this, less dose is deposited in the healthy tissue, while a high *cumulative* dose is deposited in the cancerous tissue. Components within the collimator, such as the jaws and multileaf collimator (MLC) shown in Figure 1.1, can also be used to attenuate and shape the beams. The plan beams can be optimized to limit normal tissue dose and to improve the cumulative dose received by the target volume [6]. In order to determine which beam configuration, beam shapes, and exposure times to use for each patient, a treatment planning procedure is required as described in the following section.

Figure 1.1: Picture of a linac [left] and the linac's treatment head (collimator) [right]. Note that these images have been recolored to help identify each component. [left] The patient lies on the treatment couch (orange) during treatment. Ionizing radiation is delivered from the gantry (green) towards the patient, as illustrated by the yellow cone. The gantry (and therefore the beam) can fully rotate around the patient, while the couch can be rotated, elevated, and repositioned as well. Some linacs possess onboard imaging capabilities for patient positioning and setup. The x-ray source and detector of this linac's imaging unit is highlighted blue and red, respectively. [right] The beam can be attenuated and shaped using the jaws (blue) and the multileaf collimator (MLC, purple) within the collimator of the linac. The rotation angle of the collimator can also be adjusted.

1.3 EBRT Treatment Process

The EBRT treatment planning process consists of the following major steps: (1) image acquisition, (2) delineation of target volumes and organs at risk (contouring), (3) beam selection, (4) plan optimization, (5) plan evaluation, (6) quality assurance, and (7) plan delivery. Details of each step that are relevant to this thesis, are provided in the following subsection.

1.3.1 Image Acquisition

Treatment planning begins by acquiring three-dimensional (3D) image sets of the patient. To calculate the absorbed dose from EBRT treatment in the patient, 3D maps of the tissue electron density (in electrons per cm^3) are needed [8-10]. These maps can be easily generated from the pixel values (Hounsfield Units (HU)) of x-ray computed tomography (CT) scans [9,10]. These CT scans are acquired in the intended treatment position and will include any immobilization equipment that will be for treatment. For instance, personalized immobilization masks are often used for patients with brain and head-and-neck cancer to hold their head in the same reproducible position during the CT scan and in each of the treatment sessions. These masks are securely fastened to the couch of the linac. Similarly, abdominal compressors may be used in patients with lung cancer to help suppress respiratory tumour motion during the CT scan and treatment. These CT scans are often referred to as the 'planning CT' or 'CT-sim' as they are used to plan and simulate the treatment.

In some cases, it may not be possible to differentiate healthy tissue from cancerous tissue on the planning CT images, as the borders of the tumour may not be well defined on this type of scan. Moreover, additional information such a metabolic activity or water diffusivity may be helpful for differentiating cancerous lesions from healthy tissue, staging the cancer, or visualizing nearby critical structures (e.g. hippocampus). Therefore, additional scans of the patient may be acquired using other imaging modalities such as magnetic resonance imaging (MRI) and positron emission tomography (PET) [11].

1.3.2   Contouring and Prescription

The image sets (planning CT, MRI, PET) of the patient are imported into a commercial treatment planning system (TPS). If MRI or PET scans were acquired of the patient, these image sets are co-registered with the patient's planning CT using rigid or deformable image registration (DIR) techniques [12]. The patient's tumour(s), organs, and healthy tissue are then delineated on the planning CT with the assistance of the co-registered MRI or PET scans [13]. The delineated tumour – as it is visible on the MRI, PET, and/or CT scan – is referred to as the gross tumour volume (GTV).

Cancerous lesions are typically encapsulated by microscopic disease that cannot be clearly visualized on MRI, PET, or CT scans. To ensure that all cancerous tissue is treated, a treatment margin is added to the GTVs. This expansion of the GTV is referred to as the clinical target volume (CTV) [13].

Some patients may have their gross tumour(s) surgically resected prior to radiation therapy. If no gross tumour is left behind from surgery, the tumour bed will be contoured instead and labelled as the CTV [13].

In some patients, there may be concerns that the disease has spread into the nearby lymphatic tissue; even when there is no clear GTV in these regions. In these cases, the lymphatic tissue may be delineated and treated prophylactically [13]. This is done to mitigate the risk of local reoccurrence and the risk of the disease spread (metastasis) to other regions of the body.

Lastly, a margin is added to the CTVs to account for the interfraction variability in patient positioning, intrafraction motion such as breathing, and the general uncertainties associated with treatment delivery. This expansion of the CTV is called the planning target volume (PTV). Each PTV is prescribed a specific absorbed dose level. Primary PTVs containing the GTV will be prescribed a high absorbed dose that will result in a high tumour control probability (e.g. 70 Gy). Meanwhile, PTVs containing the lymphatic tissue will typically be treated with a lower absorbed dose (e.g. 56 Gy). Finally, the

radiotherapy plan is normalized so that 95% of primary PTV is covered by 100% of the prescription dose.

1.3.3   Beam Selection

In this step, a treatment planner specifies what type of beam the linac will deliver (x-rays or electrons); the energy of each beam; the gantry, collimator, and couch angles of the beams; and how the linac will deliver this radiation. While there are many EBRT techniques available today, such as electron beams and 3D conformal radiotherapy, the majority of advanced EBRT treatments use x-ray beams delivered via one of two delivery techniques: fixed-gantry intensity-modulated radiation therapy (IMRT) and rotational volumetric modulated arc therapy (VMAT).

In fixed-gantry IMRT, the gantry, couch and collimator angles will remain fixed while the x-ray beam is being delivered. However, during beam delivery, the linac can alter the shape of the beam using the MLC and jaws shown in Figure 1.1 [14]. The MLC (and in some cases, jaws) can move while the beam is being delivered, in a technique known as sliding-window IMRT. Alternatively, the jaws and MLC can only be moved when the beam is shut off, known as step-and-shoot IMRT [6]. By modulating the shape of the beam during treatment, the net intensity (or fluence) delivered from each gantry angle is spatially varied, hence the name *intensity-modulated* radiation therapy. This intensity modulation can be used to improve PTV dose coverage and to minimize the dose to organs-at-risk (OAR) along the beam trajectories [6]. With the wise selection of gantry angles, IMRT can generally minimize the healthy tissue exposure and generate steep dose gradients to spare nearby critical structures, as demonstrated by the whole breast radiotherapy case in Figure 1.2.
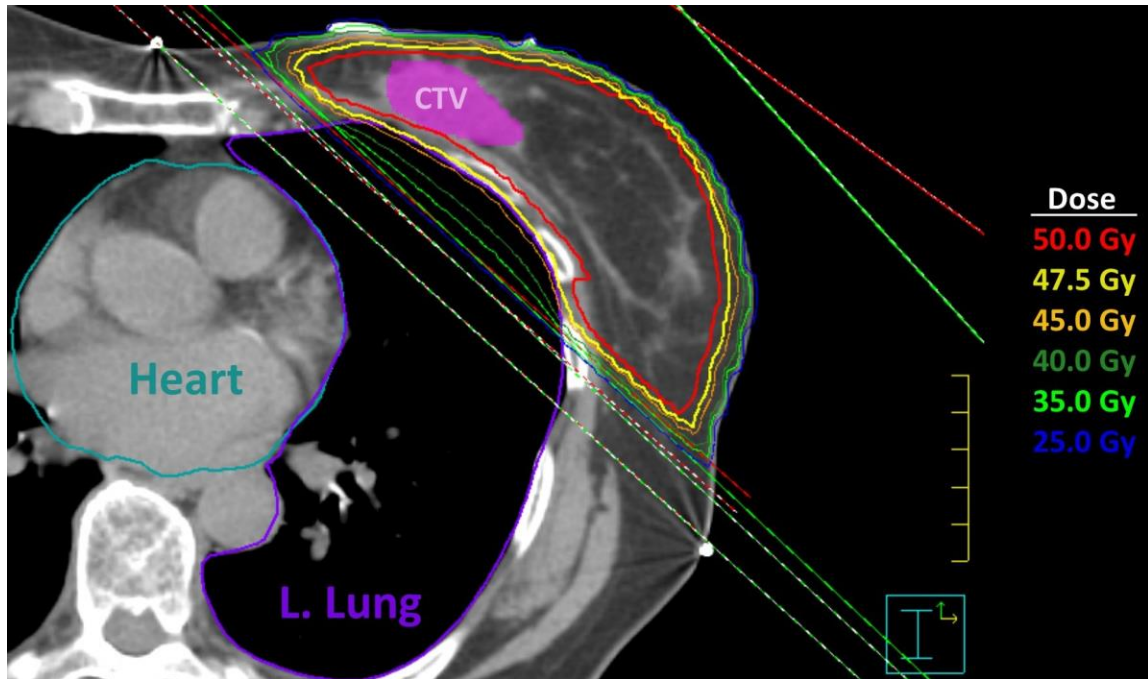
Figure 1.2: Axial view of a left-sided whole breast radiotherapy plan using two parallel and opposing IMRT beams. These beams are visualized as the red and green cones intersecting with the patient. With this beam setup, dose is limited primarily to the breast tissue. Meanwhile, the steep dose gradient (illustrated by the isodose lines, with each colour indicating the region receiving the corresponding dose (or more) in the legend on the right) generated by the beam edge is used to spare the nearby lung and heart.

In VMAT, radiation is delivered as the linac gantry continuously rotates the beam around the patient. Along the arc trajectory, the beam's dose-rate (i.e. the beam flux) and shape is modulated [15-16]. The treatment planner specifies the arcs to be used in the treatment plan and their arc range. While VMAT has limited intensity-modulation at any given gantry angle, the wide range of deliverable angles allows for more conformal dose distributions when treating quasi-spherical target volumes, like the prostate PTV shown in Figure 1.3. The wide range of deliverable angles in VMAT may result in a large volume of healthy tissue receiving low levels of dose, whereas the limited number of beams used by fixed-gantry IMRT may result in a smaller volume of healthy tissue being exposed but receiving higher levels of dose (as illustrated by the isodose lines in Figure 1.2). VMAT treatments are also typically more efficient to deliver than fixed-gantry IMRT.
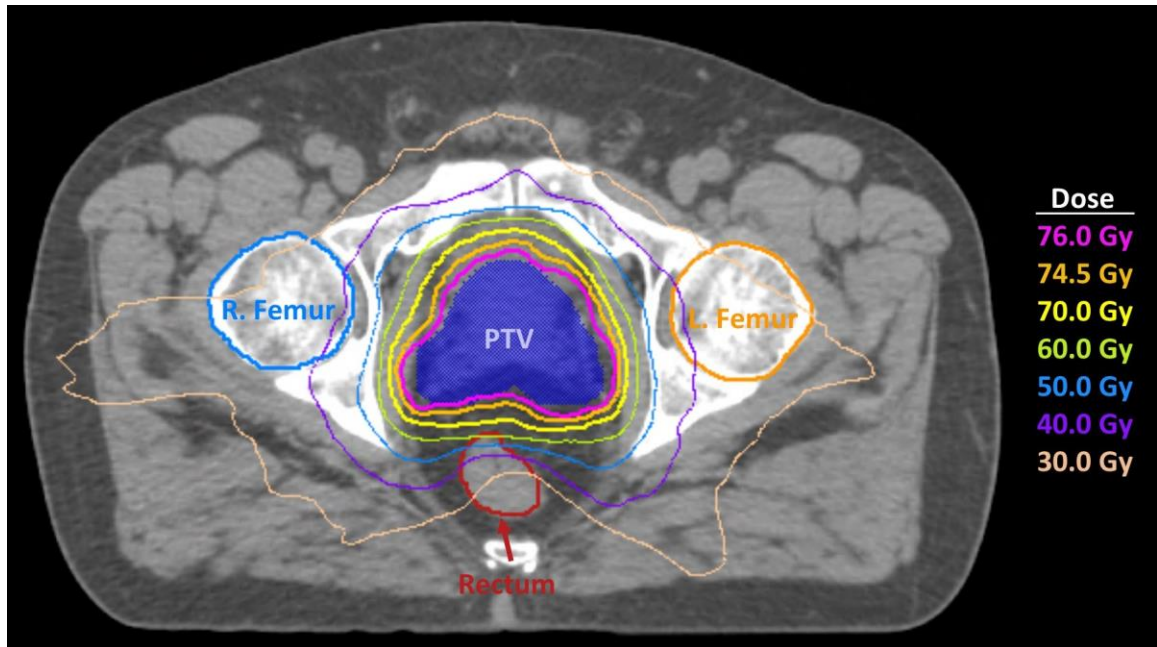
Figure 1.3: Axial view of a prostate radiotherapy plan using a single 360° VMAT arc (beam is not shown to improve visibility). With its wide range of deliverable angles, VMAT can produce dose distributions that are very conformal to the PTV.

1.3.4   Plan Optimization

It will be helpful for this section to first go over how medical linear accelerators are instructed to deliver IMRT and VMAT treatment plans. During delivery, a linac follows a series of programmed instructions known as control points (CP) [17]. Each CP specifies the position of each machine components (i.e. the couch position and angle, the gantry angle, the collimator angle, each jaw position, and each MLC leaf position) and the cumulative number of monitor units (MUs) that the machine is to deliver by the next CP. Note that the MU is a calibrated radiation unit that is measured by a monitoring ion chamber inside the linac head during beam delivery [6]. MU is calibrated to deliver a certain dose to a reference point in a water phantom under specific condition. Specifically, one MU is typically calibrated to deliver one cGy to a reference point in a water phantom at depth 5 cm and source to detector distance 100 cm for a beam with a field size of 10x10 cm^2. In step-and-shoot IMRT, the linac moves the components to the positions specified in the first CP. It then delivers the number of MUs specified for the first CP, while holding each machine component stationary. Once the MUs have been

delivered, the linac moves the components to the positions specified in the next CP, then delivers the MUs specified for that CP. Conversely, in VMAT and sliding-window IMRT, the linac moves the machine components between the positions specified in the first and second CP while delivering the number of MUs that are to be delivered by the second CP. It continues transitioning the components and delivering the MUs simultaneously until the last CP is reached.

The goal of plan optimization is to determine what the CPs parameters of the treatment plan should be. This process begins with the treatment planner creating a list of plan objectives (sometimes referred to as IMRT objectives). This list will consist of, for instance, a homogeneous prescribed absorbed dose to each PTV and a maximum dose permitted for each OAR. A weighting factor is also assigned to each of the planning objectives, indicating the relative importance of the objective.

When optimizing the treatment plan, each IMRT objective is represented by a scalar objective function [18]. This function reaches a global minimum value of zero when the 3D dose distribution of the plan satisfies the corresponding IMRT objective. The goal of plan optimization is to determine the CP parameters whose 3D dose distribution minimizes the weighted sum of these objective functions (i.e. that simultaneously satisfies as many of the IMRT objectives as possible). Unfortunately, these objective functions often have multiple minima, and so there is a risk that conventional deterministic optimization methods like gradient-descent could become trapped at a local minimum (i.e. at a sub-optimal solution). This issue can be avoided by using stochastic optimization techniques, such as simulated annealing, which can 'escape' from local minima [19]. However, stochastic optimization methods are typically much slower than deterministic methods, and so most commercial treatment planning systems use deterministic optimization algorithms (as described in Chapter 3 and Chapter 4). Briefly, these optimization algorithms perform the following IMRT/VMAT treatment planning procedure which will initialize the CP parameters as close to the global minimum of the objective function as possible.

IMRT plan optimization begins with fluence map optimization (FMO). FMO optimizes each beam's fluence map based on the planning objectives [20]. A more detailed summary of FMO can be found in Chapter 3.2.1. FMO tells us what the ideal beam fluence should be *after* a beam is delivered, but it does not tell us how many CPs are needed or what the CP parameters should be to generate the optimal fluence map. To get this CP information, an aperture-sequencing algorithm is executed on the optimized fluence maps [14]. These sequencing algorithms decompose the fluence map into a collection of segments, with each segment having a single homogeneous intensity. These segments can be easily converted into equivalent CP information. Usually, the number of CPs needed to faithfully recreate the optimal fluence map, is too high for delivery to be practical [19]. Therefore, sequencing algorithms are typically forced to approximate the ideal fluence map using a limited number of CPs. Due to this approximation, plan quality often degrades after aperture sequencing. To recoup this plan degradation, direct aperture optimization (DAO) are typically used [19,21-27]. These DAO algorithms iteratively optimize the MLC, jaw, and MUs values of each CP while also taking into consideration the delivery limitations of the specific linear accelerator. A more detailed introduction to DAO can also be found in Chapter 3.2.2. Some DAO algorithms optimize the aperture shapes after FMO and aperture sequencing [22], while others incorporate the aperture sequencing step into the FMO algorithm [23]. Both types of DAO use the same planning objectives as FMO. The result of these DAO algorithms is the CPs necessary for achieving the desired planning objectives.

The plan optimization algorithm used for VMAT treatment planning is dependent on the commercial TPS [16,28,29]. For this thesis, only the SmartArc VMAT planning algorithm is introduced [29]. Upon starting VMAT optimization, SmartArc performs FMO and aperture sequencing at fixed-gantry angles every 24 degrees between the user-specified starting and stopping angle. It then selects the two CPs with the highest number of open leaf pairs from each beam, while discarding all the rest of CPs. The selected CPs are then redistributed around their original gantry position. Additional CPs are then created between the selected and repositioned CPs, via linear interpolation, until a minimum angular spacing between consecutive CPs (typically 2° or 4°) is achieved. This

process is referred to as arc sequencing and is illustrate in Figure 1.4. DAO is then performed on the CPs of the VMAT arc, using the same planning objectives as before. Note, the DAO algorithms used for VMAT also incorporate any VMAT related delivery constraints, such as the maximum dose rate and gantry rotation speed.
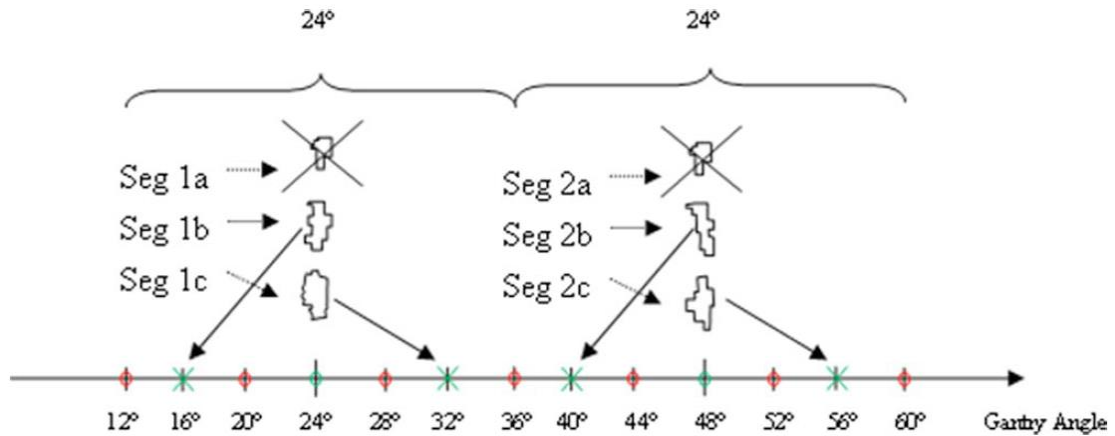
Figure 1.4: Illustration of the SmartArc planning process. FMO and aperture sequencing is performed at 24° increments. The two CPs with the highest number of open leaf pairs are selected from each beam, while the rest (CPs 1a & 2a) are discarded. The selected CPs are then repositioned along the arc (crosses). Additional CPs are generated via linear interpolation (circles) until a maximum distance between consecutive CPs (typically 4°) is achieved. This figure is reproduced from Bzdusek et al. [29], with permission from John Wiley and Sons (Appendix B.1).

The accuracy and efficiency of plan optimization relies heavily on the dose calculation algorithm that is used for plan optimization [10]. High dosimetric accuracy is needed so that the plan parameters are correctly optimized, and the optimization converges to the users-specified plan objectives. However, the dose calculation should be sufficiently fast for the optimization to complete in a practical amount of time. A common approach is to perform an accurate but less efficient dose calculation (e.g. collapsed cone convolution (CCC)) in the middle of the optimization. Then, during DAO, the algorithm uses a fast but less accurate dose engine (e.g. singular value decompositions (SVD)) to 'perturb' the dose distribution, based on the difference between the current plan parameters and plan parameters at the time of the accurate dose calculation [22,30]. This allows for fast

optimization without a substantial decrease in the dosimetric accuracy. At the end of optimization, a more accurate dose calculation algorithm such as CCC will be used again for the final dose computation of the plan.

1.3.5   Plan Evaluation

The plan quality will be evaluated once plan optimization is completed. The following tools are commonly used to assess EBRT plan quality: (1) the 3D dose distributions, (2) cumulative dose-volume histograms (DVH), and (3) dose metrics [6].

3D dose distributions and isodose lines (as shown in Figure 1.2 and Figure 1.3) can be used to evaluate the conformity of the dose distribution to the PTVs and doses to organs at risk.

Cumulative DVHs gives a compact summary of the 3D dose distribution for selected regions of interest (ROIs). Each DVH is plotted with the volume (absolute or relative) of a ROI on the vertical axis that is receiving more than or equal to the dose on the horizontal axis. An example of a DVH for a VMAT lung case is shown in Figure 1.5. Each of the PTV and OAR volumes are plotted separately on the DVH. Ideally, PTV DVHs will be as close to the top right as possible, indicating a high dose to as much of the PTV as possible. Conversely, all OAR DVHs should be bunched as close to the bottom left as possible, indicating that as little of the OAR is exposed to as low of a dose as possible. Many planning objectives, like the minimum and maximum dose, can be visualized with point markers on the DVH plot.
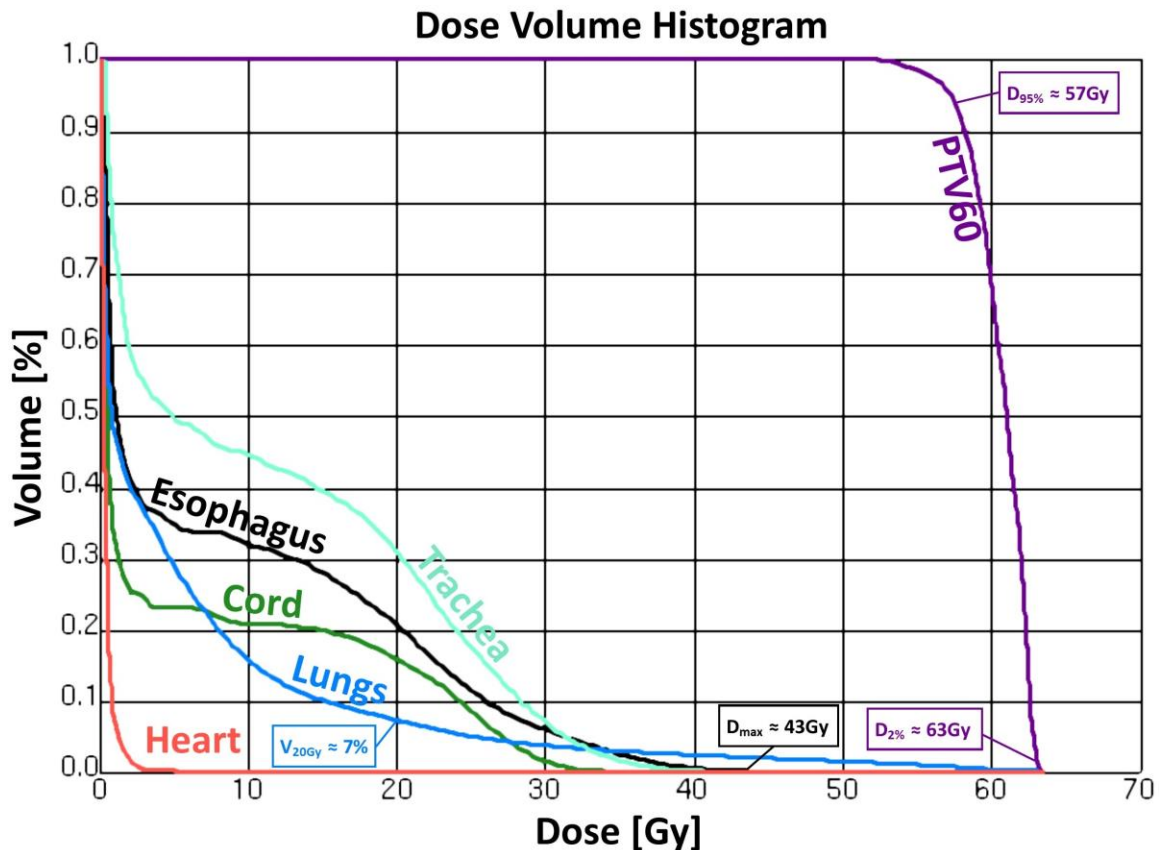
Figure 1.5: A sample dose-volume histogram from VMAT lung case. Common dose metrics for the lungs, esophagus and PTV are labelled.

Dose metrics are typically points on the DVH (e.g. the maximum dose as described above) or quantify some property about a DVH (e.g. conformity of the PTV coverage). Common dose metric include: the mean dose ($\overline{D}$), the maximum point dose (D_{max}), the minimum dose received by x volume in cubic centimeters ($D_{x\ cc}$), the minimum dose received by x % of the volume ($D_{x\%}$), and the percent volume receiving x dose or more ($V_{x\ Gy}$). Various dose metrics have been labelled on the DVH in Figure 1.5. Several dose metrics have been correlated with patient outcome data [31]. For instance, the lungs V_{20Gy} (the volume of the lungs receiving 20 Gy or more, shown in Figure 1.5) has been shown to be predictive of the patient developing pneumonitis after radiotherapy [32]. It is recommended that the lung V_{20Gy} be below 30% for treatment (it is about 7% in the plan shown in Figure 1.5).

13

If the dose distribution, the DVHs, or any of the dose metrics don't meet the clinical goal (e.g. the V_{20Gy} objective above), the plan will be re-optimized with modified planning objectives and/or objective weights. This cycle is repeated, in a trial-and-error approach, until a satisfactory treatment plan is achieved.

1.3.6   Quality Assurance

Once a satisfactory plan has been obtained, a series of quality assurance (QA) checks are performed to ensure that the treatment plan is safe, effective, and can be delivered accurately [33]. One QA test that will be relevant to this thesis is the patient-specific plan QA. First, the patient's treatment plan is delivered to a phantom that can measure and record the cumulative dose at numerous points in space. Let the spatial location of these measurements be denoted by, r_m, and the dose that is recorded at these points be, $D_m(r_m)$. The measured dose is then compared with the dose distribution calculated by the TPS, via a gamma analysis [34]. Specifically, let $D_c(r_c)$ be the dose calculated by the TPS at the location r_c. For each measurement point r_m, the gamma analysis will find the r_c that yields the lowest value to the function:

$$\Gamma(r_m, r_c) = \sqrt{\left(\frac{D_c(r_c) - D_m(r_m)}{\Delta D}\right)^2 + \left(\frac{d(r_c, r_m)}{\Delta d}\right)^2}.$$

That is,

$$\gamma(r_m) = \min_{r_c} \Gamma(r_m, r_c).$$

Note, $d(r_c, r_m)$ is the Euclidean distance between r_c and r_m, and ΔD and Δd are the dose difference and distance-to-agreement acceptance criteria set by the user. Any measurement points where $\gamma(r_m) > 1$ indicates a region where the measured dose and calculated dose disagree by more than the composite acceptance criteria. The gamma pass-rate gives the percentage of points where the measured dose agrees with calculated dose within the acceptance criteria. A common criteria is that 95% or more of the phantom dose measurements agree with the calculated dose, when the gamma analysis is performed with a 3% dose difference and 3 mm distance-to-agreement acceptance criteria.

1.3.7   Plan delivery

During a treatment session, the patient will be set up on the treatment couch (see Figure 1.1) in the same treatment position as the planning CT. Planar x-ray images or cone-beam computed tomography (CBCT) images may be acquired with linac's on-board imaging system (shown in Figure 1.1) and compared with the planning CT, to ensure accurate patient positioning [6]. Alternative image guidance technique like megavoltage x-ray CT, MRI, or optical guidance systems may also be used, if available, for patient positioning [35]. Once the patient is in the planned treatment position, the linac will deliver the patient's treatment plan. The patient will be treated with this plan, once or twice a day, Monday to Friday, for up to several weeks.

Over the course of treatment, the patient may undergo anatomical changes such as weight loss or tumour regression [36]. These changes may impact the effectiveness of the patient's immobilization equipment, leading to possible setup errors. Moreover, these changes may alter how radiation dose is distributed in the patient, leading to sub-optimal outcomes or unintended treatment-related side-effects [37].

To ensure that the patient receives adequate treatment, the patient may be referred for a new planning CT when their immobilization equipment is no longer effective or if large anatomical changes are observed between the patient's original planning CT and a CBCT acquired on-line. The patient's new planning CT will be contoured and registered with the patient's original planning CT. The patient's plan will then be 'copied' onto the new planning CT for dose calculation and plan assessment. If the plan quality is deemed inadequate, a new treatment plan will be generated on an accelerated timeline. The patient will then resume treatment with this new treatment plan. This is the process of treatment plan adaptation

1.4   Research Motivation

There are a number of ways in which the EBRT process described above, could be altered to improve plan quality, planning efficiency, and delivery efficiency.

First, EBRT treatments typically use either IMRT *or* VMAT delivery techniques. However, due to the complementary dosimetric properties of VMAT and IMRT, there could be an advantage to combining both VMAT and IMRT together in the same plan, as opposed to using one or the other. Currently, TPS do not support the *simultaneous* optimization of VMAT and IMRT. Instead, hybrid VMAT-IMRT treatment plans can only be created by optimizing the VMAT and IMRT portions separately [38]. This calls into question whether the treatment plan is truly optimal, as the plan parameters are never truly optimized together at the same time. Moreover, this planning approach will require that the IMRT and VMAT beams be delivered separately, making treatment delivery much less efficient.

Another source for improvement is the time spent optimizing IMRT, VMAT, as well as any future hybrid VMAT-IMRT treatment plans. Due to the computational complexity of the DAO problem, and the current trial-and-error approach to plan optimization, treatment planning can sometimes take several hours or even days to complete in some very complex cases. Furthermore, when there is limited time for treatment planning (e.g. for re-planning), sub-optimal treatment plans may be deemed acceptable for treatment, so that treatment delivery is uninterrupted. While newer TPS offer DAO algorithms that are implemented on fast parallelized graphical processing units (GPU), they are still not fast enough for applications like: (1) multi-criteria optimization [39,40] where numerous treatment plans are generated and compared, and (2) on-line adaptive radiotherapy (ART) where treatment re-planning is performed at the linear accelerator – while the patient is immobilized and awaiting treatment – using the 3D image sets acquired on-line (e.g. CBCT, MRI) [41,42].

Finally, even if fast DAO algorithms were available for on-line ART, another hurdle for ART is getting accurate electron density information from the 3D data sets acquired on-line, for dose calculations and plan optimization. For instance, MRI lacks a one-to-one correspondence between the voxel (3D pixel) intensity and electron density [43]. Meanwhile, patient-specific scattering conditions in CBCT can influence the accuracy of electron density maps [44]. Several methods of calibrating CBCTs for accurate dose calculation have been implemented, such as intensity-based deformable image

registration (DIR) algorithms that warp the accurate planning CT data onto the patient anatomy obtained from the CBCT. However, these DIR algorithms often introduce localized deformation errors which could potentially impact the densitometric, dosimetric and contouring accuracy within the region (see Chapter 5 for details). Therefore, more precise methods of acquiring electron density information from these image sets are still needed.

Even if fast DAO algorithms are unavailable for on-line ART, these electron density maps will be helpful for on-line dose calculations and plan assessment to judge whether treatment re-planning is truly necessary. Specifically, the effectiveness of the patient's immobilization equipment and the anatomical changes viewed on CBCT may not always be good indicators that treatment intervention and re-planning is necessary. It is not uncommon for a new planning CT to be acquired, contoured, and the plan copied over for plan assessment, only to find that the plan quality has not changed significantly to warrant re-planning. More importantly, these markers could be failing to identify patients that do need treatment intervention.

The overarching goal of this research is to address these critical areas of improvement in EBRT. Note that this is by no means an exhaustive list of how EBRT could be improved for gains in clinical outcomes. Many other areas for improving EBRT and patient outcome are currently under investigation at institutions around the world, such as the use of heavy-ion beams (e.g. proton, carbon-ion) [6], hypo-fractionation treatment regimens for the treatment of primary and oligometastatic cancer [45,46], and immunotherapy and its possible synergistic effects with radiation therapy [47], to name a few.

1.5 Research Hypothesis

We hypothesize that a fast plan optimization algorithm that unifies rotational volumetric modulated arc therapy and fixed-gantry intensity-modulated radiation therapy will improve radiotherapy plan quality, planning and delivery efficiency, and will provide a stepping-stone towards future on-line (interactive) plan adaptation.

1.6 Chapter Objectives

In Chapter 2, we evaluate a plan optimization algorithm called unified intensity-modulated arc therapy (UIMAT) on complex head-and-neck cases. This UIMAT algorithm simultaneously optimizes both rotational VMAT and fixed-gantry IMRT delivery techniques and combines their delivery. That is, UIMAT sequences the plan CPs such that, at delivery, the linac will deliver just like a VMAT beam. However, when this UIMAT beam reaches a gantry angles selected for IMRT delivery, it will halt gantry rotation and begin delivering like a step-and-shoot IMRT beam. After delivering this IMRT portion, the UIMAT beam will resume VMAT delivery. Delivery efficiency is improved by combining VMAT and IMRT's delivery in this way. Since this UIMAT algorithm was initially developed before entering this PhD program, details of this UIMAT plan optimization algorithm are provided in Appendix A.

In Chapter 3, a new DAO algorithm called fast inverse direct aperture optimization (FIDAO) is developed. FIDAO introduces modification to the equations used in DAO. These modifications greatly reduce the computation time of repeated calculations performed in the DAO process. By reducing the time of these calculations, DAO will be able to execute faster and improve the treatment planning efficiency, potentially allowing for on-line applications. Chapter 3 describes and evaluates this FIDAO algorithm for fixed-gantry IMRT treatment planning, while Chapter 4 evaluates FIDAO for rotational VMAT treatment planning.

In Chapter 5, a patient-specific CBCT calibration technique for on-line dose calculation and plan assessment is developed. By performing dose calculations and plan assessment on-line with these CBCT datasets, we can better differentiate the patient that truly require treatment re-planning from those who do not, saving resources and time. Moreover, with a fast DAO algorithm like the one developed in Chapter 3 & Chapter 4, the treatment re-planning could be potentially performed on-line with the calibrated CBCTs.

Finally, Chapter 6 summarizes the findings of this thesis, the potential clinical impact of these project, their limitations, future work, and specifically how these projects could

be combined as a package for an advanced on-line treatment planning and plan adaptation procedure. All of these developments are aimed at improving the clinical outcomes in patients treated with state-of-the-art radiation therapy.

1.7   References

1.   Canadian Cancer Statistics Advisory Committee. Canadian Cancer Statistics 2018. Toronto, ON: Canadian Cancer Society; 2018. Available at: cancer.ca/Canadian-Cancer-Statistics-2018-EN (accessed December 6, 2018).

2.   Siegel RL, Miller KD, and Jemal A. Cancer statistics, 2018. *CA: A Cancer Journal for Clinicians* 2018; **68** (1): 7-30.

3.   National Cancer Institute. Radiation Therapy and You: Support for People with Cancer. Available at: https://www.cancer.gov/publications/patient-education/radiationttherapy.pdf (2016) (accessed December 13, 2018)

4.   Bray F, Ferlay J, Soerjomataram I, Siegel RL, Torre LA, and Jemal A. "(2018), Global cancer statistics 2018: GLOBOCAN estimates of incidence and mortality worldwide for 36 cancers in 185 countries." *CA: A Cancer Journal for Clinicians* 2018; **68** (6): 394-424.

5.   Gelband, H., P. Jha, R. Sankaranarayanan, and S. Horton, editors. 2015. Cancer. Disease Control Priorities, third edition, volume 3. Washington, DC: World Bank. doi:10.1596/978-1-4648-0349-9.

6.   Khan F. *The Physics of Radiation Therapy.* 3rd ed. Philadelphia, PA: Lippincott Williams & Wilkins Inc; 2003.

7.   Hall E and Giaccia A. Radiobiology for the Radiologist. 7th ed. Philadelphia, PA. Lippincott Williams & Wilkins Inc; 2012.

8.   Papanikolaou N, Battista J, Boyer A, *et al.* Tissue inhomogeneity corrections for megavoltage photon beams. AAPM Report No 85; Task Group No. 85; Committee Task Group No. 65.

9.   Saw CB, Loper A, Komanduri K, Combine T, Huq S, and Scicutella C. Determination of CT-to-density conversion relationship for image-based treatment planning systems. *Med Dosim* 2005; 30:145-8.

10. Battista JJ, Chen JZ, Sawchuk S, Hajdok G. Introduction to megavoltage x-ray dose computation algorithms. 1st ed. Boca Raton, FL. Taylor & Francis Group; 2019.

11. Prescribing, Recording, and Reporting Photon-Beam Intensity-Modulated Radiation Therapy (IMRT): Contents, Journal of the International Commission on Radiation Units and Measurements, Volume 10, Issue 1, 1 April 2010, Pages NP, https://doi.org/10.1093/jicru/ndq002.

12. Brock, K. K., Mutic, S., McNutt, T. R., Li, H. and Kessler, M. L. (2017), Use of image registration and fusion algorithms and techniques in radiotherapy: Report of the AAPM Radiation Therapy Committee Task Group No. 132. Med. Phys., 44: e43-e76.

13. Burnet NG, Thomas SJ, Burton KE and Jefferies SJ. Defining the tumour and target volumes for radiotherapy. *Cancer Imaging* 2004; **4**: 153–161.

14. Bortfeld TR, Kahler DL, Waldron TJ, Boyer AL. X-ray field compensation with multileaf collimators. *Int J Rad Oncol Biol Phys* 1995; **28** (3): 723-30.

15. Yu C. Intensity-modulated arc therapy with dynamic multileaf collimation: an alternative to tomotherapy. *Phys Med Biol* 1995; **40** (9): 1435-49.

16. Otto K. Volumetric modulated arc therapy: IMRT in a single gantry arc. *Med Phys* 2008; **35** (1): 310-317.

17. NEMA PS3 / ISO 12052, Digital Imaging and Communications in Medicine (DICOM) Standard, National Electrical Manufacturers Association, Rosslyn, VA, USA (available free at http://medical.nema.org/)

18. Bortfeld T. Optimized planning using physical objectives and constraints. *Sem Rad Oncol* 1999; **9**(1): 20-34.

19. Shepard DM, Earl MA, Li XA, Naqvi S, and Yu C. Direct aperture optimization: A turnkey solution for step-and-shoot IMRT. *Med. Phys.* 2002; **29** (6): 1007-18.

20. Webb S. Optimizing the planning of intensity-modulated radiotherapy. *Phys Med Biol* 1994; **39**(12): 2229-46.

21. Li Y, Yao J, and Yao D. Genetic algorithm based deliverable segments optimization for static intensity-modulated radiotherapy. *Phys. Med. Biol.* 2003; **48** (20): 3353-74.

22. Hårdemark B, Liander A, Rehbinder H, and Löf J. P^{3}IMRT. Direct machine parameter optimization. *Pinnacle white paper*, Nr. 4535 983 02483, Philips (2004).

23. Romeijn HE, Ahuja RK, Dempsey JF, and Kumar A. A column generation approach to radiation therapy treatment planning using aperture modulation. *SIAM J. Optim.* 2005; **15** (3): 838-62.

24. Men C, Romeijn HE, Taşkin ZC, and Dempsey JF. An exact approach to direct aperture optimization in IMRT treatment planning. *Phys. Med. Biol.* 2007; **52** (24): 7333-52.

25. Carlsson F. Combining segment generation with direct step-and-shoot optimization in intensity-modulated radiation therapy. *Med. Phys.* 2008; **35** (9): 3828-38.

26. Men C, Jia X, and Jiang SB. GPU-based ultra-fast direct aperture optimization for online adaptive radiation therapy. *Phys. Med. Biol.* 2010; **55** (15): 4309-19.

27. Cassioli A and Unkelbach J. Aperture shape optimization for IMRT treatment planning. *Phys. Med. Biol.* 2012; **58** (2): 301-18.

28. Unkelbach J, Bortfeld T, Craft D, *et al.* Optimization approaches to volumetric modulated arc therapy planning. *Med Phys* 2015; **42**(3): 1367-77.

29. Bzdusek K, Friberger H, Eriksson K, Hårdemark B, Robinson D, and Kaus M. Development and evaluation of an efficient approach to volumetric arc therapy planning. *Med Phys* 2009; **36**(6): 2328-2339.

30. McNutt T. Dose calculations – collapsed cone convolution and delta pixel beam. *Pinnacle White Paper* 2007, Nr. 4535 983 02474/870.

31. Marks LB, Yorke ED, Jackson A, *et al.* Use of Normal Tissue Complication Probability Models in the Clinic. Int. J. Radiat. Oncol. Biol. Phys. 2010;76:S10-9.

32. Palma DA, Senan S, Tsujino K, *et al.* Predicting radiation pneumonitis after chemoradiation therapy for lung cancer: an international individual patient data meta-analysis. *Int J Radiat Oncol Biol Phys* 2013; **85**(2): 444-50.

33. Hartford AC, Palisca MG, Eichler TJ, *et al.* American Society for Therapeutic Radiology and Oncology (ASTRO) and American College of Radiology (ACR) Practice Guidelines for Intensity-Modulated Radiation Therapy (IMRT). *Int J Radiat Oncol Biol Phys* 2009; **73**(1): 9-14.

34. Low D, Harms H, Mutic S, Purdy J. A technique for the quantitative evaluation of dose distributions. *Med Phys.* 1998; **25**(5): 656-61.

35. Alaei P, Ding GX. AAPM Monograph No. 39. Image Guidance in Radiation Therapy: Techniques, Accuracy and Limitations. Madison, WI: Medical Physics Publishing Inc; 2018.

36. Barker JL Jr, Garden AS, Ang KK, et al. Quantification of volumetric and geometric changes occurring during fractionated radiotherapy for head-and-neck cancer using an integrated CT/linear accelerator system. *Int J Radiat Oncol Biol Phys* 2004; **59**(4): 960-70.

37. Hansen EK, Bucci MK, Quivey JM, Weinberg V, and Xia P. Repeat CT imaging and replanning during the course of IMRT for head-and-neck cancer. *Int J Radiat Oncol Biol Phys* 2006; **64**(2): 355-62.

38. Gevaert T, Engels B, Garibaldi C, *et al.* Implementation of HybridArc treatment technique in preoperative radiotherapy of rectal cancer: dose patterns in target lesions and organs at risk as compared to helical Tomotherapy and RapidArc. *Radiat Oncol* 2012; **7**:120.

39. Monz M, Küfer KH, Bortfeld TR, Thieke C. Pareto navigation: algorithmic foundation of interactive multi-criteria IMRT planning. *Phys Med Biol* 2008; **53**(4): 985-98.

40. Bokrantz R. Multicriteria optimization for managing tradeoffs in radiation therapy treatment planning (Doctoral Disertation). Retrieved from: https://www.raysearchlabs.com/globalassets/about-overview/media-center/wp-re-ev-n-pdfs/publications/doctoral-thesis-multicriteria-optimization_rasmus_bokrantz_2013.pdf.

41. Lim-Reinders S, Keller BM, Al-Ward S, Sahgal A, and Kim A. Online adaptive radiation therapy. *Int J Rad Oncol Biol Phys* 2017; **99**(1): 994-1003.

42. Schwartz DL, Garden AS, Shah SJ, *et al.* Adaptive radiotherapy for head and neck cancer—Dosimetric results from a prospective clinical trial. *Radiother Oncol* 2017; **106**(1): 80-4.

43. Edmund JM and Nyholm T. A review of substitute CT generation for MRI-only radiation therapy. *Radiat Oncol* 2017; **12**: 28.

44. Richter A, Hu Q, Steglich D, et al. Investigation of the usability of conebeam CT data sets for dose calculation. *Rad Oncol* 2008; 3:42.

45. Baumann P, Nyman J, Hoyer M, et al. Outcome in a prospective phase II trial of medically inoperable stage I non-small-cell lung cancer patients treated with stereotactic body radiotherapy. *J Clin Oncol* 2009; **27**(20): 3290-6.

46. Palma DA, Olson RA, Harrow S, et al. Stereotactic ablative radiotherapy versus standard of care palliative treatment in patients with oligometastatic cancers (SABR-COMET): a randomised, phase 2, open-label trial. *The Lancet* 2019; (In Press).

47. Schoenhals JE, Seyedin SN, Tang C, et al. Preclinical Rationale and Clinical Considerations for Radiotherapy Plus Immunotherapy: Going Beyond Local Control. *Cancer J* 2016; **22**(2): 130-7.

Chapter 2 – Evaluation of unified intensity-modulated arc therapy (UIMAT) for the radiotherapy of head-and-neck cancer

This chapter was adapted from the published article entitled "Evaluation of unified intensity-modulated arc therapy for the radiotherapy of head-and-neck cancer" by Michael MacFarlane, Douglas A. Hoover, Eugene Wong, Nancy Read, David Palma, Varagur Venkatesan, Alex Hammond, Jerry J. Battista, and Jeff Z. Chen, Radiotherapy and Oncology, 119 (2): 331-336 (2016). Permission to reproduce this article was granted by Elsevier and is provided in Appendix B.2. Supplemental tables and figures for this chapter are provided in Appendix C.

2.1 Introduction

Volumetric modulated arc therapy (VMAT) and fixed-gantry intensity-modulated radiation therapy (IMRT) are two commonly used external beam radiotherapy techniques for the treatment of cancers. Although these two delivery modalities are often treated in practice and literature as disparate or competing techniques, they are in fact both mechanically and dosimetrically complementary to each another.

The fixed-angle delivery used in IMRT allows for the creation of steep dose gradients at the field edges and highly modulated intensity patterns from each beam direction. With the wise selection of beam orientations, substantial sparing of select organs at risk (OAR) is possible with this technique [1,2]. However, for more rotationally symmetric target volumes, a larger number of beams may be required to achieve sufficient dose coverage and conformity while still sparing the surrounding OARs, resulting in reduced delivery efficiency. In such cases, the rotational delivery of VMAT is preferred as the wide range of deliverable angles can create very conformal dose distributions in a timely and efficient manner [3-7]. However, the requirements of continuous gantry motion and high delivery efficiency limit the degree of intensity modulation achievable at any given beam angle.

Many groups have demonstrated that the combination of IMRT and VMAT within a single plan provides a therapeutic advantage over treatments using either IMRT or

VMAT alone, as it utilizes the dosimetric advantages of both techniques [8-13]. This could be particularly advantageous in complex sites such as the head and neck where, in general, no consistent dosimetric advantage is observed between VMAT and IMRT [14]. It should be noted that with these previous hybrid techniques, IMRT and VMAT have not been fully integrated during either the inverse-optimization or beam delivery process.

Recently, our group developed a method called unified intensity-modulated arc therapy (UIMAT) which permits the simultaneous inverse optimization and concurrent delivery of VMAT and IMRT in a single arc [15]. Specifically, during the arc delivery, the gantry rotation can be reduced to a near-stop in order to deliver IMRT beam segments at opportune gantry angles. Details of this UIMAT algorithm can be found in Appendix A. This current study evaluates the potential benefit of UIMAT for the radiotherapy of complex head-and-neck cancer, compared to strictly VMAT or IMRT treatment plans. This site was selected based on promising preliminary results obtained in the previous feasibility study [15].

2.2 Methods and materials

Thirty previously treated head-and-neck cases were arbitrarily selected for this study. Fifteen of these cases were treated with dual-arc VMAT while the other fifteen cases were treated with a variable number of step-and-shoot (SS) IMRT beams. No factors related to the patient, primary disease site, or the prescribed dose was considered during the selection. A summary of the selected cases is provided in Supplementary Table 2.1.

UIMAT plans were generated for each patient using custom scripts developed for Pinnacle^3 v9.6 Radiation Therapy Planning System (Philips Healthcare, Fitchburg, USA). Technical details of the UIMAT method were previously described by Hoover et al. [15] and can be found in Appendix A however, the method can be roughly divided into five stages:

(1) Fluence Map Optimization: Multiple static beams are evenly distributed along the arc range and their fluences are optimized.

(2) MLC Sequencing: Optimized fluences are converted into deliverable MLC segments.

(3) UIMAT Sequencing (Re-assignment): Deliverable beams are sequenced via a script into VMAT or IMRT phases based on the number of MLC segments in a beam. Beams with fewer segments are converted to VMAT phases, while beams with more segments are converted to IMRT phases with near-constant gantry angles as shown in Figure 2.1.

(4) Direct Aperture Optimization (DAO): Both VMAT and IMRT phases are optimized simultaneously using Pinnacle's DAO algorithm.

(5) Unification: The optimized VMAT and IMRT phases, which are treated as separate beams within Pinnacle, are merged by script into a single UIMAT arc for final dose calculation and delivery.
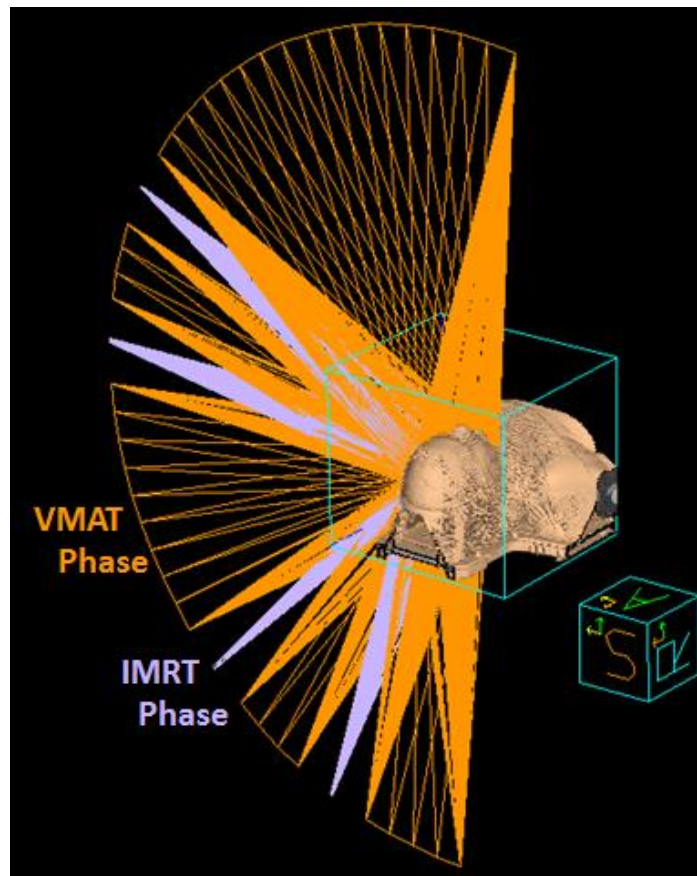
Figure 2.1: Illustration showing IMRT phases (lavender) and VMAT phases (orange) generated by the UIMAT script.

All UIMAT plans were created by a single planner (MM) and treatment planning times were recorded. Planning objectives for each UIMAT plan were copied from the clinical plan and set so that 95% of the planning target volume (PTV) would receive at least 95% of the prescription dose, while OAR doses were kept as low as achievable. Without exception, all OAR doses in both clinical and UIMAT plan were kept below our institutional standards, which originate from recommendations by Radiation Therapy Oncology Group (RTOG) clinical trials (RTOG 0225, 0513, 0522, 0615, and 0619), and Quantitative Analyses of Normal Tissue Effects in the Clinic (QUANTEC) guidelines [16].

UIMAT plans were optimized using the same (or very similar) objectives as the clinical plans. OAR objectives were set to reduce global OAR doses as opposed to the dose to any specific endpoint. Individual dose objectives were made more stringent if their relative contribution to the total objective function approached zero. In this way, the dose to all OARs was pushed as low as possible, in an unbiased manner. No explicit attempt was made to surpass the clinical plan; rather, UIMAT optimization was continued until the plan reached its highest potential. This is similar to how our clinical cases are planned.

The completed UIMAT plans were then evaluated against the clinically delivered plans in terms of target volume coverage, conformity index (CI), as well as clinically relevant OAR dose metrics. Wilcoxon signed rank tests were performed in SPSS (IBM Corp., Armonk, USA) to test for statistically significant differences between the UIMAT plans and the clinically delivered plans. The threshold for statistical significance was set to 5%. For plans with multiple PTVs (each having a different dose level), the average of a PTV metric was used in the analysis. For instance, if a plan had a PTV_{70Gy} with a mean dose of 102% (relative to 70 Gy), and a PTV_{56Gy} with a mean dose of 110% (relative to 56Gy), then the PTV mean dose used in the analysis would be 106%.

The conformity index used here is similar to the one introduced by Oozeer *et al.* [17]:
$$CI = (Cover\ factor) \times (Spill\ Factor)$$

$$= \left(\frac{V_{95}(PTV)}{V_{PTV}} \right) \times \left(\frac{V_{95}(PTV)}{V_{95}(Body)} \right) \qquad (1)$$

where $V_{95}(PTV)$ and $V_{95}(Body)$ are the volumes of the PTV and body, respectively, receiving at least 95% of the prescription dose, and V_{PTV} is the volume of the PTV. This equation was defined initially for a single dose level. To handle the case where multiple dose levels exist, the PTV volume with a lower prescription dose will also include all higher dose PTV volumes. For example, for a plan with PTV_{70Gy}, PTV_{63Gy}, and PTV_{56Gy}, to calculate the conformity index for the PTV with the lowest prescription dose (56 Gy), the PTV in equation (1) will be the union of the three PTV volumes.

Treatment plans were validated with an ArcCheck phantom (Sun Nuclear Corp., Melbourne, USA), using a TrueBeam linear accelerator (Varian Medical Systems, Palo Alto, USA) operating in clinical mode. Absolute dose distributions were compared between plans and ArcCheck measurements, using gamma parameter thresholds of 3% dose difference and 3 mm distance-to-agreement [18]. Delivery times were also measured during the ArcCheck delivery.

2.3 Results

The median (range) time required to generate a UIMAT plan was 3 (1.5-6) hours, which is comparable to the typical clinical planning time logged at our institution. Dosimetric comparisons for individual VMAT and IMRT cases are tabulated respectively in Supplementary Table 2.2 and Supplemental Table 2.3 (available online at www.thegreenjournal.com). In Table 2.1, median and ranges of the target and OAR dose metrics are compared for UIMAT plans against the stand-alone clinical IMRT plans, VMAT plans, and both clinical IMRT or VMAT plans.

Conformity indices were found to be lower in IMRT and UIMAT when compared to VMAT. A slight improvement in the dose coverage (D95) was observed for UIMAT relative to the IMRT (98.0% vs 96.7%, respectively, $p < 0.01$), but not when comparing UIMAT to the VMAT (98.2% vs 98.0%, respectively, $p = 0.70$). The mean PTV doses were slightly higher in UIMAT relative to VMAT (102.3% vs 101.5%, respectively, $p < 0.01$) and to IMRT (102.2% vs 101.8%, respectively, $p = 0.01$).

Median OAR dose metrics were universally reduced by the application of UIMAT. On average, OAR max doses were reduced by 5.4 Gy when compared to VMAT, and 5.3 Gy when compared to IMRT. Similarly, OAR mean doses were reduced, on average, by 2.5 Gy when compared to VMAT, and 3.9 Gy when compared to IMRT. All dose metrics were significantly reduced with the exception of the mean larynx and mean parotid doses when compared to VMAT. Average OAR dose-volume histograms are shown in Figure 2.2. Average OAR dose-volume histograms between just the VMAT and UIMAT techniques, as well as between IMRT and UIMAT techniques, are provided in Supplemental Figure 2.1. Sample dose distributions of two representative cases are shown in Figure 2.3.

In terms of deliverability, a significant reduction of the median delivery time was observed for UIMAT plans compared to the IMRT plans (147 s vs 269 s, $p = 0.001$), while no significant difference was observed between UIMAT and VMAT median delivery times (135s vs 168s, $p = 0.39$). A significant reduction in median monitor units (MU) was observed for UIMAT compared to IMRT (449 MU vs 596 MU, $p < 0.01$) and to VMAT (486 MU vs 635 MU, $p < 0.01$). Median IMRT QA pass rates were found to be significantly lower with UIMAT when compared to VMAT (97.5% vs. 98.8 %, $p = 0.03$) and IMRT (97.6 % vs. 99.2 %, $p = 0.02$).
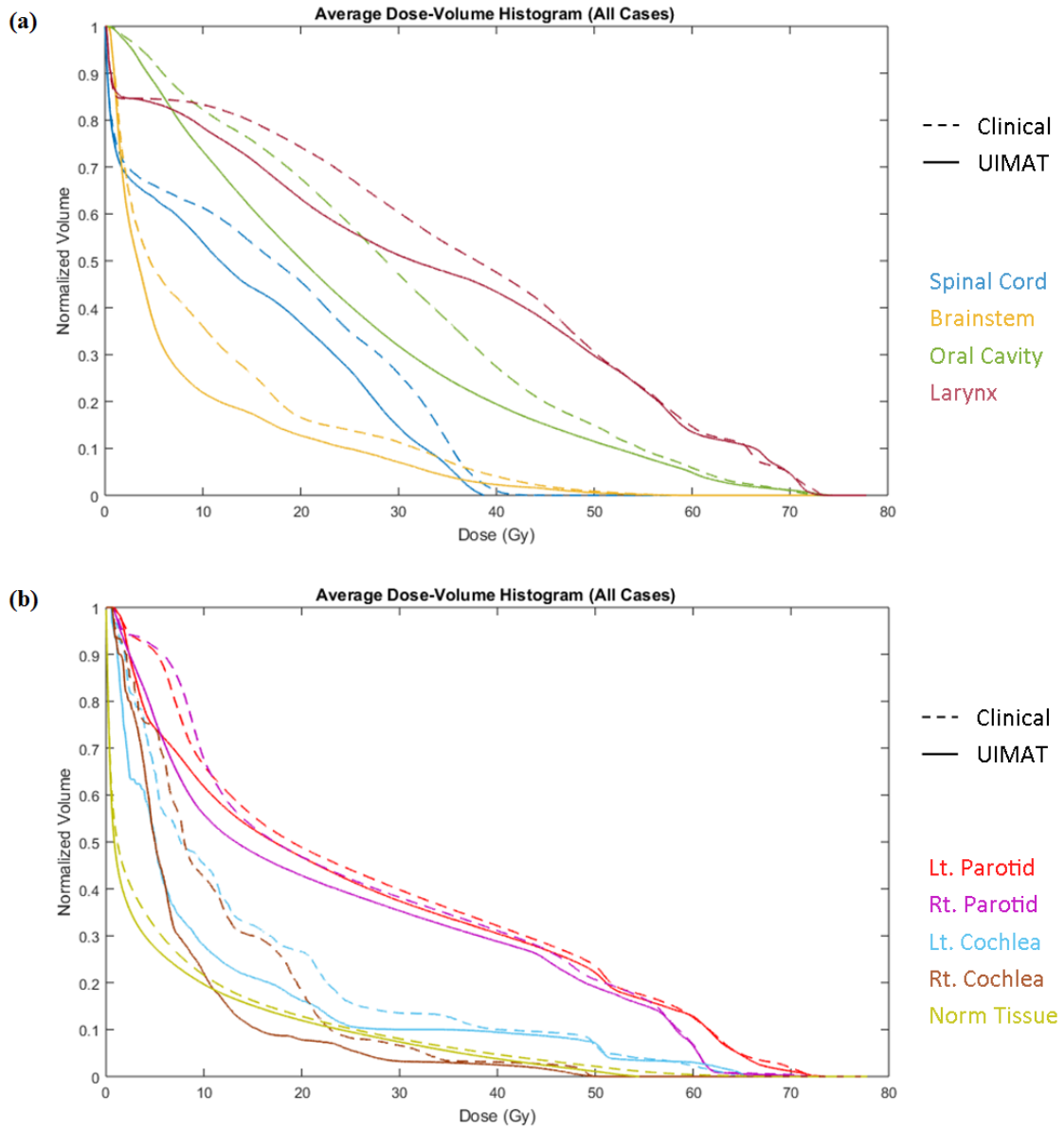
Figure 2.2: Comparison of average DVHs for various organs at risk. The clinical average DVH is plotted with the dashed line while the UIMAT average DVH is plotted with a solid line.

Table 2.1: Median (Min, Max) metric value between our UIMAT plans and the clinically delivered plans. Summaries are provided for VMAT cases (patients 1 – 15), IMRT cases (patients 16 – 30), and all cases. PTV mean doses and D95s (dose to 95% of the PTV) are given as percentages of the prescribed dose to the PTV. Reported max dose is the dose to 2% of the volume. Statistically significant differences are indicated by *.

Region of Interest	Metric	VMAT Only (Cases: 1-15)			IMRT Only (Cases: 16-30)			All Cases (Cases: 1-30)		
		VMAT	UIMAT	P	IMRT	UIMAT	P	Clinical	UIMAT	P
PTV	CI	0.73 (0.51,0.92)	0.70 (0.46, 0.87)	0.003*	0.67 (0.15,0.81)	0.67 (0.14, 0.83)	0.256	0.69 (0.15,0.92)	0.69 (0.14, 0.87)	0.086
	Mean (%)	101.5 (100.7,104.3)	102.3 (100.7, 105.6)	0.001*	101.8 (100.3,104.6)	102.2 (101.3, 104.3)	0.011*	101.7 (100.3,104.6)	102.3 (100.7, 105.6)	< 0.001*
	D95 (%)	98.0 (95.8,100.8)	98.2 (94.9, 100.2)	0.695	96.7 (94.9,98.7)	98.0 (95.6, 99.5)	0.004*	97.5 (94.9,100.8)	98.1 (94.9, 100.2)	0.01*
Norm. Tiss.	Mean (Gy)	6.4 (1.0, 11.2)	6.2 (1.0, 10.5)	0.691	7.4 (4.2, 13.4)	7.4 (3.5, 13.8)	0.069	7.2 (1.0. 13.4)	7.2 (1.0, 13.8)	0.086
Oral Cavity	Mean (Gy)	29.2 (4.7, 44.0)	21.3 (3.0, 43.0)	0.002*	33.9 (14.0, 61.3)	27.5 (10.0, 57.7)	0.001*	30.3 (4.7, 61.3)	23.2 (3.0, 57.7)	< 0.001*
Lt. Parotid	Mean (Gy)	25.3 (2.0, 43.9)	22.6 (2.0, 44.3)	0.173	29.1 (3.4, 52.0)	26.7 (2.6, 48.3)	0.005*	28.0 (2.0, 52.0)	26.1 (2.0, 48.3)	0.001*
Rt. Parotid	Mean (Gy)	27.2 (1.3, 60.9)	25.5 (1.1, 60.8)	0.071	27.2 (4.7, 58.6)	18.4 (2.7, 58.3)	0.001*	27.2 (1.3, 60.9)	23.6 (1.1, 60.8)	< 0.001*
Larynx	Mean (Gy)	33.8 (0.2, 65.8)	26.2 (0.2, 67.1)	0.173	37.4 (0.7, 71.3)	30.9 (0.6, 70.6)	0.002*	35.3 (0.2, 71.3)	29.3 (0.2, 70.6)	0.001*
Cord	Max (Gy)	35.8 (7.3, 41.6)	29.4 (5.6, 40.0)	0.001*	35.3 (25.3, 41.5)	30.3 (15.9, 39.6)	0.001*	35.6 (7.3, 41.6)	29.9 (5.6, 40.0)	< 0.001*
Brainstem	Max (Gy)	25.7 (4.3, 57.3)	11.7 (2.8, 56.9)	0.001*	25.4 (3.4, 46.9)	22.2 (4.5, 41.0)	0.001*	25.6 (3.4, 57.3)	21.2 (2.8, 56.9)	< 0.001*
Lt. Cochlea	Max (Gy)	11.9 (2.3, 64.6)	5.9 (1.6, 65.5)	0.011*	8.5 (0.7, 59.9)	5.9 (0.6, 56.3)	0.001*	10.2 (0.7, 64.6)	5.9 (0.6, 65.5)	< 0.001*
Rt. Cochlea	Max (Gy)	16.1 (1.2, 50.0)	8.2 (1.0, 50.0)	0.001*	9.5 (0.9, 25.2)	5.7 (0.9, 17.7)	0.001*	12.2 (0.9, 50.0)	6.8 (0.9, 50.0)	< 0.001*

Abbreviations: Norm. Tiss., normal tissue (defined as external contour minus the PTV & OAR volumes); Rt, right; Lt, left; D95, dose to 95% of the volume. [†]P-values were calculated using the Wilcoxon signed-rank test.
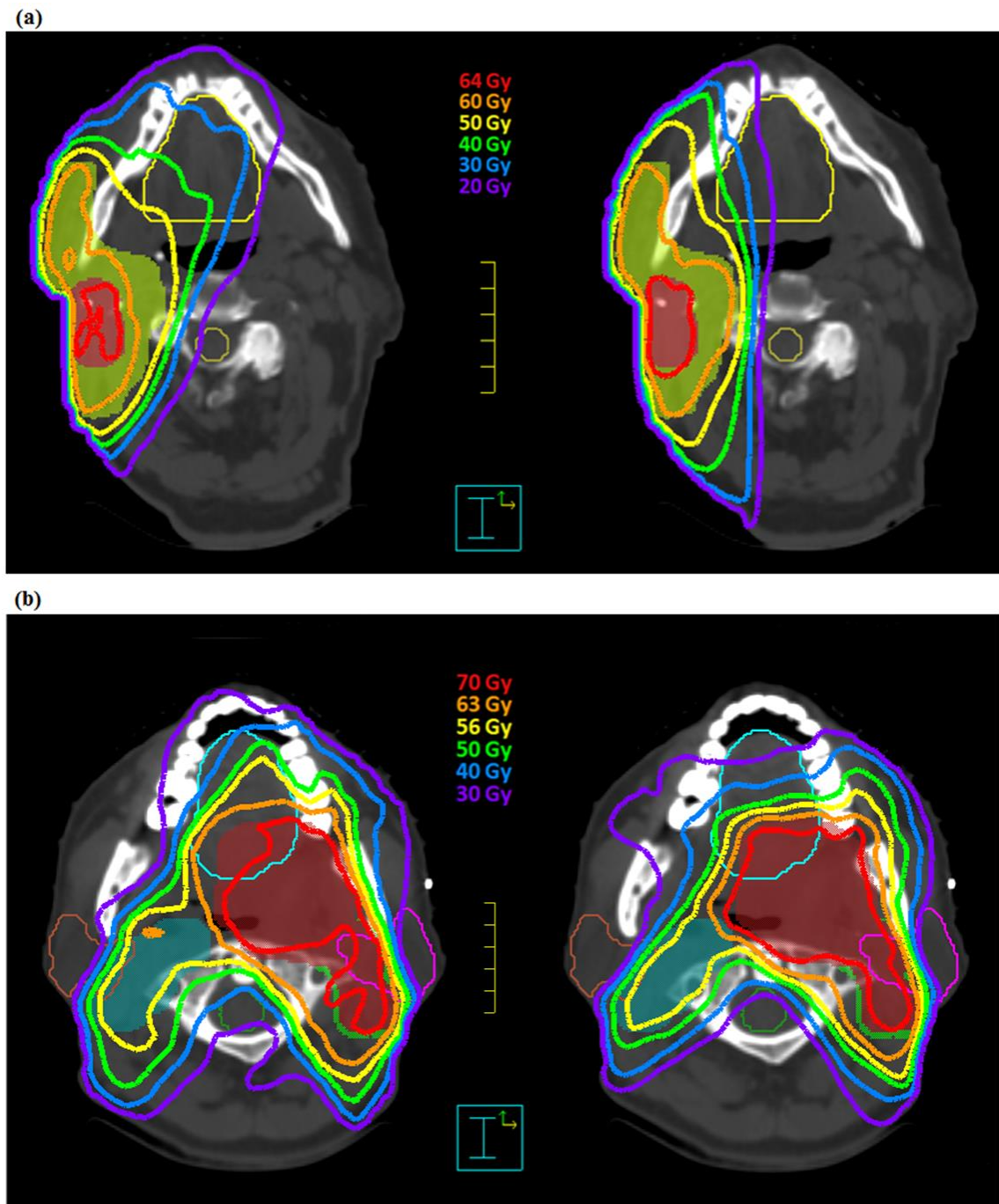
Figure 2.3: Comparison of dose distributions between: (a) the clinical VMAT plan (left) and UIMAT plan (right) for patient 1 with PTV_{64Gy} in red and PTV_{60Gy} in light green color wash; (b) the IMRT plan (left) and the UIMAT plan (right) for patient 29 with PTV_{70Gy} in red, PTV_{63Gy} in green, and PTV_{56Gy} in cyan color wash.

2.4 Discussion

The UIMAT technique exhibited many promising features, most notable being its ability to reduce the dose to organs at risk (see Table 2.1). This is also evident from the average DVH comparisons and sample dose distribution comparisons in Figure 2.2 and Figure 2.3, respectively, where improved sparing of the various organs at risk can be observed. In addition to this, Table 2.1 and Figure 2.2 shows that UIMAT was able to reduce the dose to organs at risk without increasing the dose to the rest of the normal tissue (defined here as all tissue outside of the reported PTVs and OARs), suggesting that the reduction in OAR dose did not result from the redistribution of dose to unspecified normal tissue, but rather from improved utilization of dose delivery. This reduction in OAR dose has the potential to lower both the severity and frequency of toxicities attributed to head-and-neck radiotherapy such as xerostomia, stomatitis, and sensorineural hearing loss. Alternatively, these improvements in dose delivery could allow for further dose escalation while maintaining a similar toxicity profile observed today.

Some small variability was seen in the conformity indices for the target volumes, with UIMAT conformity generally lying between that of IMRT and VMAT. This is not entirely surprising given that UIMAT is a mixture of these two techniques. This could also be a result of optimization technique, for example by imposing a higher priority on OAR sparing compared to conformity. This result was not universally observed though, as can be seen from the individual patient results in Supplementary Table 2.2 and Supplemental Table 2.3. In addition to its dosimetric advantages, UIMAT plans required fewer MUs and had comparable delivery times to VMAT.

Several areas of improvement for the UIMAT algorithm have been identified during this retrospective planning study. For instance, the current algorithm does not enforce a minimum MU or MLC segment area during plan optimization. As a result, UIMAT plans may be susceptible to dosimetric errors introduced by small-field dosimetry and small MU delivery [19-21]. This is likely the source of the lower IMRT QA gamma pass rates observed relative to the clinical plans. To improve UIMAT delivery accuracy, future

versions of the UIMAT algorithm may implement a filtration step, in which small fields are removed, or a direct aperture optimization algorithm that enforces a minimum segment area.

As with any retrospective planning study, this work was susceptible to certain biases such as providing more resources to a new treatment technique compared with the standard one. To combat this, treatment planning times were limited to a maximum of 6 hours (for the most complex cases) in order to match clinical time constraints. While it may appear that reusing the clinical objectives for UIMAT optimization gave our planner a head start, this was not the case. Most of the plan setup is automated within our institution, whereas our UIMAT method is still a manual process, and so any amount of time gained by copying (rather than populating) the objective list was easily lost in the UIMAT plan setup. The selection of endpoints may also be viewed as a source of bias. The metrics that have been reported here are, what we believe to be, the most clinically relevant based on literature as well as local standards. Additional efforts to avoid bias were made by preventing the planner from "over-optimizing" certain objectives. For example, an objective's dose or weight was only modified when the objective's relative contribution to the total objective function approached zero. Furthermore, we attempted to minimize the global dose to all OARs (including those which were not reported here) as a medical dosimetrist would, without favoring the specific endpoints presented in this work. This can be observed from the comparison of average dose-volume histograms in Figure 2.2.

The clinical and UIMAT plans presented here were also not selected based on multi-criteria optimization (MCO) or Pareto fronts. Therefore, the presented plans may not represent the Pareto-optimal solutions and one could question whether the observed dosimetric advantages result from suboptimal clinical beam configurations rather than from the superiority of our UIMAT technique. Although Pareto fronts have been previously implemented within Pinnacle [22], such an investigation is beyond the scope and capabilities of the current study. Notwithstanding, the clinical and UIMAT plans likely represent near-Pareto optimal solutions, since OAR dose objectives were pushed until further dose reduction in OARs would compromise target volume coverage.

This technique has a similar treatment planning and delivery processes as VMAT, which would allow cancer clinics to easily transition from VMAT to UIMAT. For example, a planner need only select the starting and stopping angles for the UIMAT plan, similar to VMAT planning, as the beam angles for static delivery are chosen automatically by the algorithm. Similarly, a radiation therapist would not need to perform any additional steps for UIMAT setup and delivery than what is currently required for stand-alone VMAT. Of course, UIMAT would require standard commissioning and testing prior to clinical implementation.

2.5   Conclusion

Compared to stand-alone VMAT or IMRT for head-and-neck cancer, UIMAT plans exhibited comparable target volume coverage and dose conformity while significantly reducing the dose to the surrounding organs at risk. Furthermore, UIMAT plans required only a single arc and fewer MUs on average than either VMAT or IMRT plans. We expect that this technique will also yield dosimetric benefits for other complex treatment sites.

2.6   Acknowledgement

2.7   References

1.   Veldeman L, Madani I, Hulstaert F, De Meerleer G, Mareel M, De Neve W. Evidence behind use of intensity-modulated radiotherapy: a systematic review of comparative clinical studies. *Lancet Oncol.* 2008; 9:367-75.
2.   Staffurth J, et al. A Review of the Clinical Evidence for Intensity-modulated Radiotherapy. *Clin. Oncol.* 2010; 22:643-57.
3.   Otto K. Volumetric modulated arc therapy: IMRT in a single gantry arc. *Med. Phys.* 2008; 35:310-7.
4.   Jiang X, Li T, Liu Y, et al. Planning analysis for locally advanced lung cancer: Dosimetric and efficiency comparisons between intensity-modulated radio-therapy

(IMRT), single-arc / partial-arc volumetric modulated arc therapy (SA / PA-VMAT). <u>Radiat. Oncol.</u> 2011;6:140.

5. Palma D, Vollans E, James K, et al. Volumetric Modulated Arc Therapy for Delivery of Prostate Radiotherapy: Comparison with Intensity-Modulated Radiotherapy and Three-Dimensional Conformal Radiotherapy. Int. J. Radiat. Oncol. Biol. Phys. 2008;72:996-1001.

6. Rao M, Yang W, Chen F, et al. Comparison of Elekta VMAT with helical tomotherapy and fixed field IMRT: Plan quality, delivery efficiency and accuracy. Med. Phys. 2010;37:1350-9.

7. Lu SH, Cheng JC, Kuo SH, et al. Volumetric modulated arc therapy for nasopharyngeal carcinoma: A dosimetric comparison with TomoTherapy and step-and-shoot IMRT. Radiother. Oncol. 2012;104:324-30.

8. Kim H, Li R, Lee R, et al. Dose optimization with first-order total-variation minimization for dense angularly sampled and sparse intensity modulated radiation therapy (DASSIM-RT). Med. Phys. 2012;39:4316-27.

9. Wang C, Luan S, Tang G, Chen DZ, Earl MA, Yu CX. Arc-modulated radiation therapy (AMRT): A single-arc form of intensity-modulated arc therapy. Phys. Med. Biol. 2008;53:6291-303.

10. Matuszak MM, Steers JM, Long T, et al. FusionArc optimization: A hybrid volumetric modulated arc therapy (VMAT) and intensity modulated radiation therapy (IMRT) planning strategy. Med. Phys. 2013;40:071713.

11. Robar JL, Thomas C. HybridArc: A novel radiation therapy technique combining optimized dynamic arcs and intensity modulation. Med. Dosim. 2012;37:358-68.

12. Zarepisheh M, Li R, Ye Y, Xing L. Simultaneous beam sampling and aperture shape optimization for SPORT. Med. Phys. 2015;42:1012-22.

13. Zhao N, Yang R, Jiang Y, Tian S, Guo F, Wang J. A Hybrid IMRT/VMAT Technique for the Treatment of Nasopharyngeal Cancer. BioMed. Res. Int. 2015;2015:940102.

14. Teoh M, Clark CH, Wood K, Whitaker S, Nisbet A . Volumetric modulated arc therapy: a review of current literature and clinical use in practice. Br. J. Radio. 2011;84:967-96.

15. Hoover D, MacFarlane M, Wong E, Battista J, Chen J. Feasibility of a unified approach to intensity-modulated radiation therapy and volume-modulated arc therapy optimization and delivery. Med. Phys. 2015;42:726-34.

16. Marks LB, Yorke ED, Jackson A, et al. Use of Normal Tissue Complication Probability Models in the Clinic. Int. J. Radiat. Oncol. Biol. Phys. 2010;76:S10-9.

17. Oozeer R, Chauvet B, Garcia R, Berger C, Felix-Faure C, Reboul F. Dosimetric evaluation of conformal radiotherapy: conformity factor. Cancer Radiother. 2000;4:207-16.

18. Low D, Harms H, Mutic S, Purdy J. A technique for the quantitative evaluation of dose distributions. Med Phys. 1998;25:656-61

19. Lydon JM. Theoretical and experimental validation of treatment planning for narrow MLC defined photon fields. Phys Med Biol 2005;50:2701-14.

20. Sharpe MB, Miller BM, Yan D, Wong JW. Monitor unit settings for intensity modulated beams delivered using a step-and-shoot approach. Med Phys. 2000;27:2719-25

21. Ezzell GA, Chungbin S. The overshoot phenomenon in step-and-shoot IMRT delivery. J Appl Clin Med Phys 2001;2:138-48.

22. Janssen T, van Kesteren Z, Franssen G, Damen E, van Vliet C. Pareto Fronts in Clinical Practice for Pinnacle. Int. J. Rad. Onc. Biol. Phys. 2011;85:873-80.

Chapter 3 – A fast inverse direct aperture optimization algorithm for intensity-modulated radiation therapy

This chapter was adapted from the published article entitled "A fast inverse direct aperture optimization algorithm for intensity-modulated radiation therapy" by Michael MacFarlane, Douglas Hoover, Eugene Wong, Pedro Goldman, Jerry J. Battista, and Jeff Z. Chen, *Medical Physics* 2019; **46**(3): 1127-39. Permission to reproduce this article was granted by John Wiley and Sons and is provided in Appendix B.3. Supplemental tables and figures for this chapter are provided in Appendix D.

3.1   Introduction

Direct aperture optimization (DAO) is a frequently used tool in external beam radiotherapy treatment planning [1-9]. A DAO algorithm optimizes the beam aperture shapes [i.e. multi-leaf collimator (MLC) positions] and intensities based on the treatment planning objectives while adhering to any dosimetric or machine-specific delivery constraints.

Due to the size and complexity of the DAO problem, it may take several hours to attain an optimal treatment plan using a DAO algorithm, particularly when dealing with a large high-resolution dataset or when multiple optimization trials are needed to adequately satisfy the clinical treatment objectives. Treatment plans may therefore be left at a sub-optimal solution when there is insufficient time for treatment planning. Furthermore, applications such as online treatment planning and adaptation for changing patient anatomy may be impractical as an updated treatment plan is needed within minutes while the patient remains immobilized on the treatment unit.

A major source of computational inefficiency in DAO comes from the repeated evaluation of the objective function and its gradient vector [7,9-12]. To calculate these components, the DAO algorithm must first compute the 3D dose distribution based on the plan parameters of the current iteration. This computation involves several gigabytes worth of dose data, which often results in a computational bottleneck in the optimization process. This bottleneck can be mitigated by performing the calculation in parallel over

multiple central or graphical processing units (CPU/GPUs) [7,9-12]. However, the computational speed gained by parallelizing these calculations is still insufficient for emerging applications such as online or real-time plan optimization.

In this work, we propose reformulating the objective function used in DAO so that the computational workload associated with evaluating the objective function and computing its gradient vector is greatly reduced. Specifically, we adapted the objective function used in a previously developed fluence map optimization algorithm called Fast Inverse Dose Optimization (FIDO) to optimize the aperture shapes and intensities of IMRT beams [13,14]. The number of operations performed when evaluating the adapted FIDO objective function and its gradient vector is substantially lower than that of the conventional objective function, resulting in substantially faster plan optimization.

For clarity, a brief summary of the FIDO algorithm is provided in the following section. We then describe the proposed fast inverse direct aperture optimization (FIDAO) algorithm. Finally, we present the results of a treatment planning study comparing a prototype FIDAO algorithm with a conventional DAO algorithm. For simplicity, both DAO algorithms use a singular value decomposition (SVD) dose computation algorithm but note that a more sophisticated and accurate dose calculation algorithm can also be used.

3.2   Materials and Methods

3.2.1   Introduction to FIDO

In fluence map optimization (FMO), each beam is decomposed into an array of smaller, finite-sized pencil-beams. Each pencil-beam is assigned a unique index, i, and intensity, τ_i. A large but sparse pencil-beam-based dose matrix, $\boldsymbol{d}$, is then computed using any dose calculation algorithm and it is stored in memory. The dose matrix element $\boldsymbol{d}_{xi}$ specifies the dose deposited to voxel x per unit intensity of pencil-beam i. During optimization, the FMO algorithm can compute the 3D dose distribution by multiplying this pre-calculated pencil-beam dose matrix with a vector containing the pencil-beam intensities.

FMO algorithms optimize the beam fluence maps by finding the minimum solution of an objective function (f) such as the following,

$$f(\vec{\tau}) = p_{ptv} \sum_{x \in PTV} \left(\sum_{i} \boldsymbol{d}_{xi}\tau_i - d_{ptv} \right)^2 + p_{oar} \sum_{x \in OAR} \left(\sum_{i} \boldsymbol{d}_{xi}\tau_i \right)^2, \qquad (1)$$

where p_{ROI} is the penalty weight assigned to each region of interest's (ROI) objective (PTV or OAR), and d_{ptv} is the dose prescribed to the planning target volume (PTV). This objective function approaches a global minimum when the dose to each voxel in the PTV approaches the prescribed dose, while the dose to all surrounding organs at risk (OAR) is as close to zero as possible. Notice, however, that a minimum could be obtained by combining positive and negative pencil-beam intensities. Since negative pencil-beam intensities represent a non-physical process (the removal of radiation from the patient), most FMO algorithms include a non-negative pencil-beam intensity constraint, resulting in the following FMO problem,

$$\underset{\tau}{\text{minimize}} \quad p_{ptv} \sum_{x \in PTV} \left(\sum_{i} \boldsymbol{d}_{xi}\tau_i - d_{ptv} \right)^2 + p_{oar} \sum_{x \in OAR} \left(\sum_{i} \boldsymbol{d}_{xi}\tau_i \right)^2, \qquad (2)$$

$$\text{subject to} \quad \tau_i \geq 0.$$

The solution to this FMO problem can be found through a variety of iterative constrained optimization techniques [3,11,12,15]. However, solving this FMO problem with an iterative method can be very inefficient. This is due to the frequency with which these constrained optimization algorithms must compute the objective function value (and its gradient vector if the algorithm is gradient-based) as it must first compute the product of the very large pencil-beam dose matrix, $\boldsymbol{d}$, and the vector containing the pencil-beam intensities, $\vec{\tau}$, of the current iteration.

In FIDO, the objective function was reformulated as the following: [13,14]

$$f(\vec{\tau}) = p_{ptv} \sum_{x \in PTV} \left(\sum_{i} \boldsymbol{d}_{xi}\tau_i - d_{ptv} \right)^2 + p_{oar} \sum_{x \in OAR} \sum_{i} \boldsymbol{d}_{xi}^2 \tau_i^2. \qquad (3)$$

In this formulation, the OAR objective function (which is the primary culprit leading to negative pencil-beam weights) can no longer approach its minimum through the use of

negative pencil-beam intensities. Instead, the OAR objective can only reach its minimum when all pencil-beams depositing dose to the OAR have null intensity. Additional regulative objectives can be added to the objective function to further suppress the use of negative pencil-beam intensities by the PTV objective; however, previous experience has found that these additional regulation terms are unnecessary [14].

Given that the FIDO objective function (Equation 3) is purely quadratic and that constraints are not likely needed, its minimum can be found by differentiating with respect to each pencil-beam's weight and setting each equation to zero (which is equivalent to Newton's Method in Optimization) [15]. The resulting system of equations can be written as,

$$\boldsymbol{\alpha}\vec{\tau} = \vec{\beta}, \tag{4}$$

where

$$\boldsymbol{\alpha}_{ji} = p_{ptv} \sum_{x \in PTV} \boldsymbol{d}_{jx}^T \, \boldsymbol{d}_{xi} + p_{oar} \, \delta_{ij} \sum_{x \in OAR} \boldsymbol{d}_{jx}^T \, \boldsymbol{d}_{xi}$$

$$\beta_j = p_{ptv} \, d_{ptv} \sum_{x \in PTV} \boldsymbol{d}_{jx}^T \, .$$

This matrix equation can be efficiently solved via matrix inversion to give the globally-optimal and physically-feasible fluence maps.

Multiple optimizations are often necessary to fine-tune the PTV coverage and/or OAR sparing. To minimize the amount of work performed in subsequent optimizations, FIDO stores each ROI's contribution to $\vec{\beta}$ and $\boldsymbol{\alpha}$. When the OAR and/or PTV weights are adjusted in subsequent optimizations, the FIDO matrix equation can be quickly computed by rescaling and summing these stored matrices.

3.2.2   FIDAO Formulation

The relationship between voxel dose and MLC position is non-linear, and by extension the objective function too will vary non-linearly with MLC-position. The MLC positions are also subject to numerous mechanical delivery constraints. Therefore, it is not possible to optimize the MLC positions by solving a single matrix equation as we had

with the pencil-beam intensities in FIDO [15]. Instead, we are forced to use an iterative constrained optimization technique as in the conventional FMO methods. Fortunately, as will be discussed shortly, we can improve the efficiency of computing the objective function value and its gradient vector by using a FIDO-like objective function. To do this, we first need a method of converting the beam aperture information into equivalent fluence maps.

Numerous DAO algorithms convert the plan's MLC positions, $\vec{l}$, and aperture intensity, $\vec{w}$, into equivalent fluence maps, $\vec{\tau}(\vec{l}, \vec{w})$, so that the pre-calculated pencil-beam dose matrix, $\boldsymbol{d}$, can continue to be used during optimization, to compute the objective function value and its gradient vector [3,9]. One method of converting the aperture parameters into equivalent fluence maps is through the following approximate relationship:

$$\tau_j(\vec{l}, \vec{w}) \approx \sum_{v} \boldsymbol{T}_{jv}(\vec{l})\, w_v, \qquad (5)$$

where w_v is the intensity of aperture v, and $\boldsymbol{T}_{jv}(\vec{l})$ is a non-convex piecewise linear function describing the fractional transmission through pencil-beam j by aperture v [9,16]. An illustration of this transmission matrix is shown in Figure 3.1. If pencil-beam j is completely blocked by aperture v, or if the pencil-beam belongs to another beam and therefore cannot be exposed by this beam's aperture, then the fractional transmission $\boldsymbol{T}_{jv}$ will be 0 (e.g. pencil-beams 1-3 in Figure 3.1). Conversely, if pencil-beam j belongs to the same beam as the aperture and is completely exposed by the aperture, then the transmission matrix element will have value 1 (e.g. pencil-beam 8 in Figure 3.1). Finally, if pencil-beam j is partially exposed by the aperture, the fractional exposed area of the pencil-beam is assigned to the transmission matrix (e.g. pencil-beams 7 and 11 in Figure 3.1). By multiplying this transmission matrix with a vector containing the aperture intensities, we can approximate the fluence map produced when delivering all the beam's apertures. This conversion of the aperture information into equivalent fluence will be sufficiently accurate so long as the size of the pencil beams are not too large. Otherwise,

the fractional transmission may not adequately model the true fluence produce by delivering the plan apertures.

Col. Row	(1)	(2)	(3)	(4)
(1)	1	5	9	13
(2)	2	6	10	14
(3)	3	7	11	15
(4)	4	8	12	16

Col. Row	(1)	(2)	(3)	(4)
(1)	$T_{1,1}=0$	$T_{5,1}=0$	$T_{9,1}=0$	$T_{13,1}=0$
(2)	$T_{2,1}=0$	$T_{6,1}=1$	$T_{10,1}=1$	$T_{14,1}=0$
(3)	$T_{3,1}=0$	$T_{7,1}=0.75$	$T_{11,1}=0.5$	$T_{15,1}=0$
(4)	$T_{4,1}=1$	$T_{8,1}=1$	$T_{12,1}=1$	$T_{16,1}=1$

Figure 3.1: Illustration of the transmission matrix. The left grid shows the index that each pencil-beam was assigned (1-16) during FMO. The right grid shows the pencil-beam array superimposed with MLC of the first aperture (shown in blue). The corresponding values assigned to the first column of the transmission matrix, due to the first apertures shape, is provided in the right array.

Using the equivalent fluence maps from Equation 5, the standard FMO problem from Equation 2 can be converted into the following generalized DAO problem:

$$\underset{\vec{l},\vec{w}}{\text{minimize}} \quad p_{ptv}\sum_{x\in PTV}\left(\sum_i d_{xi}\tau_i(\vec{l},\vec{w})-d_{ptv}\right)^2 + p_{oar}\sum_{x\in OAR}\left(\sum_i d_{xi}\tau_i(\vec{l},\vec{w})\right)^2, \text{(6)}$$

$$\text{subject to} \quad \tau_i(\vec{l},\vec{w}) = \sum_v \boldsymbol{T}_{iv}(\vec{l})\, w_v,$$

$$w_v \geq 0,$$

$$\boldsymbol{c}(\vec{l}) \geq \vec{b},$$

where the aperture intensities, like the pencil-beam intensities, must be positive and the constraint, $\boldsymbol{c}(\vec{l}) \geq \vec{b}$, describes all boundary, linear, and nonlinear machine-based delivery constraints on the MLC (e.g. the minimum leaf gap, position limits, leaf

interdigitation, or minimum open-area). Similarly, the equivalent fluence maps from Equation 5 can be used with the FIDO objective function in Equation 3 to construct the following aperture-based FIDO problem:

$$\underset{\vec{l},\vec{w}}{\text{minimize}} \quad p_{ptv} \sum_{x \in PTV} \left(\sum_i \boldsymbol{d}_{xi} \tau_i(\vec{l},\vec{w}) - d_{ptv} \right)^2 + p_{oar} \sum_{x \in OAR} \sum_i \boldsymbol{d}_{xi}^2 \tau_i^2(\vec{l},\vec{w}), \quad (7)$$

$$\text{subject to} \quad \tau_i(\vec{l},\vec{w}) = \sum_v \boldsymbol{T}_{iv}(\vec{l})\, w_v ,$$

$$w_v \geq 0,$$

$$\boldsymbol{C}(\vec{l}) \geq \vec{b}.$$

Like the FMO problem (Equation 2), these DAO problems can be solved using an iterative (often gradient-based) constrained optimization technique [1-10]. However, these DAO algorithms will be inefficient from repeatedly computing the product of the large pencil-beam dose matrix and the effective fluence maps produced by the plan parameters of the current iteration.

Another way of evaluating the objective function is through its Taylor series expansion. Specifically, since the objective function is purely quadratic with respect to the pencil-beam intensity, its value can be computed *without approximation* using a second-order Taylor series expansion, such as the following expansion centered at $\vec{\tau} = 0$:

$$f(\vec{\tau}) = f(0) + \nabla f(0) \cdot \vec{\tau} + \frac{1}{2}\, \vec{\tau}^T\, \mathbf{H}[f]\, \vec{\tau},$$

where $\nabla f(0)$ denotes the gradient vector of the objective function evaluated at $\vec{\tau} = 0$ and $\mathbf{H}[f]$ denotes the Hessian matrix of the objective function. It is advantageous to use this Taylor series expansion as the Hessian matrix will often be several orders of magnitude smaller than the pencil-beam dose matrix. Therefore, fewer operations will be performed when evaluating the objective functions with its Taylor series expansion as opposed to its non-expanded form. Furthermore, since the Hessian matrix is also symmetric, we can reduce the amount of computer memory taken up during optimization, and possibly avoid

any von Neumann bottlenecks (where the computation is limited by the data transfer rates) during optimization [12].

While the Taylor series expansion may reduce the number of operations performed when evaluating the objective function, it does require us to compute the objective function's Hessian matrix prior to optimization which could be computationally intensive in itself. This is where using the FIDO objective function becomes advantageous. First, note that the Hessian matrix of the FIDO objective function is proportional to the $\boldsymbol{\alpha}$ matrix in Equation 4, [15] while the Hessian matrix of the standard objective function is,

$$\mathbf{H}[f] = p_{ptv} \sum_{x \in PTV} \boldsymbol{d}_{jx}^T \boldsymbol{d}_{xi} + p_{oar} \sum_{x \in OAR} \boldsymbol{d}_{jx}^T \boldsymbol{d}_{xi}.$$

Notice that, while similar, the equations for $\boldsymbol{\alpha}$ and the standard objective function's Hessian matrix differ by a Krönecker-delta function in the OAR term. This means that the OAR objectives will contribute to every element in the Hessian matrix of the standard objective function, whereas the OAR objectives will only contribute to the diagonal elements of the $\boldsymbol{\alpha}$ matrix in FIDO. As a result, we can compute the Hessian matrix of the FIDO objective function far more efficiently than that of the standard objective function, especially when large OARs such as the normal unspecified tissue have planning objectives. Additional modifications can be made to the FIDO objective function so that dose-volume objectives can be included in the optimization. These modifications take into consideration the total number of operations performed when updating $\boldsymbol{\alpha}$ and $\vec{\beta}$ matrices during optimization and will be discussed in further detail in the following section.

The Taylor series expansion of the FIDO objective function can be written as,

$$f(\vec{\tau}) = f(0) + \vec{\tau} \cdot \left(\boldsymbol{\alpha}\, \vec{\tau} - 2\vec{\beta} \right), \tag{8}$$

where $f(0)$ is a constant. Since this constant term will have no effect on the optimal solution, it can be omitted from computations during the optimization. Therefore, like

Equation 7, a fast inverse direct aperture optimization (FIDAO) problem can be formulated as the following generalized problem:

$$\underset{\vec{l}, \vec{w}}{\text{minimize}} \quad \vec{\tau}(\vec{l}, \vec{w}) \cdot \left(\boldsymbol{\alpha} \, \vec{\tau}(\vec{l}, \vec{w}) - 2\vec{\beta} \right), \tag{9}$$

$$\text{subject to} \quad \tau_i(\vec{l}, \vec{w}) = \sum_v \boldsymbol{T}_{iv}(\vec{l}) \, w_v,$$

$$w_v \geq 0,$$

$$\boldsymbol{C}(\vec{l}) \geq \vec{b}.$$

If we are using a gradient-based optimization technique, the derivatives of the objective function with respect to each aperture μ's intensity, w_μ, and with respect to the leaf position of each leaf k in each aperture μ, $l_k^{(\mu)}$, can be computed using the following:

$$\frac{\partial f}{\partial w_\mu} = 2 \sum_j \boldsymbol{T}_{\mu j}^T(\vec{l}) \left(\boldsymbol{\alpha} \, \vec{\tau}(\vec{l}, \vec{w}) - \vec{\beta} \right)_j, \tag{10a}$$

$$\frac{\partial f}{\partial l_k^{(\mu)}} = 2 \sum_j w_\mu \frac{\partial \boldsymbol{T}_{\mu j}^T(\vec{l})}{\partial l_k^{(\mu)}} \left(\boldsymbol{\alpha} \, \vec{\tau}(\vec{l}, \vec{w}) - \vec{\beta} \right)_j. \tag{10b}$$

For convenience, the pencil-beam array is aligned with the MLC leaf banks as shown in Figure 3.1. Therefore, any leaf motion will either expose or block the pencil-beam(s) that currently coincide with the MLC leaf position (for instance, pencil-beam 7 or 11 in Figure 3.1) and we can use the following piecewise approximation when evaluating Equation 10b for each leaf in each aperture, [9,16]

$$\frac{\partial \boldsymbol{T}_{\mu j}^T(\vec{l})}{\partial l_k^{(\mu)}} = \begin{cases} \pm \dfrac{1}{h_{pb}}, & \text{leaf } k \text{ of apeture } \mu \, (l_k^{(\mu)}) \text{ coincides with pencil beam } j \\ 0, & \text{otherwise} \end{cases} \tag{11}$$

with h_{pb} being the width of the pencil-beams. The sign ($\pm$) of this piecewise function will depend on whether the differentiated leaf k is a member of the left or right leaf bank, and whether a change in its position in the positive direction of motion will lead to the coinciding pencil-beam becoming more exposed or blocked. If a leaf resides exactly between two pencil beams (e.g. the leaf between pencil beam 2 and 6 in Figure 3.1), the leaf will be considered to coincide with the pencil beam on the right unless the leaf is on

the right boundary of the calculated pencil beam array (e.g. the leaf on the edge of pencil beam 16 in Figure 3.1) in which case it will be considered to coincide with the pencil beam on the left [16].

3.2.3   Dose-volume objectives

Often a treatment plan must satisfy a variety of clinical dose-volume objectives such as a minimum PTV dose or a maximum dose to some volume of an OAR. Dose-volume objectives are typically included as a separate term in the objective function, such as the following for a minimum PTV dose objective:

$$f_{min-dvh}^{(ptv)}(\vec{\tau}) = p_{ptv} \sum_{x \in PTV} \Theta \left(d_{min} - \sum_i d_{xi}\tau_i \right) \left(d_{min} - \sum_i d_{xi}\tau_i \right)^2,$$

where Θ is the Heaviside function and d_{min} is the minimum threshold dose [16]. Note that a similar equation is used for maximum dose objectives in the PTV and OARs.

Like the standard objective function (Equation 1), these dose-volume objective functions will contribute to every element in the Hessian matrix and gradient vector. Moreover, their contribution to the Hessian matrix and gradient vector will have to be updated throughout the optimization, as the dose distribution changes and non-compliant voxels begin to comply with the dose-volume objectives and vice versa. This repeated computation of the Hessian matrix and gradient vector could be very time-consuming and so we propose the following approach.

Similar to the original FIDO publication, we use a voxel-based OAR penalty weight, $p_{oar}(x)$, and prescribed dose, $d_{ptv}(x)$, in the FIDO objective function (Equation 3) to include dose-volume objectives [14]. The amount that these terms are varied by is based on: (1) whether the voxel is contributing to the violation of a dose-volume objective, (2) the amount of dose or volume that the voxel or ROI is violating a dose-volume objective by, and (3) the penalty weight assigned to the dose-volume objective. Details on how the prescribed dose and OAR penalty weight are spatially varied can be found in Section

3.6Appendix, along with examples demonstrating its effectiveness. By doing this, the equations for $\boldsymbol{\alpha}$ and $\vec{\beta}$ become,

$$\boldsymbol{\alpha}_{ji} = p_{ptv} \sum_{x \in PTV} \boldsymbol{d}_{jx}^T \boldsymbol{d}_{xi} + \delta_{ij} \sum_{x \in OAR} p_{oar}(x) \boldsymbol{d}_{jx}^T \boldsymbol{d}_{xi}$$

$$\beta_j = p_{ptv} \sum_{x \in PTV} d_{ptv}(x) \boldsymbol{d}_{jx}^T.$$

By spatially varying these specific terms, we can include dose-volume objectives in the optimization while also minimizing the number of elements in $\boldsymbol{\alpha}$ and $\vec{\beta}$ that need to be updated during optimization. Specifically, we only need to update the diagonal elements of the $\boldsymbol{\alpha}$ matrix when OAR dose-volume objectives are included, and the elements of $\vec{\beta}$ only when PTV dose-volume objectives are included. A similar approach was used in the original FIDO algorithm to enforce minimum and maximum point dose objectives [14]. Specifically, after solving the FIDO matrix equation (Equation 4), the FIDO algorithm would re-compute and solve the matrix equation a second time with a spatially varying prescribed dose and penalty weights based on the previous solution to the FIDO matrix equation [14]. With sufficient weighting of the dose-volume objectives, the second solution to the FIDO matrix equation will improve the maximum or minimum point dose objectives.

3.2.4   Implementation & testing of the prototype algorithm

A proof-of-concept FIDAO algorithm was developed in MATLAB v9.4 (Mathworks Inc, Natick, MA) using an open-source treatment planning toolkit called matRad v2.2. [16]. This toolkit includes a graphical user interface for creating and evaluating the treatment plan, a singular value decomposition (SVD) dose computation algorithm for calculating the pencil-beam dose matrix, MLC leaf-sequencing algorithms for generating apertures from fluence maps, and sample datasets. It also includes a built-in experimental DAO algorithm, which we used as an independent benchmark for our FIDAO algorithm [16].

The prototype FIDAO algorithm used the open-source interior-point optimization (IPOPT) package to solve the FIDAO problem in Equation 9 [15]. This IPOPT package

was made available through the computational infrastructure for operations research (COIN-OR) initiative [17]. This algorithm was selected so that a fair comparison could be made between our FIDAO algorithm and matRad's DAO algorithm, as it too uses the same IPOPT package to solve the standard DAO problem in Equation 6. Our goal for this planning study was to compare the time it took each algorithm to converge to similar plans, using the same optimization algorithm but different equations for the objective function and its gradient vector. Therefore, the same planning objectives, starting apertures, convergence criteria, delivery constraints, and optimization settings were used by both algorithms.

IMRT treatment plans were created on the Common Optimization for Radiation Therapy (CORT) datasets that were included with the matRad toolkit [16,18]. This library includes the AAPM TG-119 box phantom (shown in Figure 3.2 below) as well as sample prostate, liver, and head-and-neck clinical cases. The voxel size for dose calculations and plan evaluation were: 3x3x2.5 mm^3 in the TG-119 case, 3x3x3 mm^3 in the prostate case, 3x3x2.5 mm^3 in the liver case, and 3x3x5 mm^3 in the head-and-neck case. Pencil beams were set to 5x5 mm^2 in size. The couch and gantry angles were set to the suggested values in the CORT study for IMRT treatment [18].

For the planning study, the plans first underwent FMO optimization using matRad's built in FMO algorithm and the planning objectives listed in Table 3.1 [16]. The plan then underwent aperture sequencing using matRad's leaf-sequencing algorithm [19]. The matRad leaf-sequencing algorithm was modified slightly so that the total number of apertures in a plan could be restricted. Specifically, if the sequencer produced more apertures than a user-defined limit, the apertures with the smallest open area were discarded. The maximum number of apertures in the plan was set to 10 times the number of beams.

After aperture sequencing, one copy of the post sequencing plan underwent DAO with the standard DAO algorithm implemented in matRad, and another copy underwent DAO with the FIDAO algorithm. Both algorithms used the same planning objectives listed in Table 3.1. Identical objective penalty weights were also used in both plans,

except for the TG-119 phantom case, where marginally higher OAR penalty weights were necessary in the FIDAO plan to achieve similar OAR sparing as the standard DAO plan.

Table 3.1: Optimization objectives used by both algorithms.

No.	Site	Beams (Apertures)	Optimization Objectives
1.	TG-119	5 (50)	• Uniform 50 Gy dose to the C-shaped Target.
			• Minimal dose to the core OAR and body.
			• Maximum point dose of 50 Gy in the body, and 25 Gy in the core OAR.
2.	Liver	7 (70)	• Uniform 45 Gy dose to the PTV.
			• Minimal dose to the healthy liver, heart & normal tissue.
			• Maximum point dose of 40 Gy in the normal tissue.
3.	Prostate	5 (50)	• Uniform 68 Gy and 56 Gy dose to the PTV and Nodes.
			• Minimal dose to the rectum, bladder & normal tissue.
			• Maximum point dose of 50 Gy in the normal tissue, rectum, and bladder.
4.	HN	10 (100)	• Uniform dose to each PTV (70 Gy, 63 Gy, and 56 Gy).
			• Minimal dose to the cord, brainstem, parotid glands & normal tissue.

Prior to DAO, FIDAO computed and stored each ROI's contribution to $\boldsymbol{\alpha}$ and $\vec{\beta}$. Furthermore, FIDAO also performed aperture weight optimization prior to DAO by solving the matrix equation,

$$\vec{w} = (\boldsymbol{T}^T \boldsymbol{\alpha} \, \boldsymbol{T})^{-1} \left(\boldsymbol{T}^T \vec{\beta} \right).$$

This FIDO-like aperture weight optimization equation is acquired by setting Equation 10a to zero. Its solution gives the optimal aperture weights based on the aperture information approximated by $\boldsymbol{T}$. This aperture weight optimization was performed prior to DAO in an effort to reduce the number of iteration performed in FIDAO, as the equation and its solution can be computed efficiently and the solution will place the plan significantly closer to a minimum of the objective function.

During DAO, both algorithms enforced a non-negative aperture weight constraint and position limits on the MLC leaves. These constraints are linear and are enforced during each iteration of the optimization [17]. Both methods used the default IPOPT termination criteria that came with the matRad software (v2.2.0) [16,17]. The maximum number of iterations was set to 500 and the threshold for termination was set to $1\text{x}10^{-8}$.

If dose-volume objectives were included in the optimization, FIDAO would update α and $\vec{\beta}$ twice during the optimization; once at the beginning of the optimization and a second-time after half of the maximum number of iterations were completed. If the optimization exited before the half-way point, the update would be performed then, and the optimization would automatically be executed a second time.

These optimizations were performed on the same desktop computer running Windows 10 with an Intel i7-4790 (3.6 GHz) CPU and 16 GB of RAM. To the best of our knowledge, no CPU or GPU parallelization was utilized in matRad's DAO algorithm's code [16]. Similarly, no parallel processing was used in FIDAO's code. The FIDAO and matRad optimized plans were then compared based on their dose-volume histograms, 3D dose distributions, and optimization time.

3.3   Results

Details about the test cases and the algorithms' performance are listed in Table 3.2. Note that the size of the square Hessian matrix (α) is proportional to the number of pencil beams (column 3) in the plan, while the size of the pencil-beam dose matrix is the number of pencil beams x the number of voxels (column 4). Also, note that the listed computation times for FIDAO's α and $\vec{\beta}$ (column 7) refers only to their *initial* computation time prior to DAO. The time spent updating α and $\vec{\beta}$ when dose-volume objectives were present is included in the *total* FIDAO optimization time (column 8).

Table 3.2: Information related to the size of the optimization problem, and each algorithm's performance.

No.	Site	Pencil Beams	Voxels [x 10^6]	Non-zero d_{xi} [x 10^6]	Voxels in PTV [x10^3]	$\alpha, \vec{\beta}$ Initialization	Optimization Time (Iter.) FIDAO	Standard
1.	TG-119	1,857	3.60	91.8	7.5	2.1 s	0.3s (17)	56.7 s (50)
2.	Liver	1,971	7.91	159.0	7.0	4.5 s	2.0s (28)	134.1 s (57)
3.	Prostate	3,034	3.05	159.6	16.3	6.2 s	2.5s (26)	180.6 s (107)
4.	HN	13,749	1.72	235.5	30.6	60.6 s	6.7s (20)	469.4 s (245)

Abbreviations: Iter, Iterations.

Dose-volume histograms (DVH) and sample dose distributions for each site are shown in Figure 3.2 through Figure 3.5. To demonstrate the effectiveness of these DAO algorithms, Figures 3.2-3.5 also include sample dose distributions and DVHs of the plan before DAO (post FMO and aperture sequencing). In the prostate, liver and head-and-neck cases, there were too many critical structures to display all the DVHs in one plot. Therefore, additional DVHs are available for these cases in Supplemental Figure 3.1 through Supplemental Figure 3.3. PTV and OAR dose metrics are also supplied in Supplemental Table 3.1 and Supplemental Table 3.2, respectively. As demonstrated by the comparisons of the dose-volume histograms and the sample dose distributions, FIDAO and standard DAO algorithm converged to nearly identical plans. However, FIDAO obtained the optimal solution substantially faster than the standard DAO algorithm in matRad (approximately 70-200 times faster; or up to 23 times faster when including the pre-calculation times for the α and $\vec{\beta}$ matrices), and in fewer iterations.
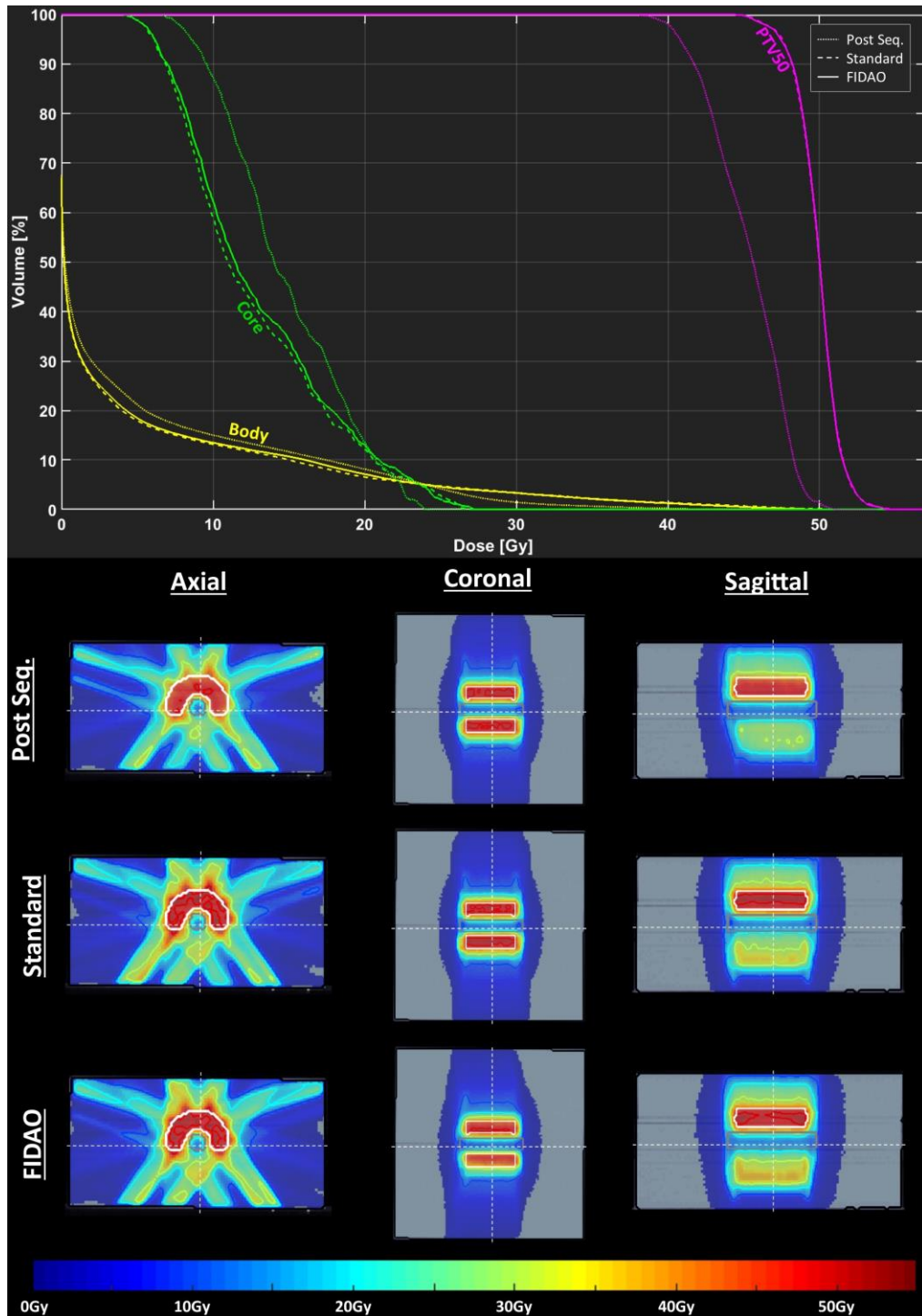
Figure 3.2: Dose-volume histograms (upper) and sample dose-distributions (lower) of the AAPM TG-119 phantom plan after undergoing FMO and aperture sequencing (dotted line) and when optimized with the FIDAO (solid line) and the standard (dashed line) DAO algorithms. The cross-section of the axial, sagittal, and coronal planes are shown as dashed lines on the dose distributions.
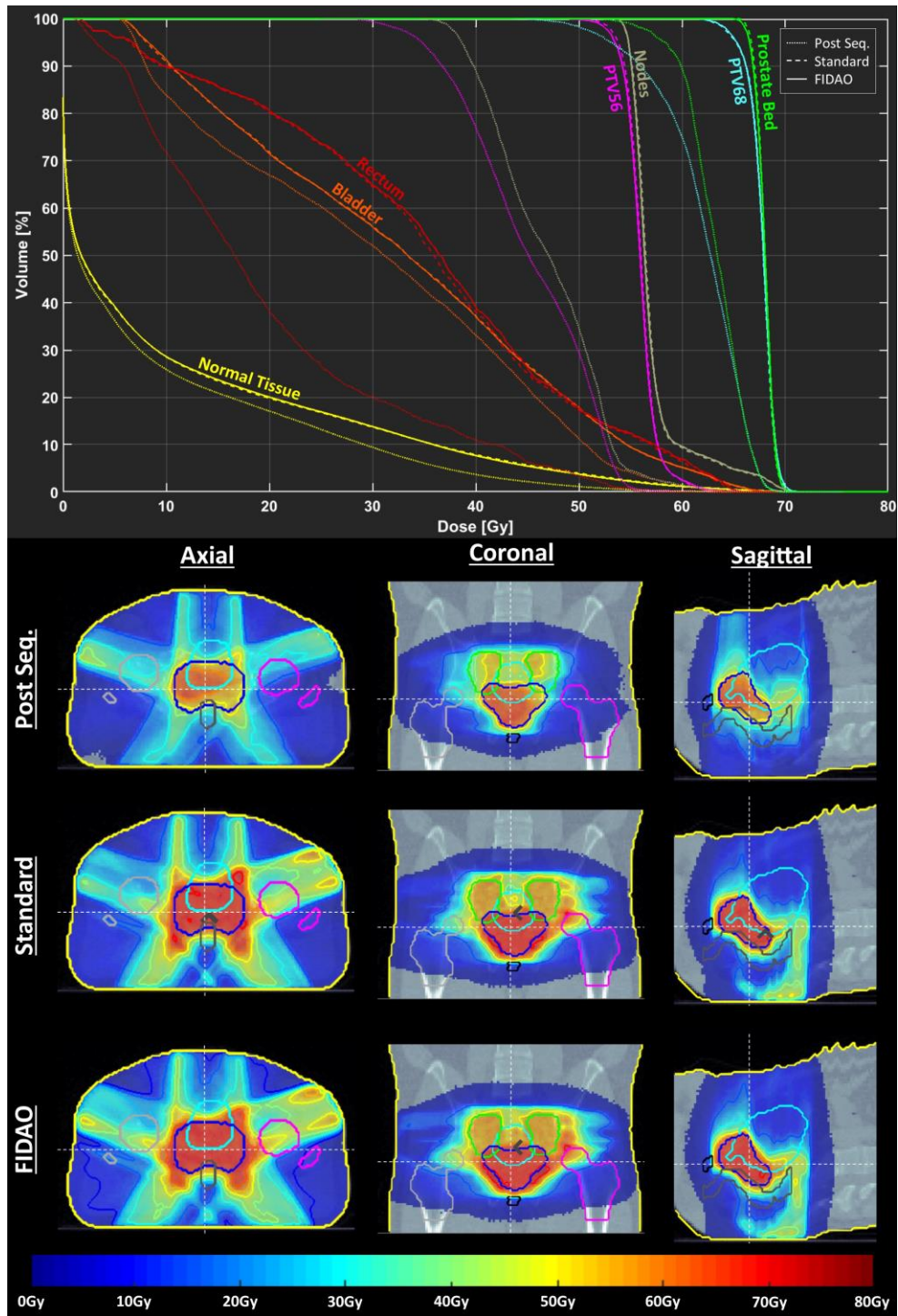
Figure 3.3: Dose-volume histograms (upper) and sample dose-distributions (lower) of the prostate case after undergoing FMO and aperture sequencing (dotted line) and when optimized with the FIDAO (solid line) and the standard (dashed line) DAO algorithms. The cross-section of the axial, sagittal, and coronal planes are shown as dashed lines on the dose distributions.
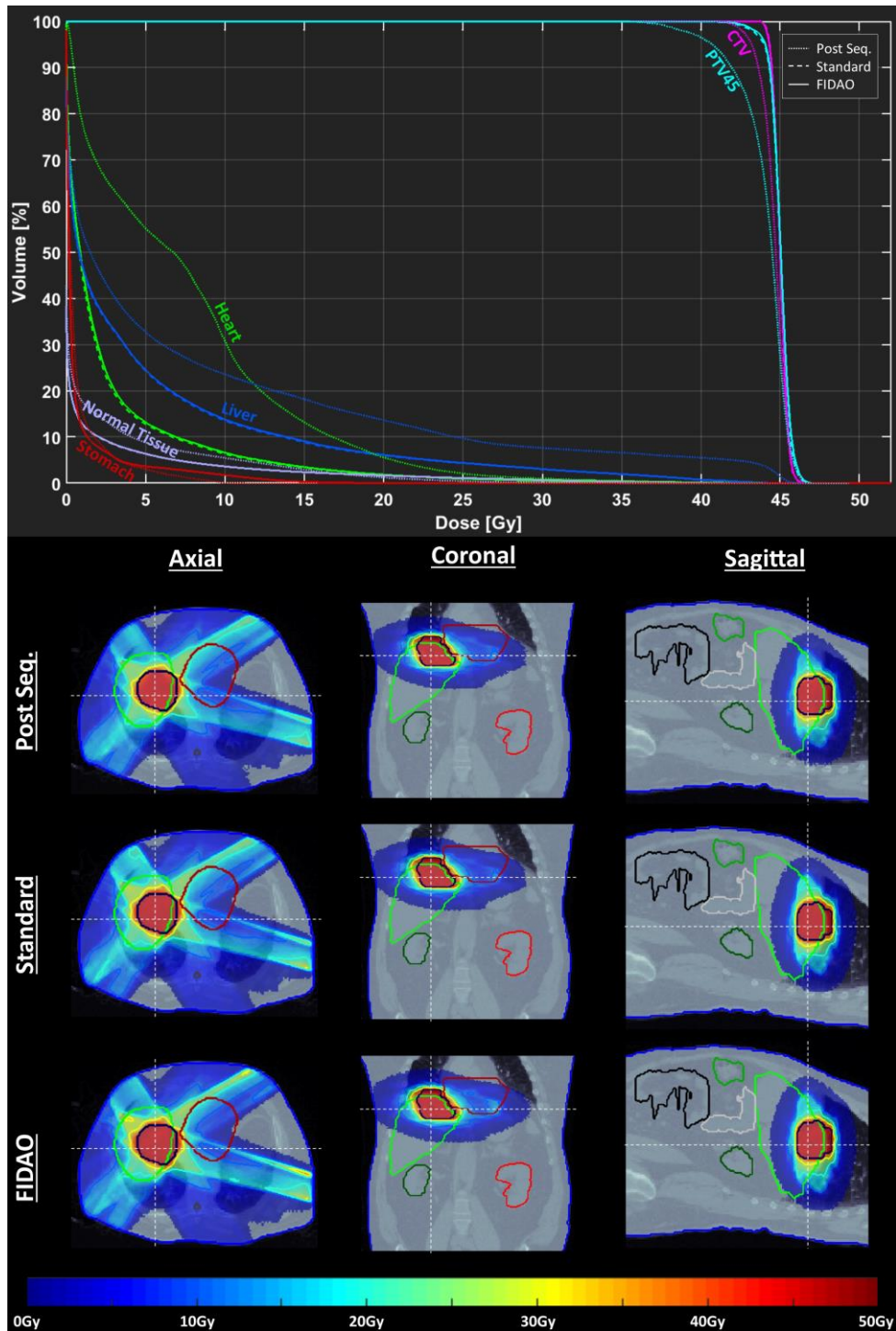
Figure 3.4: Dose-volume histograms (upper) and sample dose-distributions (lower) of the liver case after undergoing FMO and aperture sequencing (dotted line) and when optimized with the FIDAO (solid line) and the standard (dashed line) DAO algorithms. The cross-section of the axial, sagittal, and coronal planes are shown as dashed lines on the dose distributions.
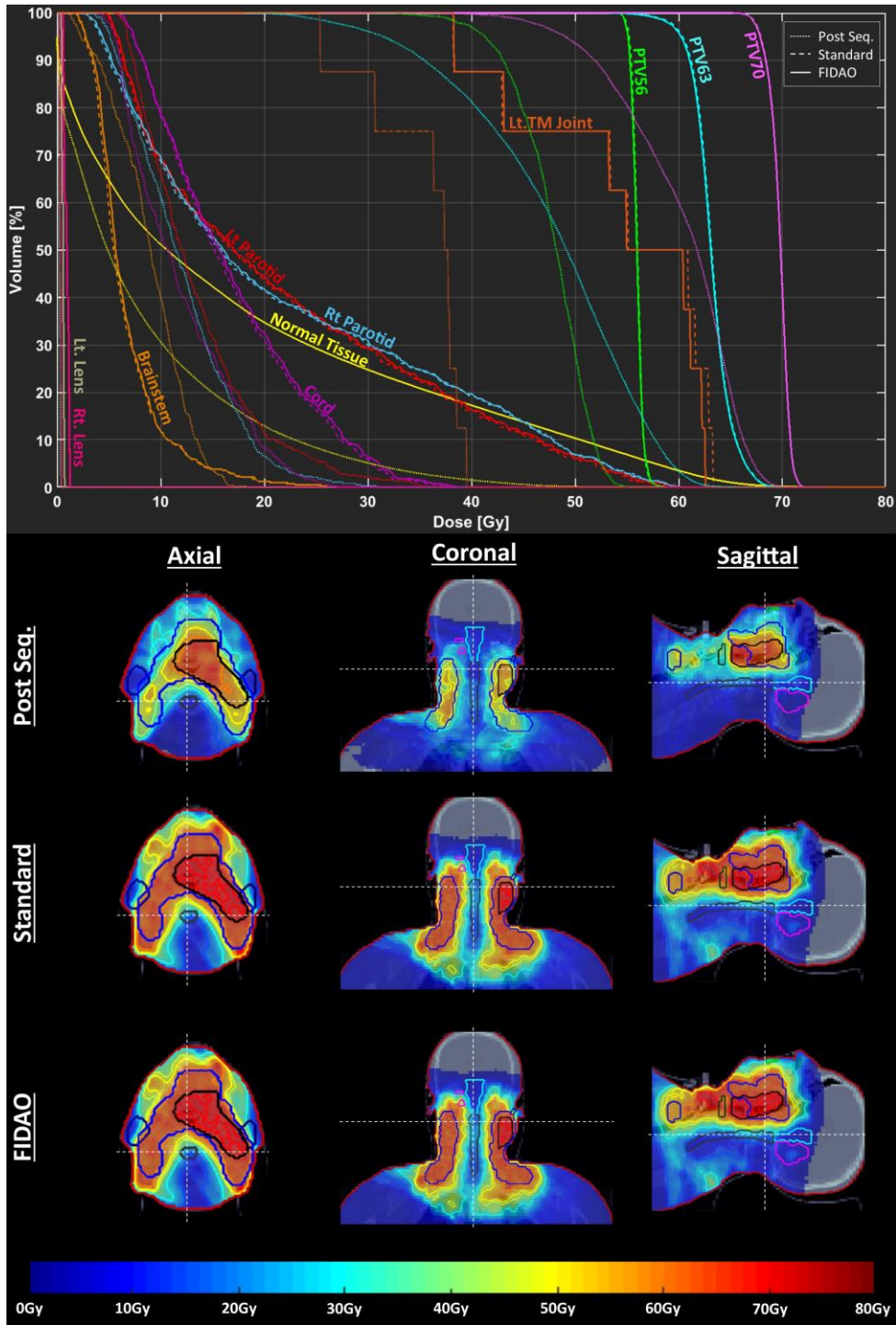
Figure 3.5: Dose-volume histograms (upper) and sample dose-distributions (lower) of the head-and-neck case after undergoing FMO and aperture sequencing (dotted line) and when optimized with the FIDAO (solid line) and the standard (dashed line) DAO algorithms. The cross-section of the axial, sagittal, and coronal planes are shown as dashed lines on the dose distributions.

3.4　Discussion

The algorithms used for DAO and FMO are computationally demanding. This is primarily due to the repeated use of the pencil-beam dose matrix, $\boldsymbol{d}$, to evaluate the objective function and compute its gradient vector during optimization. As shown in Table 3.2, this matrix has millions of elements and takes several gigabytes of memory to store. The size of this matrix not only impacts the amount of memory required to perform FMO or DAO, but also the time it takes to execute a computation involving it, as the computation speed will be limited by the rate at which the computer can transfer the dose matrix elements from memory to the processor's arithmetic unit as well as the processor's clock speed [10,12]. In response to this limit, many academic and commercial groups have developed FMO and DAO algorithms that utilize the multiple processors available on modern CPUs and GPUs [7,9-12]. With these multicore units, the computation can be performed in parallel, allowing for the individual computations and the overall optimization to be completed faster. Others have also developed using a novel non-voxel-based broad-beam (NVBB) framework when deriving the DAO problem, which eliminates the pencil-beam dose matrix from the DAO problem entirely [20,21].

In this work, we extended a previously developed FMO algorithm called FIDO to perform DAO. This algorithm uses the objective function's Hessian matrix and a reference gradient vector (or $\boldsymbol{\alpha}$ and $\vec{\beta}$ as they were denoted in the original FIDO papers), via second-order Taylor series expansion, to compute the objective function value and its gradient vector during optimization [13-15]. Using the $\boldsymbol{\alpha}$ and $\vec{\beta}$ matrices is advantageous as they often have considerably fewer elements than the pencil-beam dose matrix, and therefore any computations involving them will have smaller data transfer overheads and require fewer operations. This can be illustrated with some of the values found in Table 3.2. If the pencil-beam dose matrix is stored in a compressed sparse row or column format, the number of operations performed during matrix-vector multiplication with the pencil-beam dose matrix (e.g. $\boldsymbol{d}\vec{\tau}$ in the standard objective function) is proportional to the number of non-zero elements in the matrix [22]. On the other hand, the same operation with $\boldsymbol{\alpha}$ (e.g. $\boldsymbol{\alpha}\vec{\tau}$ in the FIDAO objective function) is proportional to the squared number of pencil-beams in the plan. From Table 3.2, we can see that the squared number of

pencil-beams in each plan is substantially smaller than the number of non-zero element in the pencil-beam dose matrix. As a result, FIDAO could evaluate the objective function value or compute its gradient vector substantially faster, resulting in an overall faster optimization.

While a similar algorithm could have been formulated from the standard objective function's (Equation 1) Hessian matrix and gradient vector, this formulation would likely have been less efficient than FIDAO due to the computation times for the Hessian matrix. Notice from Table 3.2 that a relatively large amount of time is spent pre-calculating $\boldsymbol{\alpha}$ and $\vec{\beta}$. This time is mostly spent on computing the PTV component of $\boldsymbol{\alpha}$, as the PTV objectives contributes to every element in $\boldsymbol{\alpha}$ whereas the OAR objectives only contribute to the diagonal elements of $\boldsymbol{\alpha}$. The fact that the OARs only contribute to the diagonal elements of $\boldsymbol{\alpha}$ is a result of the reformulation of the OAR objective function in FIDO. If we were to use the standard objective function, the OARs would then contribute to every element in $\boldsymbol{\alpha}$, which would substantially increase the computation time for the Hessian matrix especially when very large OARs have planning objectives such as the normal unspecified tissue. Furthermore, if we were to use the standard equations for dose-volume objectives, we would have to update every element in $\boldsymbol{\alpha}$ and $\vec{\beta}$ as opposed to just $\vec{\beta}$ and the diagonal elements of $\boldsymbol{\alpha}$ when using the spatially varying penalty weight and prescribed dose in FIDO. Collectively, this makes computing and updating the Hessian matrix and gradient vector of the FIDO objective function substantially easier than with the standard objective function.

If given the same penalty weight, p_{oar}, and effective fluence map, τ, the standard equation for the OAR objective will contribute more to the objective function value than the reformulated FIDO equation. That is,

$$p_{oar} \sum_x \left(\sum_i d_{xi} \, \tau_i \right)^2 \geq p_{oar} \sum_x \sum_i d_{xi}^2 \, \tau_i^2 \, .$$

This inequality means that FIDAO may need a higher OAR penalty weight than the standard objective function in order to achieve similar OAR sparing, as was observed in the TG-119 phantom case from this study. Moreover, this reformulation could cause

FIDAO to be less sensitive to OAR maximum doses as FIDAO penalizes the individual dose contributed by each pencil beam instead of the net dose contributed by all pencil beams. This can be counteracted by spatially increasing the OAR penalty weight in voxels with a net dose above some tolerance dose, as demonstrated in Figure 3.6 in the Appendix.

The optimization times obtained with FIDAO are similar to the reported optimization times of GPU-based DAO algorithms. For instance, Men *et al.* showed that their GPU-based DAO algorithm could optimize an IMRT treatment plan in 0.7s to 3.8s, whereas our FIDAO algorithm could optimize a plan in 0.3s to 6.7s *without any parallelization* [7]. Note that the fast optimization times reported in their study can be partially attributed to the down-sampling of unspecified tissue (i.e. voxels that were outside the PTV or contoured OARs), which resulted in much smaller pencil-beam dose matrices than in our present study. For instance, the number of non-zero elements in d in their study was at least 25 times smaller than in this study. Therefore, their GPU-based DAO algorithm would take considerably longer if executed on the same cases reported here. That said, our FIDAO algorithm does require an additional 2 to 60 s to pre-compute α and $\vec{\beta}$ whereas the GPU-based method does not. This computation, however, can be parallelized in addition to the evaluation of FIDAO's objective function and the computation of its gradient vector.

Note that the much better OAR sparing in the post sequencing prostate plan (Figure 3.3) and head-and-neck plan (Figure 3.5) was only achievable due to the *severe* and *clinically unacceptable* under-dosing of the PTVs (more than 25% under-dosing for D_{95} of PTVs). The plans obtained with FIDAO and the standard DAO algorithm are more clinically relevant as they provide the best possible OAR sparing achievable while also obtaining a clinically acceptable level of PTV coverage.

It is well known that gradient-based DAO methods may become trapped at a local minimum due to the non-convex nature of the objective function. However, this problem can be minimized by starting the DAO at a good starting point as done in many commercial treatment planning systems. For instance, we can first perform fluence map

optimization with FIDO which finds the global minimum of the objective function. After MLC leaf sequencing, we can then fine-tune these apertures using FIDAO. We can also employ stochastic optimization methods like simulated annealing and genetic algorithms in lieu of a gradient-based approach, as these algorithms can escape from local minima. For this proof-of-concept study, we chose to use a gradient-based optimization method due to its accessibility and the wide-spread use of gradient-based DAO methods in commercial treatment planning systems. However, similar performance improvements should be expected when using FIDAO with any stochastic, greedy, or other first-order optimization methods due to the much more efficient evaluation of the expanded FIDO objective function compared to the standard objective function.

FIDAOs optimization time is minimally impacted by the size or resolution of the dose grid. Specifically, only the initial computation and updating of the $\boldsymbol{\alpha}$ and $\vec{\beta}$ matrices will be affected by the resolution or size of the dose grid, whereas the computation of the objective function value and its gradient vector during optimization is only affected by the number of pencil-beams in the plan. This makes FIDAO very desirable for optimizing stereotactic body radiation therapy (SBRT) and stereotactic radiosurgery (SRS) treatment plans, where an isotropic high-resolution dose grid size of 2 mm or less is recommended [23]. Conversely, it is unclear whether FIDAO may be suitable for optimizing volumetric modulated arc therapy (VMAT) plans, as VMAT plans typically have tens of thousands of pencil-beams which could drastically decrease the efficiency of evaluating the FIDAO objective function. Moreover, interior point methods are known to be inefficient for large-scale optimization problems such as those in VMAT planning, so a different optimization method may also be necessary. This will need to be assessed in a future study that incorporates VMAT-related delivery constraints such as the maximum MLC distance due to maximum MLC-travel speeds and gantry-rotation speeds.

3.5 Conclusions

In this work, a fast inverse direct aperture optimization (FIDAO) algorithm was developed based on the fast inverse dose optimization (FIDO) method. A prototype of this algorithm was developed in MATLAB and compared against an independent DAO

algorithm on four test cases. In all four cases, the prototype algorithm produced comparable step-and-shoot IMRT plans with gains of 70-200 times in optimization speed. The study demonstrates promising speed enhancements for direct aperture optimization using FIDAO without necessitating parallel computing strategies.

3.6 Appendix

Let $d(x)$ be the dose deposited to voxel x, and let p_{dvh} and d_{tol} be the objective penalty weight and tolerance dose assigned to a dose-volume objective. Also, let $\Delta d(x) = d(x) - d_{tol}$ and $m(x)$ denote the percent that the voxel dose is above or below the tolerance dose,

$$m(x) = \left| \frac{\Delta d(x)}{d_{tol}} \right|.$$

If a maximum or minimum point dose objective is applied to the PTV, FIDAO uses a spatially varying prescription dose to increase or decrease the dose in non-compliant voxels. By varying the prescription dose instead of the penalty weight, FIDAO can avoid having to recompute the full Hessian matrix. Specifically, the prescription dose of voxels above or below the threshold point dose will vary according to:

$$d_{ptv}(x) = \begin{cases} \left(1 \pm \left(\frac{p_{dvh}}{p_{ptv}} \right) m(x) \right) d_{ptv}, & if \ m(x) < 0.03 \\ \left(1 \pm \left(\frac{p_{dvh}}{p_{ptv}} \right) 0.03 \right) d_{ptv}, & if \ m(x) > 0.03 \end{cases},$$

while all other voxels will maintain the user prescribed d_{ptv} dose [14]. Note that the $\pm$ sign will be positive if it's a minimum dose objective, and negative if it's a maximum dose objective. This equation is equivalent to increasing or decreasing the prescription dose by up to 3%, when the penalty weight of the dose-volume objective is the same as p_{ptv}. If the dose-volume objective is weighted more than the homogeneity objective ($p_{dvh} > p_{ptv}$), the prescription dose will be varied by more than 3% and vice versa.

If a maximum point dose objective is applied to an OAR, the OAR objective penalty weight $p_{oar}(x)$ for voxels above the tolerance dose is varied by,

$$p_{oar}(x) = \begin{cases} \left(1 + \left(\dfrac{p_{dvh}}{p_{oar}}\right)\dfrac{\Delta d(x)}{d_1}\right)p_{oar}, & if \ \Delta d(x) < d_{thresh} \\[3mm] \left(1 + \left(\dfrac{p_{dvh}}{p_{oar}}\right)\dfrac{d_{thresh}}{d_1}\right)p_{oar}, & if \ \Delta d(x) > d_{thresh} \end{cases},$$

where d_{thresh} is a threshold dose chosen to be 9 Gy, and $d_1 = 1$ Gy so that the penalty weight remains dimension-less. This equation is equivalent to increasing the penalty weight by up to a factor of 10 when the penalty weight of the dose-volume objective is the same as p_{oar}. If the dose-volume objective is weighted more than the OAR objective ($p_{dvh} > p_{oar}$), the penalty weight will be increased by more than a factor of 10 [14].

If the minimum (or maximum) dose-volume objective for the PTV is volume based, the prescribed dose is increased (or decreased) more for voxels that are closer to the threshold dose. Similarly, if the dose-volume objective for an OAR is volume based, the penalty weight is increased more for voxels that are closer to the threshold dose.

Figure 3.6 shows the DVHs of the prostate case from this study after FIDAO optimization with (solid line) and without (dashed line) a minimum PTV dose objective (upper), a maximum dose objective to 50% of the rectum and bladder (middle), and a maximum rectum point dose objective (lower).
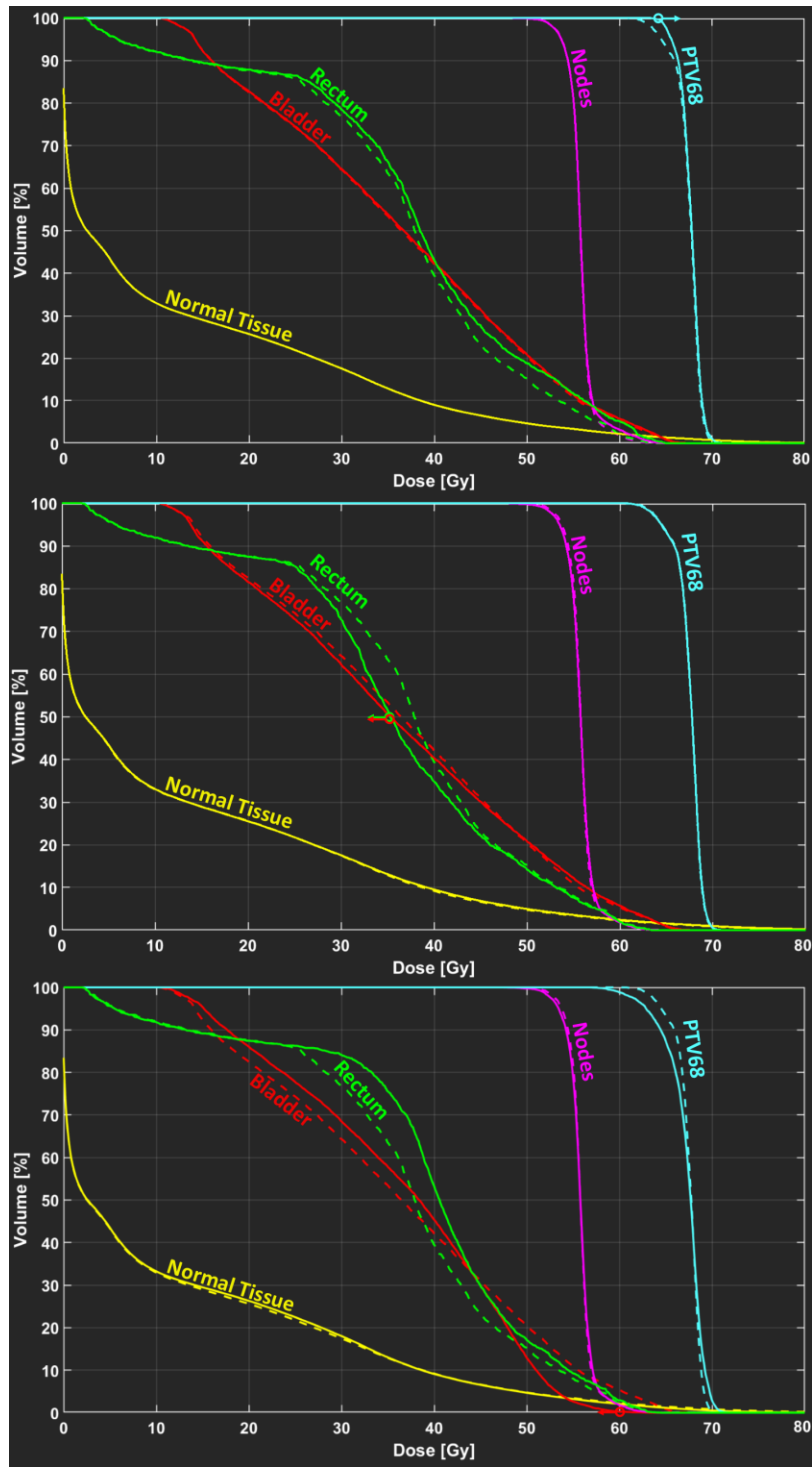
Figure 3.6: Dose-volume histograms of the prostate case after DAO with FIDAO with (solid) and without (dashed) a minimum 64.6 Gy PTV dose objective (upper), a maximum 35 Gy dose objective to 50% of the rectum and bladder (middle), and a maximum 60 Gy point dose objective to the rectum (lower) as indicated by the circles and arrow markers.

3.7 Acknowledgements

3.8 Disclosure

3.9 References

1. Shepard DM, Earl MA, Li XA, Naqvi S, and Yu C. Direct aperture optimization: A turnkey solution for step-and-shoot IMRT. *Med. Phys.* 2002; **29** (6): 1007-18.

2. Li Y, Yao J, and Yao D. Genetic algorithm based deliverable segments optimization for static intensity-modulated radiotherapy. *Phys. Med. Biol.* 2003; **48** (20): 3353-74.

3. Hårdemark B, Liander A, Rehbinder H, and Löf J. P³IMRT. Direct machine parameter optimization. *Pinnacle white paper*, Nr. 4535 983 02483, Philips (2004).

4. Romeijn HE, Ahuja RK, Dempsey JF, and Kumar A. A column generation approach to radiation therapy treatment planning using aperture modulation. *SIAM J. Optim.* 2005; **15** (3): 838-62.

5. Men C, Romeijn HE, Taşkin ZC, and Dempsey JF. An exact approach to direct aperture optimization in IMRT treatment planning. *Phys. Med. Biol.* 2007; **52** (24): 7333-52.

6. Carlsson F. Combining segment generation with direct step-and-shoot optimization in intensity-modulated radiation therapy. *Med. Phys.* 2008; **35** (9): 3828-38.

7. Men C, Jia X, and Jiang SB. GPU-based ultra-fast direct aperture optimization for online adaptive radiation therapy. *Phys. Med. Biol.* 2010; **55** (15): 4309-19.

8. Cassioli A and Unkelbach J. Aperture shape optimization for IMRT treatment planning. *Phys. Med. Biol.* 2012; **58** (2): 301-18.

9. Wild E, Bangert M, Nill S, and Oelfke U. Noncoplanar VMAT for nasopharyngeal tumors: Plan quality versus treatment time. *Med. Phys.* 2015; **42** (5): 2157-68.

10. Jia X, Ziegenhein P, and Jiang SB. GPU-based high-performance computing for radiation therapy. *Phys. Med. Biol.* 2014; **59** (4): R151-82.

11. Men C, Gu X, Choi D, et al. GPU-based ultrafast IMRT plan optimization. *Phys. Med. Biol.* 2009; **54** (21): 6565-73.

12. Ziegenhein P, Kamerling CP, Bangert M, Kunkel J, and Oelfke U. Performance-optimized clinical IMRT planning on modern CPUs. *Phys. Med. Biol.* 2013; **58** (11): 3705-15.

13. Goldman SP, Chen JZ and Battista JJ. Feasibility of a fast inverse dose optimization algorithm for IMRT via matrix inversion without negative beamlet intensities. *Med. Phys.* 2005; **32** (9): 3007-16.

14. Goldman SP, Turnbull D, Johnson C, Chen JZ, and Battista JJ. Real-time fast inverse dose optimization for image guided adaptive radiation therapy–Enhancements to fast inverse dose optimization (FIDO). *J Appl. Phys.* 2009; **105**: 102008.

15. Nocedal J and Wright SJ. *Numerical Optimization.* 2nd Edition. New York, NY: Springer Science+Business Media, LLC; 2006.

16. Wieser HP, Cisternas E, Wahl N, Ulrich S, Stadler A, Mescher H, et al. Development of the open-source dose calculation and optimization toolkit matRad. *Med. Phys.* 2017; **44** (6): 2556-68.

17. Wächter A, Biegler LT. On the implementation of an interior-point filter line-search algorithm or large-scale nonlinear programming. Math Program. 2006; **106** (1): 25–57.

18. Craft D, Bangert M, Long T, Papp D, and Unkelbach J. Shared data for intensity modulated radiation therapy (IMRT) optimization research: the CORT dataset. *GigaScience* 2014; **3**:37.

19. Siochi RA. Minimizing static intensity modulation delivery time using an intensity solid paradigm. *Int J Radiat Oncol Biol Phys* 1999; **43** (3): 671-80.

20. Lu W. A non-voxel-based broad-beam (NVBB) framework for IMRT treatment planning. *Phys. Med. Biol.* 2010; **55** (23): 7175-210.

21. Tomotherapy, Accuray. VoLO™ (Voxel-less Optimization) Technology. *Accuray white paper*, Nr. 500917, Accuray (2012).

22. Blelloch, GE. Programming parallel algorithms. *Communications of the ACM* 1996; **39** (3): 85-97.

23. Benedict SH, Yenice KM, Followill D, et al. Stereotactic body radiation therapy: the report of AAPM Task Group 101. *Med Phys* 2010; **37**(8): 4078-101.

Chapter 4 – A fast inverse direct aperture optimization algorithm for volumetric modulated arc therapy

This chapter describes initial work on a FIDAO algorithm for VMAT planning. It will be converted to a manuscript for a technical note entitled "A fast inverse direct aperture optimization algorithm for volume-modulated arc therapy" by Michael MacFarlane, Douglas Hoover, Eugene Wong, Jerry J. Battista, and Jeff Z. Chen.

4.1   Introduction

In a recent article, our group developed a new direct aperture optimization (DAO) algorithm called fast inverse direct aperture optimization (FIDAO) [1]. FIDAO extends a previously implemented fluence map optimization algorithm called fast inverse dose optimization (FIDO) for DAO [1-3]. Specifically, instead of using the conventional objective function, FIDAO used a modified quadratic objective function (similar to FIDO) to efficiently compute the objective function value and gradient vector during DAO.

The advantage of FIDAO is that the number of operations (m) performed when evaluating the modified quadratic objective function is proportional to the squared number of pencil beams in the plan, whereas the number of operations (n) performed when evaluating the conventional objective function is proportional to the number of non-zero elements in a pre-calculated dose matrix. For fixed-gantry intensity-modulated radiotherapy (IMRT), $m \ll n$, as a result FIDAO executes up 200-times faster when compared to standard DAO methods as described in Chapter 3 [1]. No significant differences in plan quality was observed between the plans optimized with FIDAO and the standard method.

For volume-modulated arc therapy (VMAT) plans, the number of pencil beams in a plan can be significantly larger than in IMRT plans. As a result, it is possible for $m \sim n$ or $m > n$, especially if the pre-calculated dose matrix is down-sampled in unspecified normal tissue, as is done by some DAO algorithms for optimization [4,5]. Furthermore, VMAT uses a different planning procedure than IMRT and requires additional

constraints, which could possibly impact the performance of FIDAO. Therefore, the goal of this work was to extend FIDAO for VMAT planning, and to evaluate whether FIDAO can also offer a performance advantage for VMAT treatment planning, as it did for fixed-field IMRT.

4.2 Methods and Materials

A prototype FIDAO algorithm for VMAT treatment planning was developed in MATLAB v9.4 (Mathworks Inc, Natick, MA) using the open-source treatment planning toolkit matRad (v2.2 – dev_VMAT build) [6,7]. This version of the matRad toolkit includes an implementation of the SmartArc VMAT planning algorithm [7,8]. Specifically, to generate a VMAT plan, this algorithm first performs fluence map optimization (FMO) and aperture sequencing on a set of coarsely equispaced beams [9]. The sequenced apertures are then redistributed along the arc trajectory at a finer angular spacing (typically 4°). Afterwards, the arc undergoes DAO where VMAT-related delivery constraints are enforced.

VMAT treatment plans were created on the AAPM TG-119 phantom dataset as well as the sample prostate and liver cancer cases that are supplied with the matRad toolkit [6,10]. The voxel size of these datasets was 3x3x2.5 mm^3 in the TG-119 case, 3x3x3 mm^3 in the prostate case, and 3x3x2.5 mm^3 in the liver case. The dose calculation matrix, $\boldsymbol{d}_{xi}$, was pre-calculated using matRad's singular value decomposition (SVD) dose computation algorithm [11]. The size of the pencil beams was set to 5x5 mm^2. To improve the standard DAO and FMO algorithms speed, the dose calculation matrix was down-sampled by a factor of 2 in the unspecified normal tissue. Note, however, that the full (non-down-sampled) dose calculation matrix was used, after optimization, for the final dose calculations and plan evaluation. In all three cases, the plans underwent FMO at an angular spacing of 28°, followed by aperture sequencing and arc sequencing with a 4° angular spacing. The planning objectives that were used in each plan are listed in Table 4.1. After arc sequencing, the plans underwent DAO using either the standard VMAT DAO algorithm that was included with the matRad toolkit, or the FIDAO algorithm.

The standard DAO algorithm used an interior-point optimization method to solve:

$$\underset{\vec{l}, \vec{w}}{\text{minimize}} \quad f_1(\vec{l}, \vec{w})$$

$$\text{subject to} \quad \boldsymbol{C}(\vec{l}, \vec{w}) \geq \vec{b}$$

[6,12]. In this problem, $\vec{l}$ and $\vec{w}$ stand for the aperture leaf positions and weights respectively, $f_1(\vec{l}, \vec{w})$ is the conventional objective function [6], and $\boldsymbol{C}(\vec{l}, \vec{w}) \geq \vec{b}$ are the constraints which include a non-negative aperture weight constraint, boundary limits on the leaf positions, minimum and maximum leaf travel speed of 0 cm/s and 6 cm/s, minimum and maximum gantry rotation speed of 0 °/s and 6 °/s, and a minimum and maximum monitor unit (MU) dose rate of 75 MU/min and 600 MU/min, respectively [7]. These were the default machine-based delivery constraint that came with the matRad toolkit.

FIDAO used the same interior-point optimization method to solve its DAO problem. Compared to the standard DAO algorithms, FIDAO had the following changes: (1) prior to optimization, FIDAO computed and stored the modified objective function's Hessian matrix ($\boldsymbol{\alpha}$) and $\vec{\beta}$ *via* Equation 4 in Chapter 3.2.1; (2) Equations 8 & 10 in Chapter 3.2.2 were used for computing the objective function value and its gradient vector, respectively; and (3) if dose-volume objectives were included in the optimization, an intermediate recalculation of the Hessian matrix would be performed as describe in Chapter 3.2.3.

Effectively, FIDAO and the standard DAO algorithm are the same as they were in Chapter 3, with the exception that both VMAT DAO problems are limited to a single aperture at each gantry angle per arc, and that the DAO problems in this study include additional VMAT-related delivery constraints such as maximum gantry-rotation speed and dose rate.

Planning was performed on the same desktop computer running Windows 7 with an Intel i7-3930K (3.2 GHz) CPU and 64 GB of RAM. To the best of our knowledge, no CPU or GPU parallelization was utilized in matRad's DAO algorithm's code [6,7]. Similarly, no parallel processing was used in the code for FIDAO. The total optimization

time and number of iterations were recorded for both FIDAO the standard DAO algorithm. The FIDAO and matRad optimized plans were also compared based on their dose-volume histograms and 3D dose distributions.

Table 4.1: Optimization objectives used by both algorithms.

No.	Site	Beams (Apertures)	Optimization Objectives
1.	TG-119	1 360° Arc (91)	• Uniform 50 Gy dose to the C-shaped Target. • Minimal dose to the core OAR and body. • Maximum point dose of 50 Gy in the body, and 25 Gy in the core OAR.
2.	Liver	1 360° Arc (91)	• Uniform 45 Gy dose to the PTV. • Minimal dose to the healthy liver, heart & normal tissue. • Maximum point dose of 40 Gy in the normal tissue.
3.	Prostate	1 360° Arc (91)	• Uniform 68 Gy and 56 Gy dose to the PTV and Nodes. • Minimal dose to the rectum, bladder & normal tissue. • Maximum point dose of 50 Gy in the normal tissue, rectum, and bladder.

4.3 Results

Details about the test cases and the algorithms' performance are listed in Table 4.2. Note that the size of the Hessian matrix (α) is proportional to the squared number of pencil beams (column 3) in the plan, while the size of the pencil-beam dose matrix is the number of pencil beams times the number of voxels (column 4). Also, note that the listed computation times for FIDAO's α and $\vec{\beta}$ (column 7) refers to their one-time *initial* computation time prior to DAO. The time spent updating α and $\vec{\beta}$ when dose-volume objectives were present is included in the *total* FIDAO optimization time (column 8).

Table 4.2: Information related to the size of the optimization problem, and each algorithm's performance.

No.	Site	Pencil Beams	Voxels [x 10^6]	Non-zero $\mathbf{d}_{xi}$ [x 10^8]	Voxels in PTV [x10^3]	$\alpha, \vec{\beta}$ Initialization	Optimization Time (Iter.) FIDAO	Optimization Time (Iter.) Standard
1.	TG-119	32,123	3.60	4.88	7.5	40.9 s	64.9 s (245)	602 s (275)
2.	Liver	20,293	7.91	8.38	7.0	18.7 s	25 s (85)	803 s (159)
3.	Prostate	52,234	3.05	10.52	16.3	197.8 s	98.6 s (174)	754.3 s (149)

Abbreviations: Iter, Iterations.

Sample dose-volume histograms (DVH) for each case are shown in Figure 4.1-Figure 4.3. To demonstrate the effectiveness of these DAO algorithms, Figure 4.1-Figure 4.3 also include DVHs of the plan prior to DAO (post FMO, aperture and arc sequencing).

As demonstrated by the comparison of DVHs, FIDAO and the standard DAO algorithm converged to plans of similar quality. In the liver case however, the FIDAO plan spared the stomach slightly more whereas the standard DAO plan spared the spinal cord slightly more. Similarly, in the prostate case, the standard DAO plan and FIDAO plan spared the femoral heads and rectum slightly differently. In terms of optimization time, FIDAO obtained its solutions about 7-32 times faster than the standard DAO algorithm, or 2.5-18.3 times faster if the one-time calculation time for α and $\vec{\beta}$ is included.
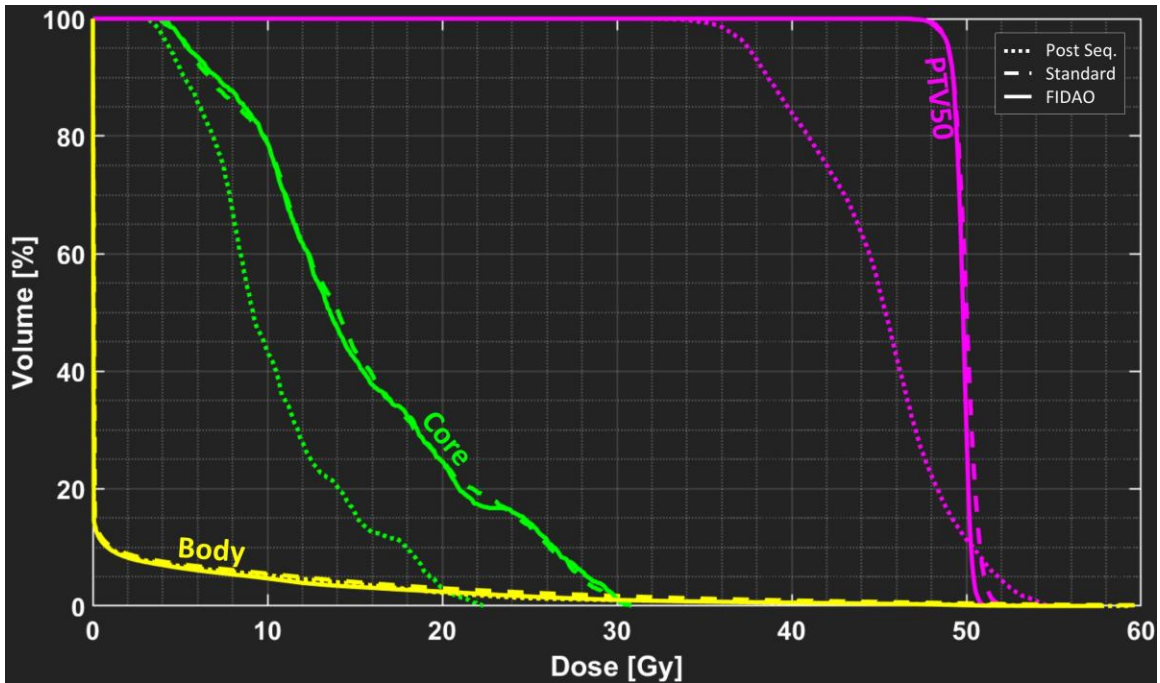
Figure 4.1: Dose-volume histograms of the AAPM TG-119 phantom plan after undergoing FMO and aperture sequencing (dotted line) and when optimized with the FIDAO (solid line) and the standard (dashed line) DAO algorithms.
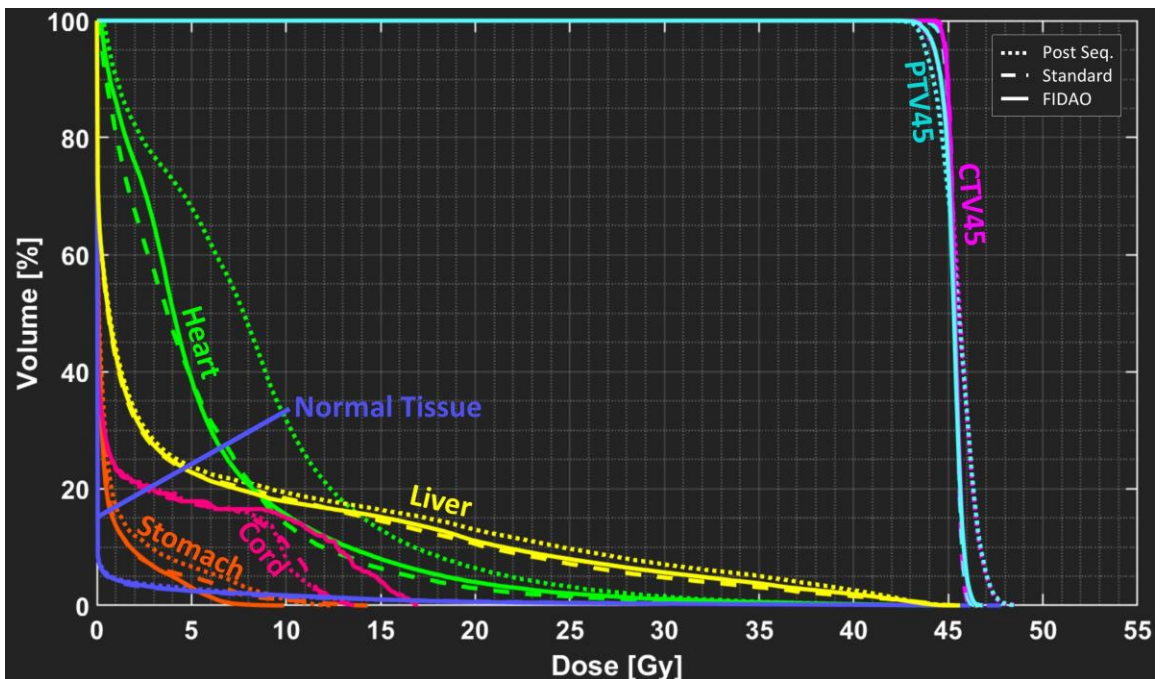
Figure 4.2: Dose-volume histograms of the liver plan after undergoing FMO and aperture sequencing (dotted line) and when optimized with the FIDAO (solid line) and the standard (dashed line) DAO algorithms.
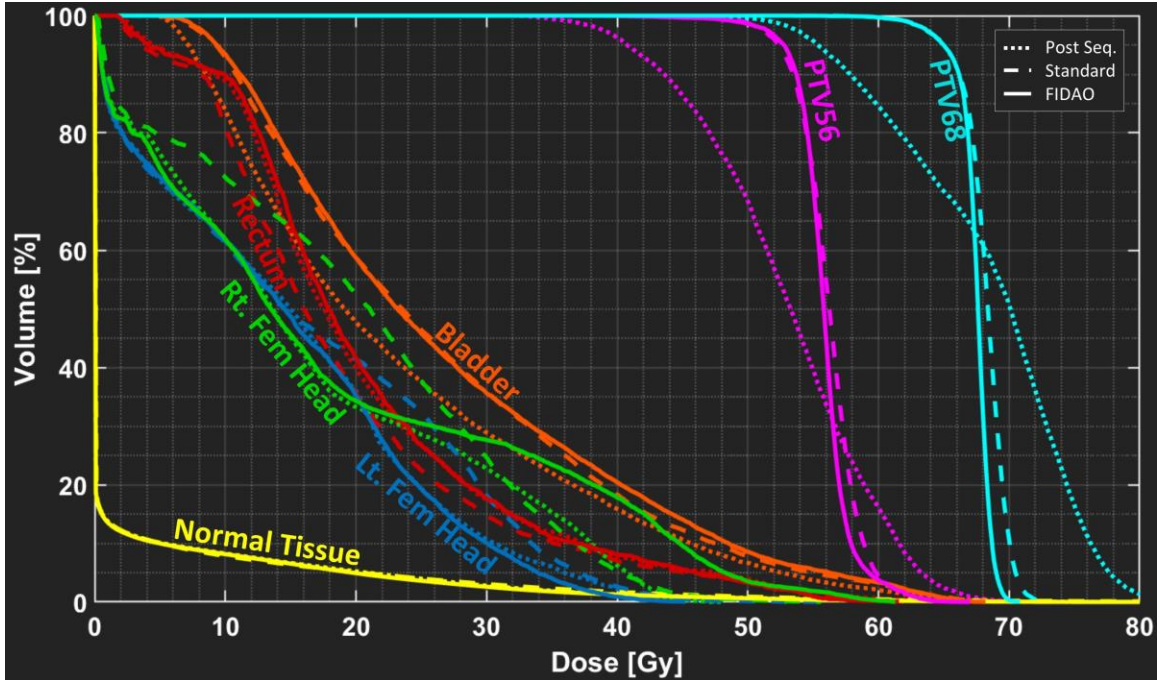
Figure 4.3: Dose-volume histograms of the prostate plan after undergoing FMO and aperture sequencing (dotted line) and when optimized with the FIDAO (solid line) and the standard (dashed line) DAO algorithms.

4.4 Discussion

In this work, we extended FIDAO for VMAT treatment planning and evaluated its performance relative to a standard VMAT DAO algorithm in three cases. As shown in Table 4.2, FIDAO reduced the optimization time for VMAT by up to a factor of 18 (when the pre-calculation times for α and $\vec{\beta}$ are included). The plan quality obtained with FIDAO was on par with the standard DAO method, although some minor differences could be observed when using the same planning objectives (Figure 4.1 - Figure 4.3).

The source of FIDAO's superior performance lies in the lower computational cost of computing FIDAO's objective function value and gradient vector. As discussed in the introduction, the number of operations (m) performed when evaluating FIDAO's objective function is proportional to the squared number of pencil beams in the plan (Table 4.2, column 3 squared), whereas the number of operations (n) performed when evaluating the conventional objective function is proportional to the number of non-zero elements in a pre-calculated dose matrix (Table 4.2, column 5). In most cases, m is much

lower than n, meaning that FIDAO can compute its objective function value and gradient vector more efficiently. Moreover, FIDAO's gradient vector can be computed with little additional cost once the objective function value is computed, and vice versa, by storing the result of $\boldsymbol{a}\vec{\tau} - \vec{\beta}$. This cannot be done when using the standard objective function.

The optimization times observed in this study are approaching the reported optimization times by commercial treatment planning systems, and by Men *et al.* for their GPU-based DAO algorithm, for VMAT planning [13]. For instance, Men *et al.* reported VMAT optimization times in the range of $18 - 31$ s when parallelized on an NVIDIA Tesla C1060 GPU, whereas we observed optimization times of $25 - 98.6$s, on a standard desktop CPU, without any parallelization. There are a few key differences between our study and Men *et al.* that are worth noting. First, the plans optimized by Men *et al.* are considerably smaller than the test cases presented in this study. The largest plan in their patient cohort had 5.5×10^7 non-zero elements in its dose calculation matrix, whereas the smallest plan in this study has 4.8×10^8 non-zero elements. Therefore, it would likely take considerably longer than $18 - 31$ s for their algorithm to execute on the cases presented in this study. Secondly, the algorithm implemented by Men *et al.* is a column generation approach that sequentially adds apertures to the plan based on a pricing problem [5,13]. It does not perform DAO after aperture and arc sequencing as is done in SmartArc (Philips Healthcare, Fitchburg, USA) and the algorithm implemented in this study. Therefore, to make a fair comparison, we should also incorporate the $\boldsymbol{\alpha}$ computation times (column 7 of Table 4.2) and the approximate 120 s that was spent on FMO, aperture and arc sequencing performed in our method. While this adds a considerable amount of time to FIDAO's overall planning time, note that the $\boldsymbol{\alpha}$ calculation can be accelerated greatly with GPUs (Equation 4 in Chapter 3.2.1 is a data-heavy computation) and we can eliminate most of the FMO time by performing FMO with FIDO [2,3]. Therefore, collectively, we anticipate that FIDAO would take less time than the algorithm developed by Men *et al.* when implemented on the same system and tested on the same cases.

While the time complexity (number of operations) of FIDAO may be lower, the spatial complexity (memory usage) of FIDAO is considerably higher. Specifically, FIDAO requires us to compute and store the objective function's Hessian matrix ($\boldsymbol{\alpha}$).

When stored in a compressed upper or lower triangular format (notice $\boldsymbol{\alpha}$ is symmetric) at double precision, the Hessian matrix for the TG-119, liver and prostate cases took an additional 4.1 GB, 1.6 GB, and 10.9 GB of memory, respectively. Furthermore, we were unable to optimize the head-and-neck cancer case that is included with the matRad toolkit due to the memory limitations of our system [6,10]. For a full 360° arc, this head-and-neck case contained 130,676 pencil beams, so the Hessian matrix would require an additional 68.3 GB of memory, which is more memory than our machine possessed. This highlights a potential limitation of current implementation of FIDAO. This may particularly be an issue when we attempt to use FIDAO for non-coplanar VMAT, which may have even more pencil beams in its plan. In a future study, we will investigate whether low-rank approximations of the Hessian matrix could be used to help reduce the memory used in FIDAO [14]. Furthermore, we will implement FIDAO within a commercial treatment and compare the FIDAO optimization to a clinically relevant DAO algorithm as opposed to the research DAO algorithm used in this and the previous study. Finally, we will parallelize FIDAO's computations on a GPU and evaluate its performance.

4.5 Conclusion

In this work, a prototype FIDAO algorithm for VMAT planning was developed and compared to a standard DAO algorithm. In the three cases that were tested, FIDAO produced plans of similar quality in at least half the time. This study demonstrates promising speed enhancement for the DAO of VMAT plans using FIDAO. Further opportunities for speed gain are possible with parallel processing technology.

4.6 References

1. MacFarlane M, Hoover D, Wong E, Goldman P, Battista J, and Chen J. A fast inverse direct aperture optimization algorithm for intensity-modulated radiation therapy. *Med. Phys.* 2019; **46**(3): 1127-39.

2. Goldman SP, Chen JZ and Battista JJ. Feasibility of a fast inverse dose optimization algorithm for IMRT via matrix inversion without negative beamlet intensities. *Med. Phys.* 2005; **32** (9): 3007-16.

3.   Goldman SP, Turnbull D, Johnson C, Chen JZ, and Battista JJ. Real-time fast inverse dose optimization for image guided adaptive radiation therapy– Enhancements to fast inverse dose optimization (FIDO). *J Appl. Phys.* 2009; **105**: 102008.

4.   Men C, Jia X, and Jiang SB. GPU-based ultra-fast direct aperture optimization for online adaptive radiation therapy. *Phys. Med. Biol.* 2010; **55** (15): 4309-19.

5.   Romeijn HE, Ahuja RK, Dempsey JF, and Kumar A. A column generation approach to radiation therapy treatment planning using aperture modulation. *SIAM J. Optim.* 2005; **15** (3): 838-62.

6.   Wieser HP, Cisternas E, Wahl N, Ulrich S, Stadler A, Mescher H, et al. Development of the open-source dose calculation and optimization toolkit matRad. *Med. Phys.* 2017; **44** (6): 2556-68.

7.   Christiansen E, Heath E, and Xu T. Continuous aperture dose calculation and optimization for volumetric modulated arc therapy. *Phys. Med. Biol.* 2018; **63** (21): 21NT01.

8.   Bzdusek K, Friberger H, Eriksson K, Hårdemark B, Robinson D, and Kaus M. Development and evaluation of an efficient approach to volumetric arc therapy planning. *Med. Phys.* 2009; **36** (6): 2328-39.

9.   Siochi RA. Minimizing static intensity modulation delivery time using an intensity solid paradigm. *Int J Radiat Oncol Biol Phys* 1999; **43** (3): 671-80.

10.   Craft D, Bangert M, Long T, Papp D, and Unkelbach J. Shared data for intensity modulated radiation therapy (IMRT) optimization research: the CORT dataset. *GigaScience* 2014; **3**:37.

11.   Bortfeld T, Schlegel W, and Rhein B. Decomposition of pencil beam kernels for fast dose calculations in three-dimensional treatment planning. *Med. Phys.* 1993; **20** (2): 311-18.

12.   Wächter A, Biegler LT. On the implementation of an interior-point filter line-search algorithm or large-scale nonlinear programming. Math Program. 2006; **106** (1): 25– 57.

13.   Men C, Romeijn HE, Jia X, and Jiang SB. Ultrafast treatment plan optimization for volumetric modulated arc therapy (VMAT). *Med. Phys.* 2010; **37**(11): 5787-91.

14. Demmel JW. *Applied numerical linear algebra.* 1st ed. Philadelphia, PA. Society for Industrial and Applied Mathematics; 1997.

Chapter 5 – Patient-specific calibration of cone-beam computed tomography images for dose tracking and treatment plan assessment

This chapter was adapted from the published article entitled "Patient-specific calibration of cone-beam computed tomography data sets for radiotherapy dose calculations and treatment plan assessment" by Michael MacFarlane, Daniel Wong, Douglas A. Hoover, Eugene Wong, Carol Johnson, Jerry J. Battista, and Jeff Z. Chen, *Journal of Applied Clinical Medical Physics*, **19** (2): 249-257 (2018). Permission to reproduce this article was granted by John Wiley and Sons and is provided in Appendix B.4. Supplemental data for this chapter is provided in Appendix E.

5.1   Introduction

Radiation treatments generally span several weeks and during this time, changes in patient weight, tumour volume and organ positioning can occur [1]. These changes may substantially alter the radiation dose distribution within the patient, potentially resulting in degraded plan quality and suboptimal clinical outcomes [2].

To ensure that a patient receives adequate treatment, a new re-planning CT (reCT) data set may be acquired to dosimetrically assess plan quality and to evaluate whether treatment re-planning has become necessary. Unfortunately, this workflow is often inefficient as it is difficult to distinguish *a priori* which patients require a reCT from those who do not. A promising solution is to use cone-beam computed tomography (CBCT) image sets to dosimetrically assess plan quality, since these image sets are already routinely acquired prior to treatment for patient setup and monitoring. However, to perform dose calculations, accurate tissue density information must be extracted from the CBCT voxel values.

Normally, tissue density information is obtained through CT calibration curves, which are generated by scanning a plastic phantom containing various inserts of known electron density [3]. For CBCT scans, the Hounsfield Units (HU) of an image set are highly dependent on many factors, including the size and material of the phantom, the materials placed in the phantom, and the imaging protocol used [4-7]. Furthermore,

scattering conditions often differ between phantoms and patients when using a cone-beam geometry. Due to this variability, HU-to-density calibration curves obtained with phantoms for CBCT lack sufficient robustness to be applicable to all patients and across all anatomical sites [6]. Consequently, alternative methods of inferring tissue density have been suggested, such as: (1) population-based calibration curves [6,7], (2) multi-level thresholding or bulk assignment of the HU or density values [7-10], and (3) voxel-to-voxel mapping using deformable image registration (DIR) [10-12].

Although these CBCT calibration techniques have demonstrated some promising results, each method may have limitations in certain situations. For instance, population-based calibration methods require unique calibration curves for each treatment site, and for each imaging protocol used. Bulk assignment techniques are dependent on the accuracy of automatic segmentation or thresholding of tissue regions, correct density assignments, or the time allotted to manually correct improperly delineated volumes. Similarly, DIR methods depend on the accuracy of the DIR algorithms, as regional DIR errors may significantly distort local anatomy and hence affect the density and dose evaluation within the region [13]. This may be particularly problematic in sites such as the pelvis and thorax where large deformation errors frequently occur. Moreover, regional DIR errors could also alter the delineation of critical structures, thereby further affecting organ dose assessment and dose-volume metrics.

To potentially resolve these limitations, we began development on an alternative patient-specific CBCT calibration (PSC) technique that, while using DIR algorithms, is less sensitive to DIR uncertainties. Briefly, rather than mapping CT numbers voxel-by-voxel with DIR, we generate a systematic but patient-specific calibration curve for each CBCT slice after registering CBCT to planning CT with DIR (see next section for details). This slice-specific calibration curve is then applied to the CBCT slice to convert the voxel values to their 'planning CT equivalent' values, without altering the patient geometry through regional DIR errors. Calibration curves are generated on a per-slice basis since scattering conditions may vary axially and thereby affect the relationship between CBCT and planning CT HU values.

To evaluate whether this new PSC method improves dosimetric accuracy, we performed a retrospective patient study of 15 head-and-neck clinical cases, and a phantom study. The dosimetric accuracy of this PSC method was compared to a re-planning CT (serving as the gold standard) and to other CBCT calibration methods implemented in literature (DIR mapping and bulk density assignment).

5.2   Materials and Methods

5.2.1   Patient Selection

Fifteen head-and-neck cancer patients were selected at random from our institution database, all of whom had completed their treatment course and were referred for a reCT study at some point during their treatment course. This tumour site was selected due to the high frequency of treatment re-planning. In order to minimize the dosimetric error resulting from anatomical differences, CBCTs acquired around the acquisition date of the reCT were reviewed and the CBCT with the most acceptable anatomical agreement with the reCT image set was selected. Patient and treatment related information are summarized in Supplemental Table 5.1.

5.2.2   Imaging

All CT and CBCT images were acquired as part of the patient's routine treatment course.

Original planning CT and re-planning CT images were acquired on a Philips Brilliance Big Bore 16-slice CT scanner (Philips Healthcare, Cleveland, OH). CT images were acquired with a full-fan 120 kVp beam. The scanning parameters used to acquire each planning and re-planning CT, can be found in Supplemental Table 5.2 and Supplemental Table 5.3, respectively. The CT images were reconstructed using the device's default filtered back-projection algorithm, with a default slice thickness of 3 mm and slice size of 512 x 512. The voxel size varied between image sets as the CT operator would select the smallest field of view (FoV) required to cover the patient [14].

CBCT images were acquired with either a Varian Truebeam or Clinac iX On-Board Imaging (OBI) system (Varian Medical Systems, Palo Alto, CA). CBCT scans were acquired with either a standard (20 mA) or low dose (10 mA) protocol using a full-fan 100 kVp beam with a full bow-tie filter. The scanning parameters used to acquire each CBCT can be found in Supplemental Table 5.4. CBCT scans were reconstructed by the treatment unit's OBI software (v 2.0-2.1) which uses a Feldkamp-Davis-Kress (FDK) reconstruction algorithm with a Ram-Lak filter [15,16]. Image slices were 384 x 384 in size when acquired with the Clinac iX's system, and 512 x 512 when acquired with the Truebeam's system.

5.2.3   Creation of calibrated CBCT image sets

Figure 5.1 outlines the general steps performed for each calibration method in this study. Details specific to each method will be described below.
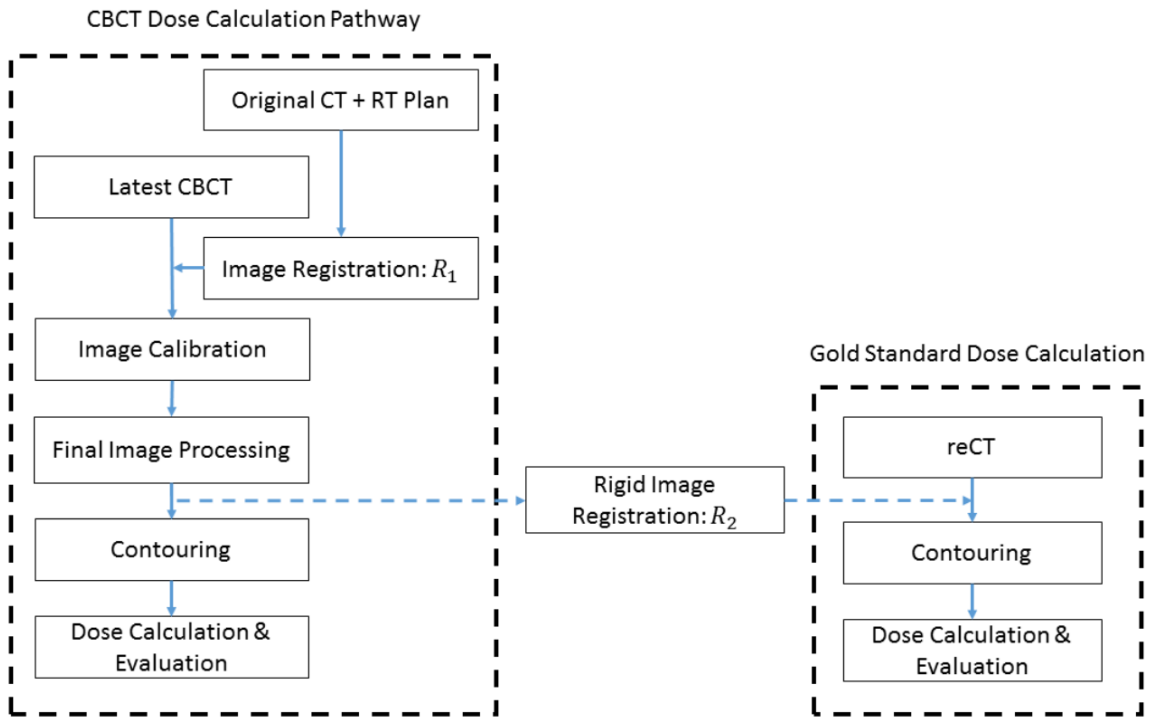
Figure 5.1: Schematic of the process used to generate a calibrated CBCT data set for dose calculation (left). The gold standard reCT data set is rigidly registered with the final calibrated CBCT data set for comparison (right).

5.2.4   Patient-specific calibration (PSC) Method

The CBCT image sets were imported into a research version of the Pinnacle treatment planning system (v9.7, Philips Healthcare, Fitchburg, WI) along with the patient's original treatment planning CT data set (containing the CT scan, treatment plan, contours, and points of interest). The CBCT image set was first rigidly registered with the planning CT image set. The planning CT image set was then deformably registered to the CBCT image set using a fast-symmetric Demon's algorithm implemented in Pinnacle [17], resulting in a deformed planning CT image set that was registered with the CBCT image set. The resulting deformed planning CT and the CBCT image sets were exported to Matlab (v2015a, MathWorks Inc, Natick, MA) for the patient specific calibration.

A correlation plot of the voxel values was then generated for each slice between the deformed planning CT and CBCT image sets (Figure 5.2a). While deformation errors may have affected the correlation of HU values for some voxel pairs (such as those highlight by the arrows in Figure 5.2a), most voxels within the slice will have been properly mapped by the DIR algorithm to planning CT HU values. Therefore, a strong relationship between the planning CT and CBCT HU values could be regressed from these correlation plots. With this relationship, we could scale the CBCT HU values to their CT-equivalent values without introducing the regional DIR errors.

Linear calibration curve specific to each slice were obtained by least-squares fitting of the correlation plots, and applied to each slice of the CBCT data set. These calibration curves were slice-specific since scatter conditions will vary between slices of the CBCT, and therefore the relationship between CBCT and planning CT HU values (the model parameters regressed) may change.

As a final image processing step, the calibrated CBCT images were merged with the original planning CT images to extend the FoV, as shown in Figure 5.2b. Before merging, the calibrated CBCT images were rigidly registered with the original planning CT (using R_1 in Figure 5.1) and resampled with a linear interpolation algorithm so that the resolution of the CBCT matched that of the planning CT. Regions that were outside of the calibrated CBCT FoV or truncated during reconstruction were substituted with

voxel values from the original planning CT images. Slices on the superior/inferior border with poor correlation between the voxel values of the CBCT and the deformed planning CT image set ($R^2 < 0.8$) were also replaced by the planning CT images. This usually occurred in the shoulder region where the CBCT FoV was insufficient to cover the whole patient, resulting in large deformation errors. By removing these slices, we could improve the anatomical matching at the junction of the CBCT and the original planning CT image set.
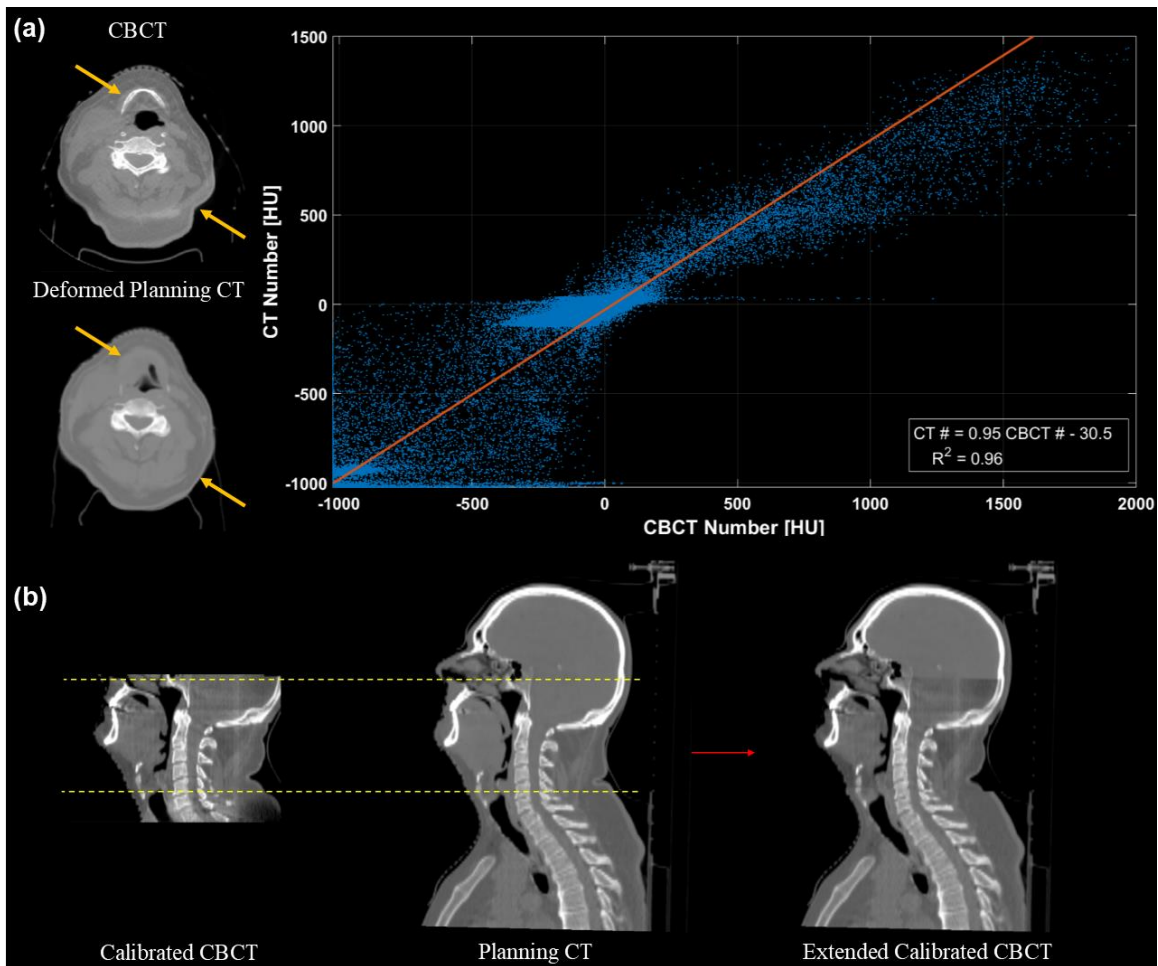
Figure 5.2: Illustration of the patient-specific calibration (PSC) method. a) An HU correlation plot is generated for each slice, between corresponding voxels of the CBCT and the deformed planning CT. Despite the presence of DIR errors (highlighted by the arrows), a strong slice-specific linear calibration curve of the CBCT HU values to the planning CT HU values, can be obtained by least square fitting. b) Once the linear mappings are applied, the calibrated CBCT image set is then rigidly registered, resampled

and merged with the original planning CT image set to extend its field-of-view. Slices with poor correlation between the CBCT and the deformed planning CT voxel values ($R^2 < 0.8$; outside of dashed lines) were replaced by the original planning CT.

5.2.5   Voxel-to-voxel DIR method

For the DIR method, the deformable image registration proceeded exactly as it did for the PSC method. Provided there are no significant DIR errors, a deformed planning CT will match the target CBCT while containing HU values from the source planning CT. Therefore, the deformed planning CT data set can be directly used to calculate the dose received at the time of treatment. After DIR, the deformed planning CT image set has the same dimensions and coordinates as the CBCT image set. Therefore, the deformed images were also rigidly registered, resampled, and merged with the original (un-deformed) planning CT images to extend the field-of-view. Like the PSC method, the same slices on the superior/inferior border with poor correlation between the voxel values of the CBCT and the deformed planning CT ($R^2 < 0.8$) were replaced by the planning CT slices.

5.2.6   Density-override method

In the density-override method, the CBCT image set was first rigidly registered with the original planning CT image set. Regions where soft tissue had become air (e.g. weight loss) or where air had been replaced by soft tissue (e.g. closed air cavity) were manually delineated on the original planning CT image set and assigned either water or air equivalent densities, accordingly. With these modifications, the major anatomical changes can be accounted for on the planning CT dataset, while continuing to use the original planning CT's HU values for dose calculations. This technique is similar to the algorithm implemented by van Zijtveld et al. [8] and is illustrated in Figure 5.3.

5.2.7   Gold standard (reCT) for dose evaluation

The CBCT image sets calibrated by each method were imported back into the research version of Pinnacle, along with the patient's re-planning CT data set (including contours). The calibrated CBCTs inherit the coordinate system of the original planning

CT study, which may not be registered with the re-planning CT. Therefore, for accurate plan dose comparison, each of the image sets was rigidly registered with the reCT image set (R_2 in Figure 5.1), taking care to match the original plan isocenter to the same anatomical location. The original treatment plan was then transferred to the reCT data set and dose was recomputed while maintaining the original beam layout and monitor units per beam. Dose was calculated on each data set using Pinnacle's Adaptive Collapsed Cone Convolution algorithm with inhomogeneity corrections [18]. The dose grid was set to cover the entire patient CT images with 3 mm resolution in all directions. To minimize dosimetric errors, regions with metal streaking artifacts were delineated on each image set and assigned tissue equivalent densities for dose computation. Dose-volume metrics evaluating tumour volume coverage and organ-at-risk (OAR) exposure were tabulated and served as the gold standard results.
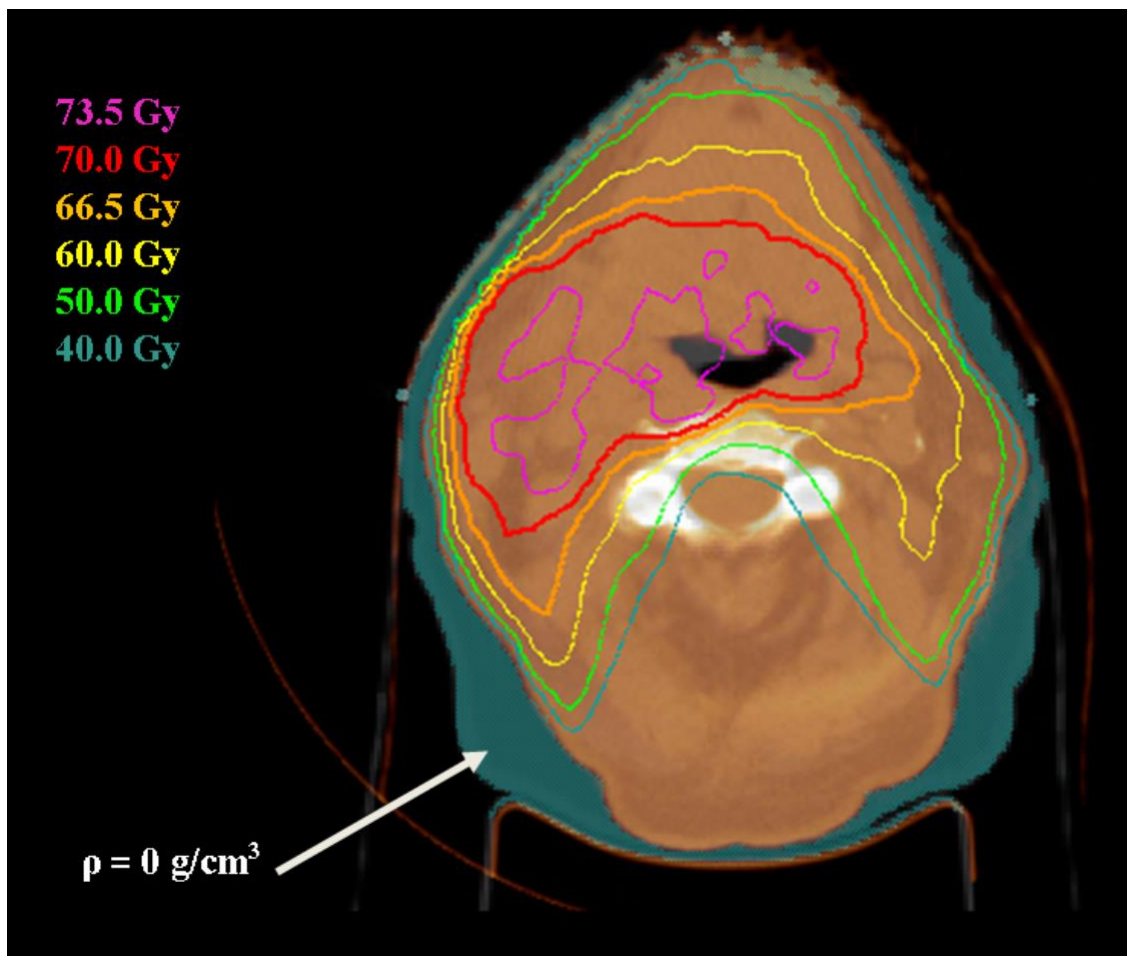
Figure 5.3: Illustration of the density-override method. Regions of weight loss (shown in a teal colourwash) were assigned a density of 0 g/cm3 for dose calculations.

5.2.8   Contouring and dose metrics

The contours from the reCT data set were rigidly copied onto each calibrated CBCT image set based on the rigid registration R_2. If necessary, these contours were manually adjusted to match the patient anatomy as seen on the calibrated image set. Dose metrics evaluating tumour volume coverage and organ-at-risk (OAR) exposure were again tabulated and compared to the gold standard results.

5.2.9   Gamma analysis

Dose distributions computed on each of the calibrated image sets were compared to the gold standard dose distribution using the SlicerRT extension (v 0.18.0) of 3D Slicer (v 4.6.2) [19,20]. A 3D gamma analysis was restricted to a region inside the original CBCT volume and excluded voxels within 3 mm of the surface so that uncertainties in surface dose were omitted. The analysis was performed with a low-dose threshold of 10% (relative to the maximum point dose on the reCT data set), and acceptance criteria of 3% dose-difference and 3 mm distance-to-agreement. The gamma pass rate (percentage of voxels with $\gamma < 1$) was tabulated.

5.2.10   Statistical Analysis

A one-way repeated measures MANOVA was performed in the Statistical Package for the Social Sciences (SPSS v23, IBM Corp, Chicago, IL) to assess whether the image set used for dose calculations influenced the collective dose metric values. Univariate analysis followed when the MANOVA test was significant, along with post-hoc pair-wise Student's t-tests when appropriate. A one-way repeated measure ANOVA was also performed to find statistical differences between the gamma pass rates. A 5% threshold for statistical significance ($p = 0.05$) was used.

5.2.11   Phantom Study

A phantom study was also performed to assess the accuracy of the DIR and PSC CBCT calibration methods. A planning CT and CBCT (Clinac iX) scan were acquired of the CIRS 062 inner 'head' phantom with various material inserts (Computerized Imaging Reference Systems Inc, Norfolk, VA).

To simulate weight loss with the phantom, a simulated reCT image set was created by reducing the planning CT's in-plane dimensions by 5% (yielding an equivalent depth reduction of 4.5 mm) as shown in Figure 5.4. Similarly, the in-plane dimensions of the CBCT images were reduced by 5% to match the simulated reCT.

The original planning CT, simulated reCT and CBCT image sets were imported into the research version of Pinnacle. The CBCT was then calibrated using both the DIR and the PSC CBCT calibration methods described above. Merging of the calibrated CBCT image sets with the original planning CT was not required as the CBCT FoV was sufficient to capture the entire phantom. The calibrated CBCT images were then rigidly registered with the reCT image set. The inserts in the phantom were manually delineated on each image set (as shown in Figure 5.4) and the average density and Sørensen-Dice similarity coefficient (compared to the reCT contour) were calculated for each insert and each image set.
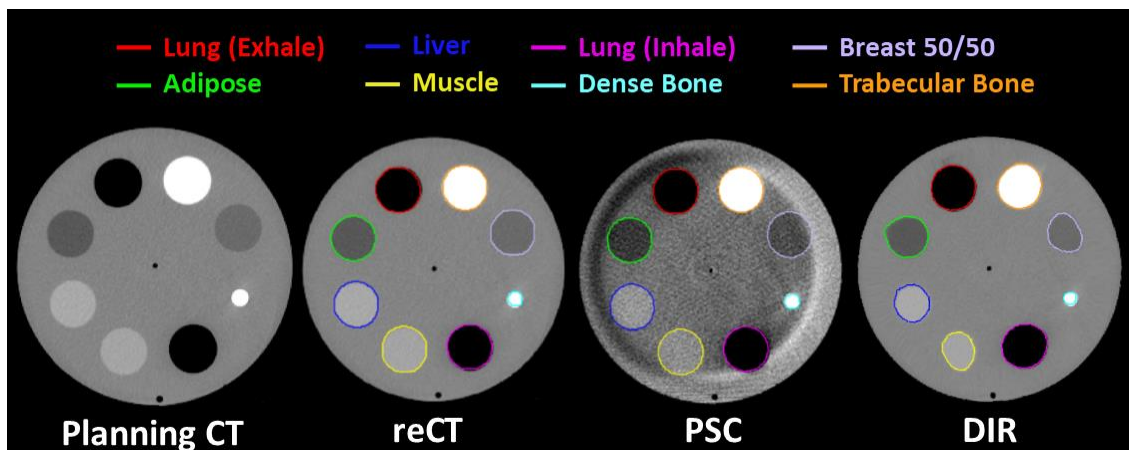
Figure 5.4: The image sets and contours produced for the phantom study. A simulated reCT was produced by reducing the Planning CT's in-plane voxel size by 5%. The CBCT

voxel size was also adjusted by 5%. The CBCT was then calibrated using both the PSC and DIR methods. The inserts were delineated on each image and the average density and Dice Coefficient (relative to the reCT) was computed for comparison.

5.3 Results

Table 5.1 shows the difference of various dose metrics compared to the gold standard values, averaged over all patients and normalized to the prescription dose (due to different prescription doses between patients). Figure 5.5 and Figure 5.6 show the average dose-volume histogram of the 15 patients and a sample patient dose distribution, respectively.

Table 5.1: Mean (standard deviation) dose metric differences compared to the gold standard reCT, normalized by the prescribed dose. Dose metrics that were significantly different to the reCT are indicated with the asterisk ($p < 0.05$) and dagger ($p < 0.01$).

ROI	Dose Metric	PSC Method [%]	DIR Method [%]	Density-Override [%]
	$D_{95\%}$	-1.1 (1.0)	-0.9 (1.0)	-0.8 (2.8)
PTV	Mean	-0.5 (0.8)	-1.0 (0.8) [†]	-1.5 (0.8) [†]
	$D_{2\%}$	0.0 (1.3)	-0.8 (1.2) [†]	-1.5 (1.3) [†]
Brainstem	$D_{0.1cc}$	0.6 (1.0)	0.0 (1.2)	-0.5 (1.5)
Cord	$D_{0.1cc}$	-2.0 (2.5) [*]	-3.0 (3.3) [†]	-3.4 (3.1) [†]
Lt. Parotid	Mean	0.7 (1.5)	0.3 (2.4)	0.5 (1.9)
Rt. Parotid	Mean	0.5 (2.2)	0.2 (3.1)	-0.4 (2.4)

Abbreviations: ROI, region of interest; PSC, patient-specific calibration; DIR, deformable image registration; D_{XX}, minimum dose to the most irradiated XX volume, specified in percent or cubic centimeters (cc), as indicated.

On average, dose metric differences were $\leq 1.1\%$ for all three methods, with the PSC method providing marginally better agreement (-0.3 $\pm$ 1.0%, mean $\pm$ standard deviation) compared to the DIR (-0.7 $\pm$1.1%) and density-override (-1.1 $\pm$ 1.2%) methods. Multivariate testing revealed that the image set used for dose calculation had a statistically significant effect on the dose metric values ($p < 0.001$). Further univariate

analysis and pair-wise t-testing found that the spinal cord maximum dose D0.1cc metric was systematically underestimated by all three methods ($p < 0.05$). Furthermore, both DIR and density-override methods also systematically underestimated both the PTV mean dose metric ($p < 0.01$) and D_{02} metric ($p < 0.01$), whereas the PSC method did not. The level of statistical significance of the Student's t-test is indicated by asterisks ($p < 0.05$) and daggers ($p < 0.01$) in Table 5.1.
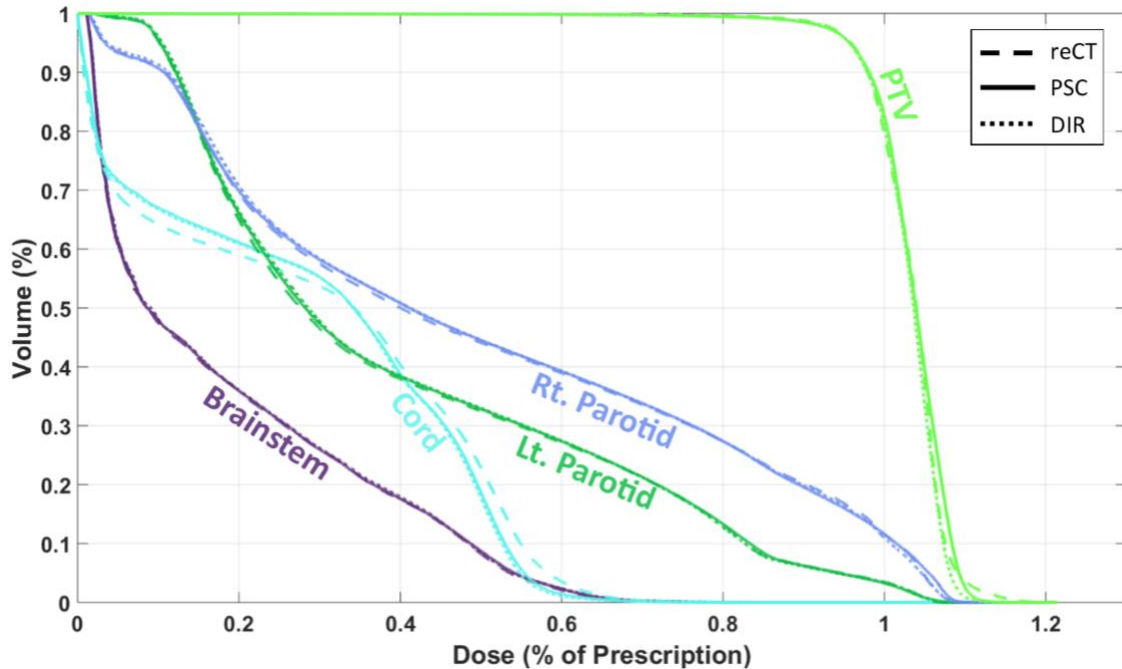
Figure 5.5: Average dose-volume histograms of fifteen plans, calculated with the gold-standard reCT image set (dashed line), and the CBCT calibrated with the patient-specific calibrated method (PSC, solid line), and the DIR method (DIR, dotted line).

The results of the 3D gamma analysis were found to be similar across all three techniques ($p = 0.41$), with the average (standard deviation) gamma pass rates of 95.0% (3.0%), 96.1% (3.3%), and 94.4% (4.4%) for the PSC, DIR, and density-override methods, respectively.

Results from the CIRS phantom study are provided in Table 5.2. Relative to the reCT scan, the DIR calibrated CBCT provided very similar densities for every insert in the phantom. However, significant distortions were introduced into the image set as a result of the DIR errors, as evident by the Dice coefficient values and by visual inspection of

the deformed CT in Figure 5.4. Conversely, the PSC calibrated CBCT provides better anatomy matching than DIR, with higher Dice coefficients. Despite the presence of crescent artifacts, the PSC method also improves the average density accuracy for most materials, relative to the uncalibrated CBCT, as shown in Table 5.2.
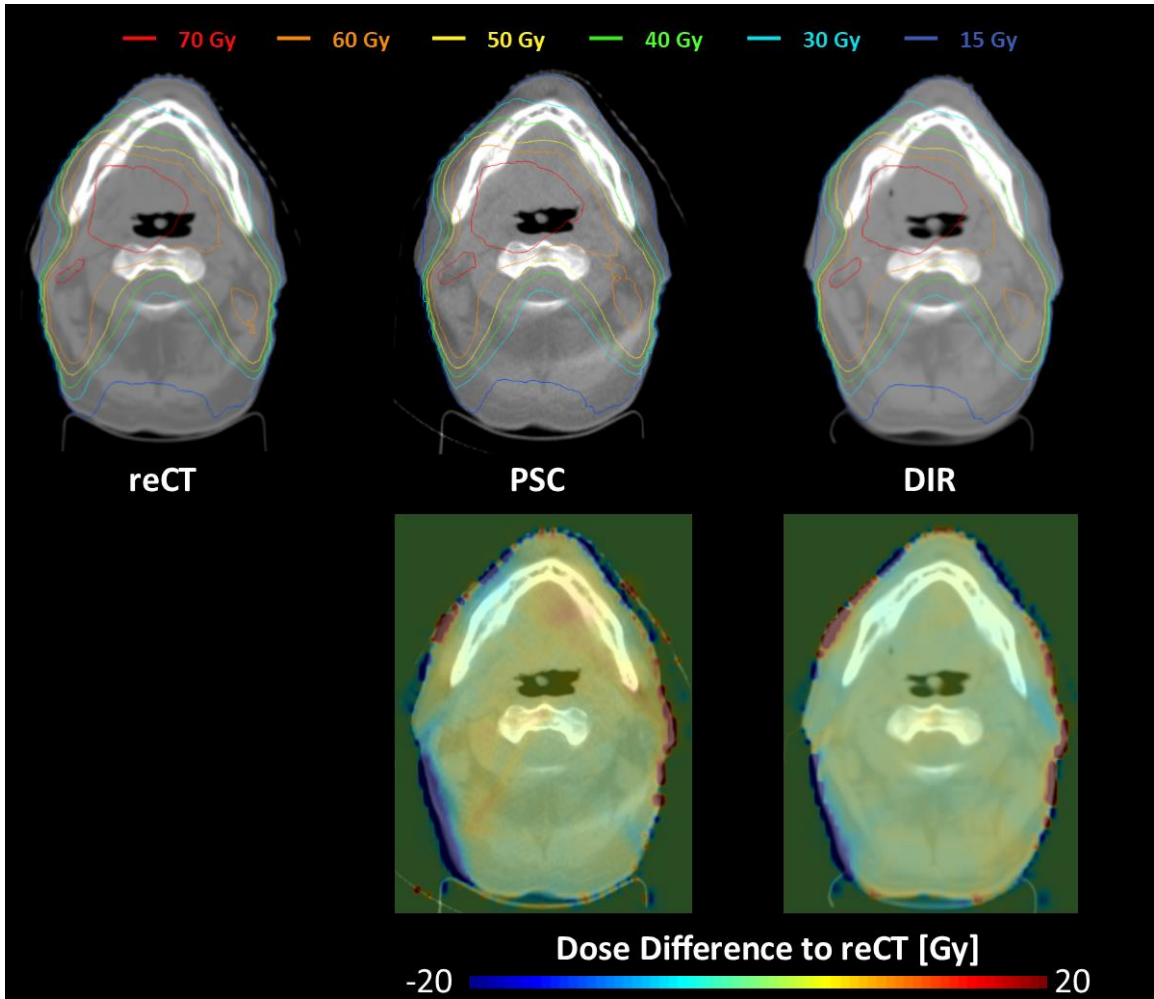
Figure 5.6: (Upper) Sample dose distributions from patient 1 for the plans calculated on the gold standard reCT (left), PSC calibrated CBCT (middle), and DIR calibrated CBCT (right) image sets. (Lower) Differences between the PSC, DIR calculated dose distribution and the reCT calculated dose distribution.

On average, it took about 30 minutes to perform the full DIR and PSC calibration workflow, with the bulk of the time spent on dose calculations and transferring the image sets between systems for merging and/or calibration. Of those 30 minutes, under a minute

was spent running the DIR, and only a few seconds were spent calibrating and merging the CBCT with planning CT image set using the PSC method. The density-override techniques took longer (~50 minutes) because the contours delineating anatomical changes were generated manually.

Table 5.2: The average density and Sørensen-Dice similarity coefficient (compared to the reCT) calculated for each insert in the CIRS 062 phantom, and for each image set.

Material (True density [g/cm^3])	Computed Density [g/cm^3]			Dice Coefficient	
	DIR	PSC	CBCT	PSC	DIR
Exhaled Lung (0.52)	0.53	0.52	0.47	0.98	0.96
Adipose (0.93)	0.93	0.90	0.87	0.99	0.94
Liver (1.05)	1.05	1.04	1.02	0.96	0.77
Muscle (1.05)	1.05	1.04	1.00	0.97	0.73
Inhaled Lung (0.24)	0.26	0.27	0.21	0.97	0.97
Dense Bone (1.55)	1.55	1.58	1.57	0.86	0.80
Breast 50/50 (0.96)	0.96	0.95	0.91	0.96	0.79
Trabecular Bone (1.20)	1.19	1.21	1.20	0.94	0.92

5.4   Discussion

We have developed a patient-specific method of calibrating CBCTs for dose tracking and plan assessment and compared it with other methods for the head-and-neck site [8,11]. The results show that slightly better dosimetric agreement with the gold standard reCT can be obtained when using this patient-specific calibration (PSC) method, although each method demonstrated sufficient accuracy for plan re-assessment during radiotherapy.

It is worth noting that the spinal cord dose was poorly estimated by all three methods ($D_{0.1cc}$ in Table 5.1, Figure 5.5). This was caused by a few select patients who had slight variations of the spinal cord positioning in regions of steep dose gradients (due to differences in setup between the reCT and the CBCT studies). It should also be noted that the gamma pass rates presented in this study are lower than other published results. For example, both van Zijtveld et al. [8] and Veiga et al. [11] reported similar gamma pass rates for the head-and-neck site when using a stricter 2%, 2 mm acceptance criteria. The difference in gamma pass rates could be attributed to differences in the study design. For

instance, Veiga et al. [11] performed their DIR method on simulated CBCTs, which were created by deforming the selected CBCT to match the reCT.

The results from this study illustrate the pros and cons of the three CBCT calibration methods. While the density override method is easy to implement on available treatment planning systems, it cannot account for internal anatomical changes and it can be very time consuming to perform. Furthermore, the observed dosimetric accuracy of this technique is not as high as the other CBCT calibration techniques (Table 5.1). The DIR method is less sensitive to the CBCT artifacts (such as the crescent artifact visible in Figure 5.4) and provides sufficiently accurate tissue density and dosimetric information (Table 5.2, Figure 5.5). However, DIR methods may introduce distortions into the image through DIR errors (Figure 5.2a, Figure 5.4, Table 5.2) that can affect OAR delineations and their dosimetric evaluations (Table 5.1). On the other hand, the PSC method is less sensitive to regional DIR errors as it maintains the patient anatomy from the CBCT, resulting in higher Dice similarity coefficients as shown in Table 5.2. While the PSC method preserves the patient anatomy, it also preserves the noise and any artifacts present in the CBCT images (Figure 5.4). It also produces slightly less accurate densities than the DIR methods (Table 5.2). Neither of these limitations appeared to have considerable influence on the dosimetric performance of the PSC method (Table 5.1, Figure 5.5).

While distortions introduced by DIR calibration did not have substantial influence on the dosimetric accuracy in the head-and-neck site studied here (Table 5.1, Figure 5.5 & Figure 5.6), the same may not be true in sites such as pelvis or thorax where large DIR distortions are commonplace at tissue-air interfaces, such as the bowel. Therefore, the PSC method could be potentially advantageous for these sites and will be investigated in the future.

Based on Table 5.2, the PSC method improves the average density accuracy of the uncalibrated CBCT, for most materials inserted in the phantom. However, since there were relatively low amounts of high-density (bone) material in each slice, the calibration curves used by the PSC method were primarily fitted for lower density materials and not higher density materials. As a result, the density of higher density materials were not

corrected by the PSC method. A future version of this PSC method could potentially be improved by using a piece-wise continuous linear calibration curves that calibrates both lower and higher density materials separately. Furthermore, the limited FoV, noise, and artifacts present in CBCTs may pose additional challenges in sites such as the pelvis or thorax [21,22]. Therefore, more sophisticated methods of extending the CBCT field-of-view (such as fusion-aligned reprojection techniques [23]), and reducing the noise and artifacts present in the CBCT, will be investigated in the future. The performance of this method will also need to be verified on other CBCT imaging systems, and in other treatment sites.

Finally, in addition to calibrating CBCT for dose calculations, the calibration curves used in the PSC method can also be used to quickly identify regions of potential DIR error on a deformed CT. For example, if one highlights the voxels outside of the 95% confidence interval of the calibration curve, regions where the CBCT and the deformed CT differed substantially can be easily visualized. An example of this application is provided in Figure 5.7.

5.5   Conclusion

A patient-specific CBCT calibration method has been developed and tested for the head-and-neck site. Compared to a gold standard reCT dose distribution, average differences in dose metric values were $\leq 1.1\%$ for all calibration methods tested, although the PSC method showed slightly better performance. Some advantages of the PSC method are that it preserves the patient anatomy, accounts for variable scattering per CT slice, can be uniquely applied to each patient, is computationally efficient, and may also be used to display errors introduced by DIR algorithms.
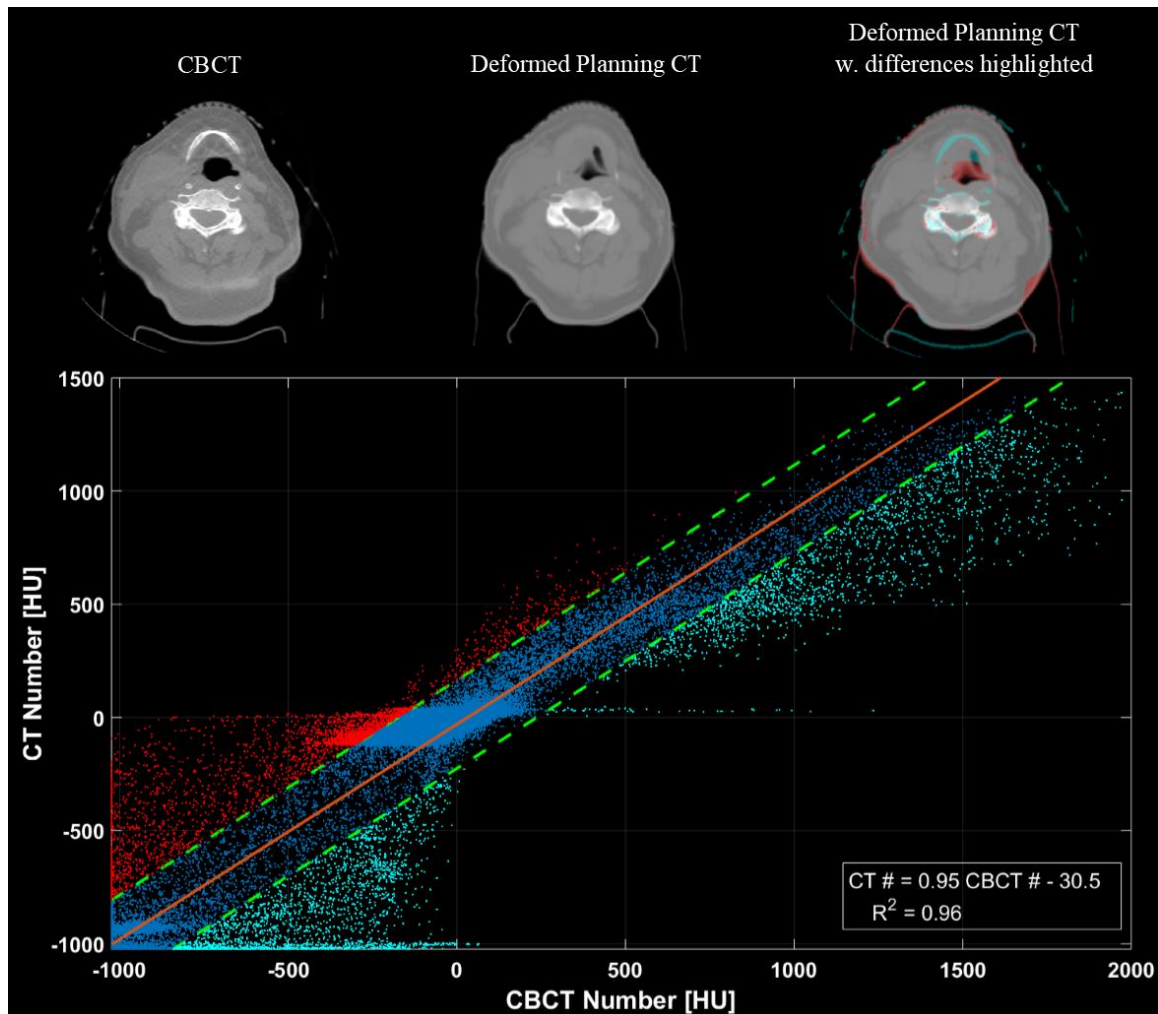
Figure 5.7: Illustration of how the linear calibration tool may be used to highlight regions of deformation error. The bottom frame shows the correlation plot generated for this slice. The linear mapping used to calibrate the slice is shown in orange, while the upper and lower bounds of the 95% confidence interval (CI) are shown as the dashed green lines. Data-points falling outside of the 95% CI are labelled in red and blue on the plot and are also highlighted on the top-right deformed planning CT to show regions where the CBCT (top-left) and deformed planning CT (top-middle) differ due to DIR errors.

5.6 Reference

1. Barker JL Jr, Garden AS, Ang KK, et al. Quantification of volumetric and geometric changes occurring during fractionated radiotherapy for head-and-neck

cancer using an integrated CT/linear accelerator system. *Int J Radiat Oncol Biol Phys* 2004; 59(4):960-70.

2. Hansen EK, Bucci MK, Quivey JM, Weinberg V, and Xia P. Repeat CT imaging and replanning during the course of IMRT for head-and-neck cancer. *Int J Radiat Oncol Biol Phys* 2006; 64(2):355-62.

3. Saw CB, Loper A, Komanduri K, Combine T, Huq S, and Scicutella C. Determination of CT-to-density conversion relationship for image-based treatment planning systems. *Med Dosim* 2005; 30(3):145-8.

4. Yoo S, and Yin FF. Dosimetric feasibility of cone-beam CT-based treatment planning compared to CT-based treatment planning. *Int J Radiat Oncol Biol Phys* 2006; 66(5):1553-61.

5. Hatton J, McCurdy B, and Greer PB. Cone beam computerized tomography: the effect of calibration of the Hounsfield unit number to electron density on dose calculation accuracy for adaptive radiation therapy. *Phys Med Biol* 2009; 54(15):N329-46.

6. Richter A, Hu Q, Steglich D, et al. Investigation of the usability of conebeam CT data sets for dose calculation. *Rad Oncol* 2008; 3:42.

7. Fotina I, Hopfgartner J, Stock M, Steininger T, Lütgendorf-Caucig C, and Georg D. Feasibility of CBCT-based dose calculation: Comparative analysis of HU adjustment techniques. *Radiother Oncol* 2012; 104(2):249-56.

8. van Zijtveld M, Dirkx M, and Heijmen B. Correction of conebeam CT values using a planning CT for derivation of the ''dose of the day''. *Radiother Oncol* 2007; 85(2):195-200.

9. Chen S, Le Q, Mutaf Y, et al. Feasibility of CBCT-based dose with a patient-specific stepwise HU-to-density curve to determine time of replanning. *J Appl Clin Med Phys 2017; 18(5): 64-69.*

10. Onozato Y, Kadoya N, Fujita Y, et al. Evaluation of On-Board kV Cone Beam Computed Tomography – Based Dose Calculation With Deformable Image Registration Using Hounsfield Unit Modifications. *Int J Radiat Oncol Biol Phys* 2014; 89(2):417-23.

11. Veiga C, McClelland J, Moinuddin S, et al. Toward adaptive radiotherapy for head and neck patients: Feasibility study on using CT-to-CBCT deformable registration for "dose of the day" calculations. *Med Phys* 2014; 41(3): 031703.

12. Moteabbed M, Sharp GC, Wang Y, Trofimov A, Efstathiou JA, and Lu HM. Validation of a deformable image registration technique for cone beam CT-based dose verification. *Med Phys* 2014; 42(1): 196-205.

13. Vickress J, Battista J, Barnett R, and Yartsev S. Representing the dosimetric impact of deformable image registration errors. *Phys Med Biol* 2017; 62: N391-403

14. Philips CT Clinical Science. Respiratory motion management for CT. *Philips White Paper* 2013, Nr. 4522 962 91291.

15. Han X, Pearson E, Pelizzari C, et al. Algorithm-enabled exploration of image-quality potential of cone-beam CT in image-guided radiation therapy. *Phys. Med. Biol.* 2015; 60(12):4601-33.

16. Ramachandran G, and Lakshminarayanan A. Three-dimensional reconstruction from radiographs and electron micrographs: application of convolutions instead of Fourier transforms. *Proc. Natl. Acad. Sci. USA.* 1971; 68(9): 2236-40.

17. Dru F, and Vercauteren T. An ITK implementation of the symmetric log-domain diffeomorphic demons algorithm. *Insight Journal* 2009.

18. McNutt T. Dose calculations – collapsed cone convolution and delta pixel beam. *Pinnacle White Paper* 2007, Nr. 4535 983 02474/870.

19. Low DA, Harms WB, Mutic S, and Purdy JA. A technique for the quantitative evaluation of dose distributions. *Med Phys* 1998; 25(5): 656-61.

20. Pinter C, Lasso A, Wang A, Jaffray D, and Fichtinger G. SlicerRT: Radiation therapy research toolkit for 3D Slicer. *Med Phys* 2012; 39(10): 6332-8.

21. Niu T, Sun M, Star-Lack J, Gao H, Fan Q, and Lei Z. Shading correction for on-board cone-beam CT in radiation therapy using planning MDCT images. *Med Phys* 2010; 37(10): 5395-406.

22. Marchant TE, Moore CJ, Rowbottom CG, MacKay RI, and Williams PC. Shading correction algorithm for improvement of cone-beam CT images in radiotherapy. *Phys Med Biol* 2008; 53(20): 5719-33.

23. Ruchala KJ, Olivera GH, Kapatoes JM, Reckwerdt PJ, Mackie TR. Methods for improving limited field-of-view radiotherapy reconstructions using imperfect a priori images. *Med Phys* 2002; 29(11): 2590-605.

Chapter 6 – Summary & Future Work

6.1 Contributions and Findings

This thesis presented a number of improvements to the EBRT planning process that enhance patient plan quality as well as the efficiency of the treatment planning and beam delivery procedures. This work also made progress towards long-awaited applications like on-line plan assessment and adaptive radiation therapy.

In Appendix A, we presented initial work on a new treatment planning algorithm called unified intensity-modulated arc therapy (UIMAT) which combines the optimization and delivery of rotational VMAT and fixed-gantry IMRT. Specifically, UIMAT automatically selects which subset of gantry angles to deliver as fixed-gantry IMRT, and which arc ranges to deliver as rotational VMAT. It then simultaneously optimizes the VMAT and IMRT beams and merges their control point (CP) information for efficient delivery – merging the best qualities of these complementary techniques.

A retrospective planning study of 15 lung, head-and-neck, and prostate cancer patients was performed, comparing the clinically approved treatment plans with the plans obtained with this UIMAT algorithm. The results of this planning study showed that UIMAT could obtain similar PTV coverage while also providing modest dose reductions to the surrounding OARs in the lung and prostate cases (as demonstrated by Figure A.4 & Figure A.5, respectively), and substantial dose reductions to OARs in head-and-neck cases (as demonstrated in Figure A.3). These findings motivated a larger retrospective planning study of 30 head-and-neck patients that was presented in Chapter 2. When compared to the clinically approved dual-arc VMAT or step-and-shoot IMRT plan, the UIMAT plans provided similar or better PTV coverage while also reducing the dose to nearly all OARs (Figure 2.2, Table 2.1). This OAR dose reduction was achieved without increasing the dose to unspecified normal tissue (i.e. by relocating the dose elsewhere). It was also found that UIMAT plans could be delivered more efficiently than clinical IMRT or VMAT plans, both in terms of average delivery time and total delivered MU.

This reduction in OAR dose means that UIMAT could potentially reduce the severity or frequency of treatment-related toxicities such as dry mouth (xerostomia), mouth sores, and difficulty swallowing (dysphagia) in head-and-neck cancer patients [1]. Conversely, the lower OAR doses could allow for dose escalation to the PTV to achieve even better tumour control while continuing to adhere to OAR dose limits.

DAO algorithms are needed to create VMAT, IMRT, and UIMAT treatment plans. Due to the dimensionality and computational complexity of the DAO problem, and the current inefficient trial-and-error approach to plan optimization, treatment planning can sometimes take several hours or even days to complete in complex cases. Furthermore, when there is limited time for treatment planning (e.g. for re-planning), sub-optimal treatment plans may be accepted so as to not interrupt or delay treatment delivery. In Chapter 3 and Chapter 4, we developed and evaluated a new fast DAO algorithm called fast inverse direct aperture optimization (FIDAO). FIDAO extends a previously established FMO algorithm called fast-inverse dose optimization (or FIDO) for fast DAO. When compared to conventional DAO algorithm, FIDAO reduced DAO times by as much as 23 times in IMRT plans (Chapter 3) and by as much as 18 times in VMAT plans (Chapter 4). Similar plan quality was observed between the plans obtained with the standard DAO algorithm and FIDAO, though some minor (but clinically insignificant) differences could be observed between the VMAT plans. Given that UIMAT plans consist of just as many pencil beams as a VMAT plan, we anticipate that faster DAO will also be observed with a FIDAO algorithm implemented for UIMAT planning.

FIDAO, like conventional DAO algorithms, is well suited for parallelization on GPUs. When compared to their runtimes on CPUs, standard DAO algorithms implemented on GPUs have achieved an average speed gain of about 37 times in IMRT and 15 times in VMAT [2,3]. If similar gains were to be obtained with FIDAO, the FIDAO optimization times could be in the millisecond range for IMRT plans, and in a few seconds range for VMAT plans. This could drastically reduce the time spent on treatment planning, allowing the treatment planner to focus on the plan quality instead of the plan deadline. It could also make applications like multicriteria optimization (MCO) faster and allow for new applications such as interactive treatment planning and on-line

adaptive radiotherapy. In order to perform on-line adaptive radiotherapy, accurate dose information is needed from image sets acquired on-line, which leads us to the final project.

In Chapter 5, we developed a patient-specific CBCT calibration (PSC) technique for on-line dose calculations and plan assessment. This PSC method demonstrated high dosimetric accuracy when compared to the dose calculated with a gold-standard re-planning CT data set, and when compared to other established CBCT calibration techniques. One of the key features of this PSC method is that it does not introduce geometric distortions (via deformation errors) and it accounts for slice-by-slice scattering conditions. Furthermore, this PSC technique can be used to flag regions of DIR error on deformed image sets. The calibrated CBCT could be used instead of acquiring a new planning CT, to assess whether treatment re-planning has become necessary due to anatomical changes such as weight-loss or tumour regression. This will help make sure that the patient receives their intended treatment and minimize the risk of a suboptimal clinical outcome. Moreover, this will help avoid unnecessary re-planning procedures that potentially waste resources and cause treatment delays. Finally, if combined with FIDAO and automated precise target/OAR delineation techniques, treatment re-planning could potentially take place on-line while the patient is immobilized and awaiting their treatment.

In summary, this thesis has developed new methods of improving plan quality and delivery efficiency, improving planning efficiency, and assuring accurate EBRT treatment delivery in the presence of ongoing anatomical changes. It also brings applications like on-line adaptive radiotherapy within the realm of feasibility.

6.2 Limitations and Future Work

The future projects of FIDAO, UIMAT, and PSC are shown as a diagram in Figure 6.1. The section number describing each future project is stated along each arrow.
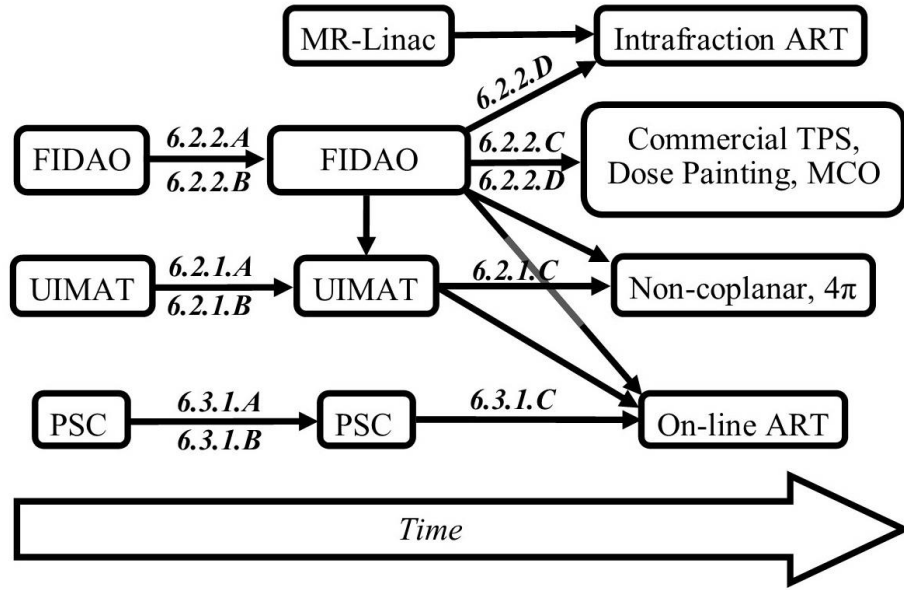
Figure 6.1: Visual diagram of proposed future work. The section number describing each future project is stated along each arrow.

6.2.1   UIMAT

A.   Robustness

The UIMAT algorithm presented in Section A.2.1 is only capable of producing hybrid VMAT-IMRT treatment plans, as well as single-arc VMAT treatment plans (when 2 apertures are sequenced for every beam). However, a truly unified approach to VMAT and IMRT planning should be able to produce VMAT-only, IMRT-only, or hybrid treatment plans, should they be the optimal treatment method for the patient. Development is currently underway on a new, more robust UIMAT algorithm. Briefly, this new algorithm is inspired by recent work on beam orientation optimization using sparse optimization techniques [4,5]. Specifically, this UIMAT algorithm begins by performing FMO and aperture sequencing at 4° gantry angle increments. The goal of this step is to create a large collection of CPs at many gantry angles, as illustrated in Figure 6.2a. Next an accelerated proximal gradient method optimizes the CP shapes and weights, while simultaneously minimizing a regularizer acting on the CP weights [6,7]. As this DAO progresses, the regularizer forces the DAO algorithm to eliminate CPs from the treatment plan, while simultaneously trying to improve the plan quality. The idea is that gantry angles that can use higher intensity-modulation to improve plan quality, will

retain their apertures, while all other gantry angles will have their CPs removed. This step is illustrated in Figure 6.2b. In cases where IMRT-only is the optimal treatment plan, we expect this DAO to only keep CPs at select gantry angles. Conversely, in cases where VMAT-only is the optimal treatment plan, we expect this DAO to eliminate CPs uniformly from all gantry angles.

Figure 6.2: Illustration of the new UIMAT algorithm. A) FMO and aperture sequencing (each CP illustrated as a square) is performed at 4° increments. B) DAO with a CP weight regularizer is performed. As this DAO progresses, the regularizer eliminates CPs from the treatment plan. C) The results of this DAO are parsed and VMAT (green) or IMRT (purple) beams are sequenced using the CPs from B). A final DAO is then performed.

When this DAO terminates, the treatment plan may still have too many apertures for treatment delivery to be practical. Therefore, the UIMAT algorithm next evaluates each

individual CP and gantry angle's delivery efficiency and their contribution to the treatment plan. It then sequences VMAT arcs and/or IMRT beams from these CPs. This step is visualized in Figure 6.2c. The newly sequenced VMAT and IMRT beams then undergo a final DAO, without the CP weight regularizer described above, and where the VMAT- or IMRT-related delivery constraints are enforced.

This new UIMAT algorithm is currently being implemented in MATLAB v9.4 (Mathworks Inc, Natick, MA) using the open-source treatment planning toolkit matRad (v2.2 – dev_VMAT build) [8,9]. Preliminary results of this UIMAT algorithm on a prostate, head-and-neck, and a right-sided whole breast radiotherapy case are provided in Figure 6.3. The plans obtained with this new UIMAT algorithm were compared to conventional dual-arc VMAT plans in the prostate and head-and-neck cases, and a tangent-field IMRT plan in the whole breast radiation therapy case.

In the whole breast radiotherapy case, the UIMAT algorithm produced a hybrid treatment plan using a single VMAT arc and two tangent IMRT beams (similar to the plan visualized in Figure 6.2c). Slightly lower OAR doses were obtained with the UIMAT algorithm, as visible from the DVHs. In the prostate case, the UIMAT algorithm also produced a dual 360° arc VMAT plan. However, the plan quality of the UIMAT plan was noticeably better, as can be seen by the DVH curves. Finally, in the head-and-neck case, the UIMAT algorithm produced a hybrid plan consisting of a single 360° VMAT arc and 5 IMRT beams. Superior OAR sparing was observed with the UIMAT plan, supporting the observations of the previous UIMAT studies.
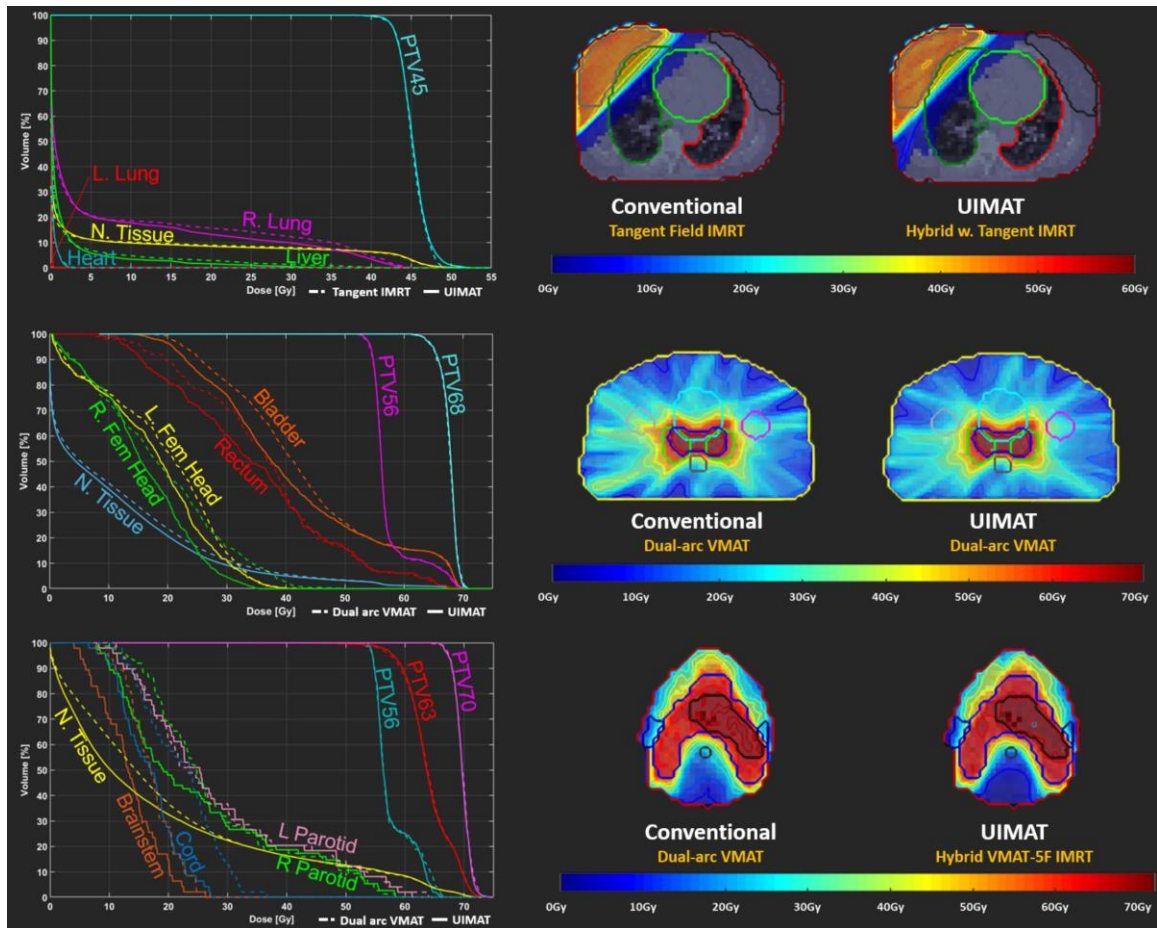
Figure 6.3: Preliminary DVH [left] and sample dose distributions [right] from the new UIMAT algorithm.

Further development is still needed for this algorithm. If the regularizer is not adequately enforced during the first DAO, the optimization will fail to eliminate enough CPs from the plan, and the subsequent beam sequencing step will create an impractical number of beams. Similarly, we have not yet settled on a single metric for determining a CP's or gantry angle's 'contribution' to the treatment plan. Currently, the algorithm looks at the median PTV voxel dose that is delivered from each gantry angle (as shown in Figure 6.2c) as a measure of each gantry angle's contribution to the plan. Better metrics (such as the gantry angle's relative contribution to the objective function value) may be suitable.

B. Constraints

As discussed in Section 2.4, the DAO algorithm currently used by UIMAT cannot enforce a minimum MU or MLC segment area during optimization. This could make UIMAT susceptible to dosimetric errors introduced by small field and small MU dosimetry and could explain why lower gamma passing rate were observed with UIMAT in the head-and-neck study [10-12]. Therefore, a future UIMAT algorithm should use a custom DAO algorithm – such as FIDAO – where these delivery constraints can be enforced.

C. Additional Applications for UIMAT

Additional future work includes integrating FIDAO into this UIMAT algorithm. This fast UIMAT algorithm could then be implemented on GPUs, and potentially used for online adaptive radiotherapy using the PSC CBCT technique or other on-line 3D image sets. Finally, one can also investigate a UIMAT algorithm that uses non-coplanar arcs or that can select IMRT beams outside of the VMAT arc range. Moreover, one can investigate a UIMAT algorithm that also incorporates couch rotations during beam delivery (a 4π UIMAT algorithm) [13].

6.2.2 FIDAO

A. Memory

FIDAO's greatest limitation at the moment is the computer storage requirements for the Hessian matrix. As discussed in Section 4.4, we were unable to optimize a head-and-neck VMAT plan as FIDAO's Hessian matrix required much more memory (68 GB) than was available on the tested computer system (64 GB). This memory issue will continue to grow as we evaluate FIDAO on larger treatment plans, including non-coplanar VMAT and 4π plans (where the couch is also allowed to rotate during beam delivery [13]). This is because the size of the Hessian matrix grows quadratically with the number of pencil beams in the plan. This storage issue can potentially be mitigated by using a low-rank approximation of the Hessian matrix, via singular value decomposition (SVD) [14]. Specifically, SVD can help identify a set of vectors whose memory requirements are much smaller, and whose product closely approximates the full Hessian matrix.

Alternatively, FIDAO could perform successive optimizations on a random sampling of the plan parameters, allowing for smaller Hessian matrices during each individual optimization cycle. With this memory issue resolved, future studies will continue to develop and evaluate FIDAO's performance on larger co-planar and non-coplanar VMAT plans, UIMAT plans, and potentially 4π plans.

B. Dosimetric Accuracy

Another source for improvement in FIDAO is in the selection of its dose calculation algorithm. SVD dose calculation algorithms are commonly used in plan optimization due to their superior speed [15]. However, SVD's superior speed comes at the cost of reduced dosimetric accuracy when compared to slower dose calculation algorithms such as collapsed cone convolution (CCC) and Monte Carlo simulation [16,17]. The time gained with FIDAO's fast optimization could be re-allocated to executing slower, but more accurate, dose computation algorithm for calculating α and $\vec{\beta}$. Alternatively, some commercial DAO algorithms first perform an accurate dose calculation (e.g. CCC) of the plan prior to DAO. They then use the more approximate SVD dose engine to 'perturb' the dose distribution based on the difference between the current plan parameters and plan parameters at the time of the accurate dose calculation [15,17]. This allows for fast DAO with only a slight loss of dosimetric accuracy. A future study could evaluate whether this 'perturbation' approach is applicable to FIDAO.

C. Commercial Software Platforms

The interior-point DAO algorithm that has been used as a benchmark for FIDAO thus far, may not be representative of the optimization times or the plan quality we would obtain with a commercial treatment planning system. Therefore, another step in FIDAO's development is to implement FIDAO within a commercial treatment planning system and to compare its performance to well established DAO algorithms like the simulated annealing DAO algorithm in Eclipse (Varian Medical Systems, Inc., Palo Alto CA) [18] or direct machine parameter optimization (DMPO) [15] in Pinnacle[3] (Philips Healthcare, Fitchburg, USA) and RayStation (RaySearch Laboratories AB, Stockholm SE).

D. *Future Applications of FIDAO*

With FIDAO implemented in a commercial treatment planning system, one intriguing study would be to compare FIDAO and the commercial DAO algorithm on stereotactic radiosurgery (SRS) and stereotactic body radiotherapy (SBRT) cases. As discussed in Section 3.4, it is recommended that the dose voxel size in SRS and SBRT plans be 2mm or less [19]. These high-resolution dose grids will result in the standard DAO algorithm running substantially slower. However, only the calculation times for α and $\vec{\beta}$ will be affected by the dose grid resolution in FIDAO. Therefore, a large difference in the optimization time could be observed in SRS and SBRT cases.

Another future study will implement FIDAO on high-performance GPUs and investigate its performance to a standard DAO method on a GPU. If ultra-fast optimization times are achieved, this GPU-based FIDAO algorithm could be used for on-line adaptive radiotherapy using the on-line PSC CBCTs or MRI data-sets. It could also be used to speed up multi-criteria optimization (MCO), or for interactive treatment planning like dose-painting. Specifically, in dose painting, the treatment planner could 'paint' a desired dose distribution on the planning CT, or they could drag a point on the DVH interactively instead of modifying IMRT objectives. The DAO algorithm would then immediately update the treatment plan and dose distribution, ideally in real-time.

Finally, with the real-time imaging capabilities of MR-linacs, it may also be possible to do *intra*fraction treatment adaptation with FIDAO. That is, during treatment delivery, the undelivered beams could be re-optimized to compensate for any anatomical changes that have occurred moments earlier during treatment delivery (e.g. changes in patient positioning, their respiratory cycle, or gas passing through the rectum) [20]. This intrafraction adaptive radiotherapy could potentially eliminate the need for certain immobilization equipment, such as the very invasive head frames used for brain SRS (i.e. frame-less SRS) [19].

6.2.3 PSC

A. Limited Field-of-View

CBCTs have a limited field-of-view relative to planning CTs and do not provide sufficient anatomical information of the patient, at the time of treatment, for on-line adaptive radiotherapy. Therefore, methods of extending CBCT's limited field-of-view, rather than relying on the fusion with the planning CT scans, will be beneficial [21].

B. Artifacts

In addition to preserving the patient's anatomical information, the PSC calibration method also preserves any noise and imaging artifacts present in the CBCT. Iterative reconstruction technique could be used instead of filtered back-projection to improve the CBCT image quality, reduce artifacts, and potentially improve the dosimetric accuracy of PSC [22]. Similarly, scatter-correction techniques – such as those using convolution neural networks – could also enhance the PSC method by improving the CBCT image quality, dosimetric accuracy, or calibration time [23-25].

C. Additional work

With these improvements, a future study could re-evaluate the dosimetric accuracy of the PSC method in the head-and-neck site, relative to the gold-standard re-planning CT and other CBCT calibration techniques. A future study could also assess the dosimetric accuracy in other anatomical sites such as the pelvis, thorax, and abdomen sites. Finally, a study could evaluate the feasibility of the PSC method for rapid on-line treatment adaptation and re-optimization using FIDAO and/or UIMAT.

6.2.4 Summary

Medical linear accelerators have evolved rapidly over the last few decades, with the integration of MLC systems, the addition of dynamic delivery capabilities (e.g. fixed-gantry IMRT and rotational-VMAT) and on-board 3D imaging systems (i.e. CT, CBCT, MRI, and soon PET). At the time of writing this thesis, EBRT has yet to utilize these linac features to their fullest potential. Therefore, this research set out to introduce a number of improvements to the EBRT process that enhance the use of modern-day linear accelerators. Specifically, we hypothesized that a fast plan optimization algorithm that

unifies rotational VMAT and fixed-gantry IMRT will improve radiotherapy plan quality, planning and delivery efficiency, and will provide a stepping-stone towards future on-line (interactive) plan adaptation.

This was demonstrated with a new UIMAT planning algorithm that combines the optimization and delivery of rotational VMAT and fixed-gantry IMRT. This UIMAT algorithm demonstrated lower normal tissue doses and improved delivery efficiency compared to conventional IMRT and VMAT treatment plans. Next, a fast-direct aperture optimization algorithm was established and applied to both IMRT and VMAT planning. This algorithm exhibited superior plan optimization speed on both IMRT and VMAT plans, and potential for implementation in UIMAT. Finally, a patient-specific CBCT calibration technique was developed and tested on head-and-neck cases. This calibration technique demonstrated high dosimetric accuracy and potential for on-line plan adaptation. Collectively, these projects improve radiotherapy plan quality, planning and delivery efficiency, as well as establish the foundation for an on-line plan adaptation procedure. Additional applications of these projects include dose-painting, multi-criteria optimization, as well as inter- and intra-fraction on-line adaptive radiotherapy in response to anatomical changes. Ultimately, these developments could enhance the quality of life and the survival rates of cancer patients, using existing technology that is widely available today.

6.3 References

1. Marks LB, Yorke ED, Jackson A, *et al.* Use of Normal Tissue Complication Probability Models in the Clinic. Int. J. Radiat. Oncol. Biol. Phys. 2010; 76:S10-9.
2. Men C, Jia X, and Jiang SB. GPU-based ultra-fast direct aperture optimization for online adaptive radiation therapy. *Phys. Med. Biol.* 2010; **55** (15): 4309-19.
3. Men C, Romeijn HE, Jia X, and Jiang SB. Ultrafast treatment plan optimization for volumetric modulated arc therapy (VMAT). *Med. Phys.* 2010; **37**(11): 5787-91.
4. O'Connor D, Voronenko Y, Nguyen D, Yin W, Sheng K. Fast non-coplanar beam orientation optimization based on group sparsity. arXiv:1710.05308 [physics.med-ph].

5. O'Connor D, Yu V, Nguyen D, Ruan D, Sheng K. Fraction-variant beam orientation optimization for non-coplanar IMRT. *Phys Med Biol* 2018; **63**(4): 045015.

6. Beck A and Teboulle M. A fast iterative shrinkage-thresholding algorithm for linear inverse problems. *SIAM J Imag Sci* 2009; **2**(1): 183-202.

7. N. Parikh and S. Boyd. Proximal Algorithms. Foundations and Trends in Optimization. Vol. 1, no. 3, pp. 127–239, 2014.

8. Wieser HP, Cisternas E, Wahl N, Ulrich S, Stadler A, Mescher H, et al. Development of the open-source dose calculation and optimization toolkit matRad. *Med. Phys.* 2017; **44** (6): 2556-68.

9. Christiansen E, Heath E, and Xu T. Continuous aperture dose calculation and optimization for volumetric modulated arc therapy. *Phys. Med. Biol.* 2018; **63** (21): 21NT01.

10. Lydon JM. Theoretical and experimental validation of treatment planning for narrow MLC defined photon fields. Phys Med Biol 2005;50:2701-14.

11. Sharpe MB, Miller BM, Yan D, Wong JW. Monitor unit settings for intensity modulated beams delivered using a step-and-shoot approach. Med Phys. 2000;27:2719-25

12. Ezzell GA, Chungbin S. The overshoot phenomenon in step-and-shoot IMRT delivery. J Appl Clin Med Phys 2001;2:138-48.

13. Dong P, Lee P, Ruan D, *et al.* 4π Non-Coplanar Liver SBRT: A Novel Delivery Technique. *Int J Rad Oncol Biol Phys* 2013; **85**(5): 1360-6.

14. Demmel JW. *Applied numerical linear algebra.* 1st ed. Philadelphia, PA. Society for Industrial and Applied Mathematics; 1997.

15. Hårdemark B, Liander A, Rehbinder H, and Löf J. P³IMRT. Direct machine parameter optimization. *Pinnacle white paper*, Nr. 4535 983 02483, Philips (2004).

16. Battista JJ, Chen JZ, Sawchuk S, Hajdok G. Introduction to megavoltage x-ray dose computation algorithms. 1st ed. Boca Raton, FL. Taylor & Francis Group; 2019.

17. McNutt T. Dose calculations – collapsed cone convolution and delta pixel beam. *Pinnacle White Paper* 2007, Nr. 4535 983 02474/870.

18. Shepard DM, Earl MA, Li XA, Naqvi S, and Yu C. Direct aperture optimization: A turnkey solution for step-and-shoot IMRT. *Med. Phys.* 2002; **29** (6): 1007-18.

19. Benedict SH, Yenice KM, Followill D, et al. Stereotactic body radiation therapy: the report of AAPM Task Group 101. Med Phys 2010; 37(8): 4078-101.

20. Pathmanathan AU, van As NJ, Kerkmeijer LGW, *et al.* Magnetic Resonance Imaging-Guided Adaptive Radiation Therapy: A "Game Changer" for Prostate Treatment? *Int J Rad Oncol Biol Phys* 2018; **100**(2): 361-73.

21. Ruchala KJ, Olivera GH, Kapatoes JM, Reckwerdt PJ, Mackie TR. Methods for improving limited field-of-view radiotherapy reconstructions using imperfect a priori images. Med Phys 2002; 29(11): 2590-605.

22. Wang J, Li T, and Xing L. Iterative image reconstruction for CBCT using edge-preserving prior. *Med Phys* 2009; **36**(1): 252-60.

23. Sisniega A, Zbijewski W, Xu J, *et al.* High-fidelity artifact correction for cone-beam CT imaging of the brain. *Phys Med Biol* 2015; **60**(4): 1415-39.

24. Niu T, Sun M, Star-Lack J, Gao H, Fan Q, and Zhu L. Shading correction for on-board cone-beam CT in radiation therapy using planning MDCT images. *Med Phys* 2010; **37**(10): 5395-406.

25. Hansen DC, Landry G, Kamp F, *et al.* ScatterNet: A convolutional neural network for cone-beam CT intensity correction. *Med Phys* 2018; **45**(11): 4916-26.

Appendix A – Feasibility of a unified approach to intensity-modulated radiation therapy and volumetric modulated arc therapy optimization and delivery

This chapter was adapted from the published article entitled "Feasibility of a unified approach to intensity-modulated radiation therapy and volumetric modulated arc therapy optimization and delivery" by Douglas A. Hoover, Michael MacFarlane, Eugene Wong, Jerry J. Battista, and Jeff Z. Chen, Medical Physics, **42** (2): 726-34 (2015). Permission to reproduce this article was granted by John Wiley and Sons, and is provided in Appendix B.5.

A.1   Introduction

Volumetric-modulated arc therapy (VMAT) has been rapidly adopted by the radiotherapy community due primarily to its delivery speed and monitor unit (MU) efficiency, as well as the quality of conformal dose distributions achievable [1-3]. On the other hand, intensity-modulated radiotherapy (IMRT) with its static beam directions might be advantageous in cases where steep dose gradients or highly intensity-modulated beam intensities are required in preferred directions [4]. While the community tends to regard these two delivery techniques as disparate entities, they are in reality special cases of one another. More specifically, there exists a unifying delivery technique which bridges the gap between static-gantry IMRT and rotating-gantry VMAT. Such a unified delivery, if properly implemented into an inverse-planning algorithm, would in general lead to improved dose delivery capabilities as the algorithm could naturally optimize the beam within a given arc range to be more IMRT-like, if greater beam intensity modulation is required, or more VMAT-like, if increased conformity is required with less beam intensity modulation. This combined approach would take advantage of the two modes of beam delivery for targeting and normal tissue sparing.

IMRT or VMAT delivery is typically represented by control points—or multi-leaf collimator (MLC) segments—which are essentially snapshots of the positions of the relevant linear accelerator components taken at regular intervals. For example, a VMAT beam can be stored as a series of control points specifying the machine parameters at

regular 2 or 4 degree intervals of the rotating gantry. Due to the large number of degrees-of-freedom required to specify a VMAT beam, all VMAT radiotherapy plans are created using specialized optimization software, such as SmartArc in Pinnacle (Philips Healthcare, Fitchburg, USA) or RapidArc in Eclipse (Varian Medical Systems, Palo Alto, USA). Both commercial treatment planning systems optimize beam parameters specifically for equally-spaced gantry positions. In addition to commercially-available software, a number of research prototypes have been developed to test novel optimization algorithms including the concept of unequally-spaced control points [5,6]. In principle, VMAT and IMRT with and without gantry rotation, respectively, can be unified during optimization and delivery. Instead of forcing the beam angle increments for arc therapy, the fixed-gantry IMRT parameters can add additional degrees of freedom available to the optimization engine.

The idea to combine VMAT and IMRT deliveries is not new, and various ideas have been implemented to improve the current clinically-available VMAT implementations. One suggestion, termed dense angularly sampled and sparse intensity modulated radiation therapy (DASSIM-RT), proposes a method to search more thoroughly through the parameter space of machine-deliverable radiotherapy plans [7]. One major hurdle towards the clinical implementation of this method is that the scale of the optimization problem is now immense and so much greater computer memory is required [8]. Another proposal, Arc Modulated Radiation Therapy (AMRT), builds on previous work in intensity modulated arc therapy (IMAT) [1]. AMRT is a sequencing algorithm that allows multiple IMAT arcs to be delivered by a single arc. In one study, AMRT plans required on the order of 200-400 segments and achieved similar plan quality to IMRT [9].

Yet another proposal, termed FusionArc, has recently been published [10]. This paper describes an in-house optimization software that begins with a full VMAT optimization followed by an iterative conversion, at select gantry angles, from uniform to intensity-modulated fluence. Gantry angles are selected for conversion based on a gradient function which attempts to predict conversions that will lead to the greatest reduction in the cost function. Brainlab (Feldkirchen, Germany) has introduced a commercial platform

which first optimizes a dynamic conformal arc delivery phase followed by an optimization of an IMRT phase. However, the arc phase is restricted by constant angular speed and dose rate. Furthermore, the arc ranges, the number of uniformly spaced IMRT fields, and the relative weighting of arc and fixed-gantry IMRT phases must all be chosen from the outset of optimization [11]. The quality of HybridArc plans has been shown to depend on a proper selection of these initial parameters [12].

None of the solutions described above has yet embodied the fully-integrated and unified approach that we advocate here. The purpose of this work is to create, as a proof-of-principle, a unified intensity-modulated arc therapy (UIMAT) that combines IMRT and VMAT optimization and delivery in order to produce efficient and superior radiation treatment plans in a single optimization with concurrent VMAT and IMRT features

A.2   Material and Methods

A.2.1 Inverse Planning for UIMAT

Custom software was developed and integrated into a commercial treatment planning system, Pinnacle[3] v9.6 Radiation Therapy Planning Systems (Philips Healthcare, Fitchburg, USA) for the purpose of testing whether UIMAT is superior to either standard VMAT or IMRT. This software extends Pinnacle's built-in VMAT optimization in a few key ways. Firstly, it removes the restriction that control points within a dynamic arc must have a uniform angular spacing. Importantly, this allows arc segments that would benefit from increased intensity modulation to have more densely packed control points. Furthermore, angles requiring this increased modulation are selected automatically during the initial optimization stage, and this can be thought of as a form of beam-angle optimization.

Our optimization algorithm begins by creating static beams uniformly distributed between start and stop arc angles with an initially coarse control point spacing of twenty-four degrees, as suggested by Bzdusek [13]. Using Pinnacle's inverse-planning system, an optimized fluence pattern is determined for these initial beams. In general, these

fluence patterns will not be machine-deliverable and so a sequencing step is then performed which converts the fluence patterns into executable MLC control points.

Custom software is then initiated which reads in this beam information from Pinnacle software. As a preparatory step, the code first re-orders the control points within each individual beam, anticipating that these control points may later be distributed—or fanned out—into other gantry angles to form an arc segment. The goals of this re-ordering step are: (1) to preferentially place higher-weighted control points towards the middle of the order, thereby minimizing the dosimetric differences between the original and the fanned-out beams (see Figure A.1); and (2) to minimize MLC motion between control points, thereby improving delivery efficiency. Note that for any given solution, there will always be a "symmetric" solution having the reverse control point order. However, this symmetry is broken once neighboring beams are considered, and so for each beam the software determines whether the original or reverse order will result in the least MLC motion between the first and last control points of neighboring beams.
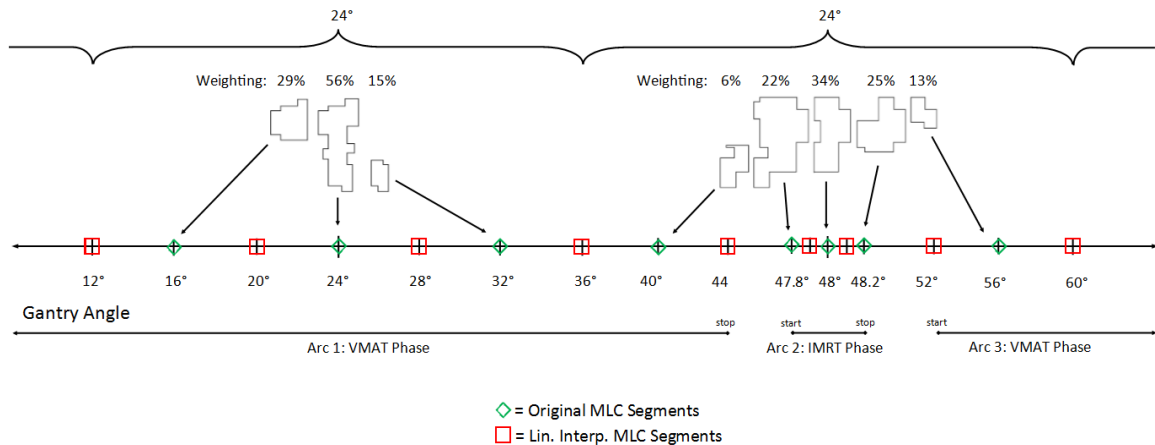
Figure A.1: Schematic showing how the control points from the initial fixed-beam optimization are distributed into VMAT and IMRT phases. Control points within each beam have been re-ordered to minimize MLC motion. As well, higher-weighted control points are preferentially placed in the middle of the ordering to minimize the difference between the initial and final gantry angles. Interpolated MLC segments are inserted as necessary to maintain a maximum control point spacing of four degrees.

The algorithm next determines which of these beams should remain as IMRT fields and which should be converted into arc segments. In our current implementation, we chose to convert those beams having fewer than four control points (low modulation) into a "VMAT phase", while those beams with four or more control points were retained for the "IMRT phase" (high modulation). In this study, the threshold to distinguish between low and high modulation corresponds approximately to the average number of control points per beam which in turn depends on the MLC sequencing parameters chosen. Based on the parameters we chose, on average, we had 4 control points per beam which we found to work well practically for the anatomical sites tested.

Finally, the algorithm modifies the gantry angle associated with each beam segment as shown in Figure A.1. Beams that have low modulation become VMAT phases where their control points are distributed uniformly within the 24 degree spacing. In order to maintain approximately four-degree spacing between control points, linear interpolation of MLC leaves is used to create new interlaced control points as needed. Beams that have high modulation become IMRT phases. In this case, the first and last control points have their gantry angles shifted 8 degrees on either side of the initial gantry angle, as shown in Figure A.1. These two boundary control points, together with linearly interpolated control points, are used to facilitate a smooth transition from VMAT to IMRT phases. Next, the central control points of high-modulation beams are fanned out around the initial gantry angle in 0.2° increments. Interpolated control points are then added between these central control points to arrive at a 0.1° spacing for the IMRT phase. The small gantry rotation (almost stalled) for the IMRT phase approximates a static-gantry IMRT field and is a work-around for the fact that Pinnacle v9.6 does not allow simultaneous DMPO optimization of static-gantry IMRT and VMAT beams. At this stage, the beam control points are re-imported into Pinnacle for a final optimization using the DMPO algorithm. As an example, the start and stop angles for these partial arcs, as well as the angular location of the IMRT phases, are shown in Figure A.2.

Certain "soft" deliverability constraints are relaxed for the IMRT-like portions of delivery. Specifically, for the IMRT phases the maximum MU per degree is increased from 20 to 200, and the gantry acceleration limit is removed. Within Pinnacle software,

this is accomplished by defining a separate machine having these special properties and associating the IMRT phases with this virtual machine. This is required in order to have a reasonable number of MUs delivered during the more highly-modulated IMRT phase, which may have up to ten control points within one degree angular spacing. It is important to note that such a beam is still machine-deliverable as it does not violate any physical constraints of the accelerator.
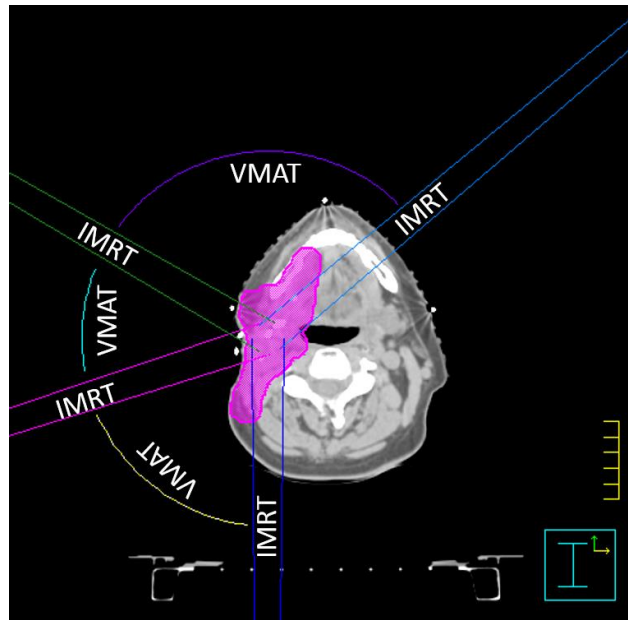
Figure A.2: A typical UIMAT plan. The angular ranges for three VMAT phases are represented by arc segments while the fixed gantry angles corresponding to four IMRT phases are represented by straight line pairs.

From this point on, optimization proceeds using the standard functionality within Pinnacle. Machine parameters for both IMRT phases and VMAT phases are optimized at the same time as multiple dynamic arcs in Pinnacle software. DMPO optimization is continued until a clinically-acceptable plan is obtained using standard dose-volume histogram (DVH) constraints. During optimization, the VMAT and IMRT phases are treated as separate beams, and after optimization is complete, our custom software is used to combine the VMAT and IMRT phases into a single UIMAT arc with variable gantry speed for final dose calculation and delivery. The final dose is calculated by collapsed-cone convolution algorithm in the Pinnacle treatment planning system.

A.2.2 Treatment Plan Evaluation

In order to test our optimization algorithm, CT scans from 15 previously treated patients were selected for planning comparison purposes. Five cases each were randomly selected from head-and-neck, lung, and prostate sites to represent a variety of anatomy, complexity levels, and delivery modalities. All clinical treatment plans were optimized using the Pinnacle treatment planning system. A summary of the selected patient plans is provided in Table A.1 with the estimated delivery times obtained from Pinnacle. Since Pinnacle does not provide an estimate for step-and-shoot beams, the delivery time for IMRT plans was measured on a Varian linear accelerator. The IMRT delivery time is defined here as the total time from when the first beam turns on until the last beam turns off and so includes the "mode-up" time as well as the time required to move to the various gantry positions. Beams were ordered for the most efficient delivery. A paired, two-tailed t-test was used to assess for statistically significant differences in delivery times.

Table A.1: Comparison of clinically-delivered treatments with UIMAT treatment plans. Note that some patients had multiple target volumes with distinct dose levels (e.g. Patient 3 had both a 70 Gy and a 56 Gy target volume). Approximate treatment delivery times are given.

	Patient	Site	Dose Pres. [Gy]	Beam Arrangement		Delivery Time [s]	
				Clinical	UIMAT	Clinical	UIMAT
Head & Neck	1	Lt. Parotid	64/60/54	2x 210° (108 CP)	1x 210° (65 CP)	91	64
	2	Rt. Parotid	60	2x 225° (116 CP)	1x 225° (55 CP)	95	68
	3	Larynx/Neck	70/56	2x 360° (182 CP)	1x 360° (87 CP)	151	171
	4	Parotids/Neck	70/56	2x 360° (182 CP)	1x 360° (89 CP)	151	201
	5	Larynx	61/50	5 Fields (23 CP)	1x 260° (77 CP)	182	109
Lung	6	Lt. Lung	60	5 Fields (17 CP)	1x 230° (73 CP)	167	64
	7	Lt. Lung	60	2x 225° (116 CP)	1x 225° (63 CP)	94	67
	8	Rt. Lung	60	6 Fields (21 CP)	1x 192° (61 CP)	237	126
	9	Rt. Lung	60	2x 210° (108 CP)	1x 210° (63 CP)	90	98
	10	Lt. Lung & Mediastinum	50	2x 360° (181 CP)	1x 360° (93 CP)	149	100
Prostate	11	Prostate	76	1x 360° (91 CP)	1x 360° (99 CP)	79	129
	12	Prostate Bed	66	2x 360° (182 CP)	1x 360° (97 CP)	151	200
	13	Prostate	45	2x 360° (182 CP)	1x 360° (103 CP)	150	236
	14	Prostate Bed	76/50.4	2x 360° (182 CP)	1x 360° (93 CP)	154	241
	15	Prostate	66	2x 360° (182 CP)	1x 360° (96 CP)	151	139

Abbreviations: Pres, prescription; Rt, right; Lt, left; UIMAT, unified intensity modulated arc therapy; CP, control points

The UIMAT plans were optimized based on our local treatment planning guidelines used to generate the clinical plans. Without exception, critical structure tolerances such as the spinal cord and brainstem were respected. For lung cases, the volume of both lungs receiving at least 20 Gy (V20) was kept below 35% and a mean lung dose of < 20 Gy was also maintained. The dose coverage goal for the planning target volume (PTV) was to cover at least 95% of the PTV by at least 95% of the prescription dose. For non-critical structures, DVH criteria from RTOG 0126 and QUANTEC [14] were used to guide the planning process. All UIMAT plans were restricted to a single arc. Dynamic jaw movements were allowed in order to facilitate the goal of a single-arc delivery. Dynamic jaws were required when treating large volumes with a single arc due to the finite speed

and length of the MLC leaves. It is noted that the clinical plans did not require dynamic jaws, as all complicated VMAT plans standardly use two arcs.

To compare a UIMAT plan with the corresponding clinical VMAT or IMRT plan for each patient, various dose metrics were selected and subjected to a paired, one-tailed t-test to assess statistically significant differences. Mean doses for PTVs and conformity index (CI) were analyzed for all cases. The conformity index has been previously defined as [15]:

$$CI = (Cover\ factor) \times (Spill\ Factor)$$
$$= \left(\frac{V_{100}(PTV)}{V_{PTV}}\right) \times \left(\frac{V_{100}(PTV)}{V_{100}(Body)}\right) \tag{1}$$

where $V100(PTV)$ and $V100(body)$ are the volumes of the 100% prescription dose within the PTV and body, respectively, and V_{PTV} is the volume of the PTV. For head-and-neck cases, mean doses for parotids, oral cavity, larynx, and maximum doses for cord, brainstem, and larynx were analyzed. For lung cases, mean doses for lung, esophagus, and heart were recorded as well as the lung V20 and the maximum cord dose. For prostate cases, mean doses for rectum, bladder, bowel, and femurs were analyzed. The threshold for statistical significance was set at a *p*-value of 0.05.

The deliverability of UIMAT plans was tested on a Varian TrueBeam linear accelerator (Varian Medical Systems, Palo Alto, USA). The accuracy of dose calculations and delivery was verified by measurements with the ArcCheck Phantom (Sun Nuclear, USA).

A.3 Results

A.3.1 Feasibility

The UIMAT plans were generated for 15 cases, as summarized in Table A.1. UIMAT plans employed only one arc, while most of the clinical VMAT plans required two arcs. The number of MLC control points in the UIMAT plans were less than the VMAT plans for all but one case (see Table A.1), but more than in the IMRT plans. The estimated delivery times for UIMAT plans were not significantly different from the VMAT plans

(p=0.22) but they were significantly faster than multiple-field IMRT plans (p=0.01). No significant difference in delivery time was observed between the UIMAT plans and the VMAT and IMRT plans taken together (p=0.75).

An ArcCheck measurement in each treatment site was made to verify the accuracy of UIMAT dose calculation and feasibility of delivery. All tested plans had a gamma passing rate [16] of greater than 95% using our standard clinical parameters of 3% dose difference and 3 mm distance-to-agreement.

A.3.1 Plan Comparison

A.3.1.a - Head and Neck

The dose metrics used in the evaluation of the head-and-neck cases are presented in Table A.2. Plans which have multiple PTVs, as listed in Table A.1, have one conformity index (CI) reported for each PTV. For patient 5, the low doses associated with most OARs are related to the small treatment volume which is restricted to the laryngeal region of the neck. For the five head-and-neck cases, the overall average of the mean OAR doses in Table A.2 was reduced by 8.4% (p<0.001) using UIMAT plans compared to the clinical VMAT or IMRT plans. As a specific example, comparison of the dose distributions and DVHs between a UIMAT and a VMAT plan for a head-and-neck case is shown in Figure A.3. It shows that the UIMAT plan produced lower OAR doses with similar PTV coverage compared with the clinical VMAT plan.

Table A.2: Dose volume parameters of interest for five head-and-neck cases. The mean PTV dose is represented as a percentage of the prescription dose. Certain OARs were not contoured for some patients, either because the OAR was well outside the treatment volume or because it was completely enclosed within the PTV. The conformity indices correspond to the target volumes listed in the third-last column, and similarly for the mean PTV doses. Since not all patients had the same number of PTV dose levels, P values and average doses for PTVs were calculated for the highest dose level only.

No.	Plan	Oral Cavity $\bar{D}$ [Gy]	Left Parotid $\bar{D}$ [Gy]	Right Parotid $\bar{D}$ [Gy]	Larynx $\bar{D}$ [Gy]	Larynx D_{max} [Gy]	Brainstem D_{max} [Gy]	Cord D_{max} [Gy]	PTV(s) Pres. [Gy]	Conformity Index	PTV(s) $\bar{D}$ [%]
1	Clinical	28.4	6.9	--	31.8	62.3	15.0	22.4	64/60/54	0.21/0.77/0.63	99.8/101.5/103.5
	UIMAT	22.6	2.4	--	26.8	61.2	9.5	24.5		0.14/0.79/0.63	101.9/102.6/103.7
2	Clinical	30.0	5.9	61.0	27.8	62.6	13.8	36.7	60	0.85	101.3
	UIMAT	27.7	3.3	60.8	26.3	63.1	10.9	37.4		0.80	101.5
3	Clinical	33.2	25.9	25.6	--	--	32.2	36.9	70/56	0.83/0.79	100.0/101.8
	UIMAT	29.9	23.1	22.4	--	--	33.3	44.3		0.70/0.70	101.7/102.6
4	Clinical	39.3	25.3	25.4	48.6	65.1	44.3	44.8	70/56	0.78/0.72	100.6/104.5
	UIMAT	37.3	22.5	22.9	47.7	58.0	46.0	23.4		0.82/0.71	100.7/103.6
5	Clinical	0.2	0.2	0.2	55.5	64.2	0.2	0.2	61/50	0.89/0.73	101.0/109.6
	UIMAT	0.2	0.2	0.2	55.5	64.0	39.8	23.6		0.93/0.73	101.6/108.6
Avg.	Clinical	26.2	12.8	28.0	40.9	63.6	21.1	31.8		0.72	102.4
	UIMAT	23.6	10.3	26.6	39.0	61.6	20.0	34.9		0.7	102.9
P value		0.02	0.01	0.09	0.09	0.17	0.23	0.04		0.11	0.08

Abbreviations: **PTV, planning target volume; OAR, organ at risk; UIMAT, unified intensity modulated arc therapy; $\bar{D}$, mean dose; D$_{max}$, maximum dose; Avg, average**

Figure A.3: Comparison of dose distributions between a clinical VMAT plan (top left) and a UIMAT plan (top right) and corresponding dose volume histograms (bottom) for a head-and-neck case (patient 1).

A.3.1.b - Lung

The dose metrics used in the evaluation of the lung cases are presented in Table A.3.

UIMAT yielded significant reductions for the mean doses for heart and esophagus, and maximum cord dose compared with clinical IMRT or VMAT plans, while the difference in V20, mean lung dose, conformity index, and mean PTV dose is not statistically significant. The overall average of the mean OAR doses in Table A.3 was reduced by 5.7% (p<0.001) using UIMAT plans compared with clinical IMRT or VMAT plans

Table A.3: Dose volume parameters of interest for five lung cases. The mean PTV dose is represented as a percentage of the prescription dose.

No.	Plan	Lung V20 [%]	Lung $\overline{D}$ [Gy]	Esophag us $\overline{D}$ [Gy]	Heart $\overline{D}$ [Gy]	Cord D_{max} [Gy]	CI	PTV $\overline{D}$ [%]
6	Clinical	15.1	9.8	17.1	1.2	29.5	0.72	101.7
	UIMAT	14.9	9.2	15.7	1.0	27.9	0.87	102.0
7	Clinical	21.9	14.0	22.4	10.1	35.6	0.87	101.3
	UIMAT	22.1	14.0	21.2	8.3	34.8	0.91	101.3
8	Clinical	30.5	17.2	25.0	11.0	47.8	0.79	103.5
	UIMAT	27.8	15.5	22.7	10.6	47.4	0.91	101.5
9	Clinical	20.7	11.8	24.4	4.8	43.3	0.78	101.3
	UIMAT	20.7	11.5	23.3	3.8	41.2	0.81	101.3
10	Clinical	35.6	18.6	36.2	30.6	43.4	0.92	100.2
	UIMAT	34.4	18.1	35.5	29.4	42.5	0.88	101.0
Avg.	Clinical	24.8	14.3	25.0	11.5	39.9	0.82	101.6
	UIMAT	24.0	13.7	23.7	10.6	38.8	0.88	101.4
P value		0.12	0.05	0.003	0.01	0.01	0.08	0.37

Abbreviations: PTV, planning target volume; CI, conformity index; V20, percent volume of lung receiving at least 20 Gy; $\overline{D}$, mean dose; D_{max}, maximum dose; UIMAT, unified intensity modulated arc therapy; Avg, average

As a specific example, comparison of the dose distributions and DVHs between a UIMAT and a 5-field IMRT plan for a lung case is shown in Figure A.4. The UIMAT plan produced more conformal and uniform dose to the PTV and lower doses to left lung, esophagus, and spinal cord compared with the IMRT plan.
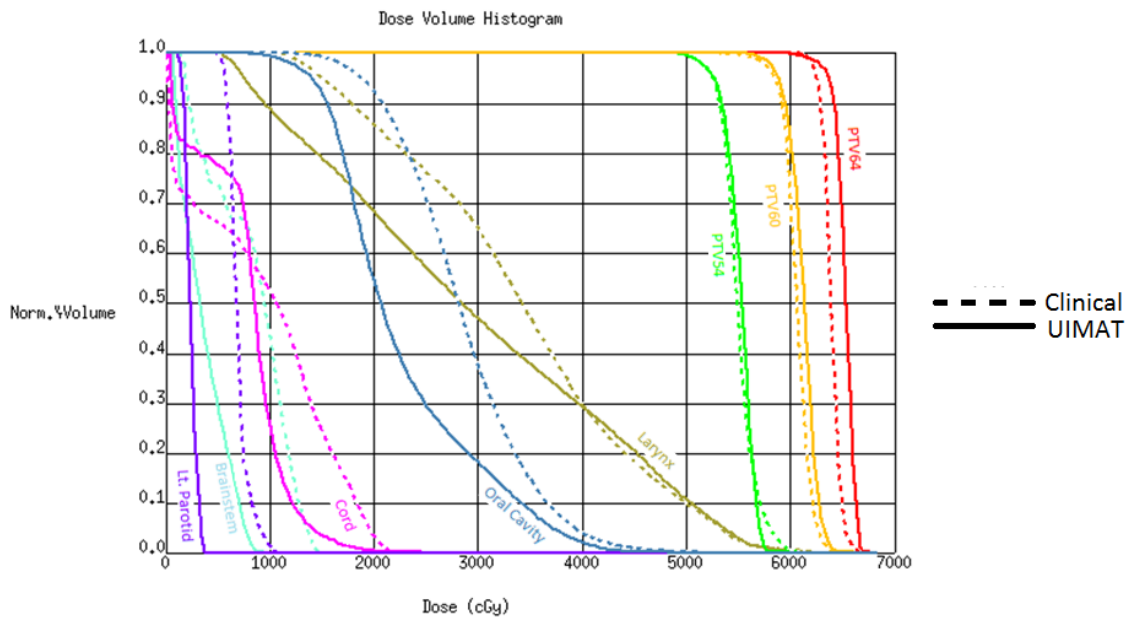
Figure A.4: Comparison of dose distributions between a clinical IMRT plan (top left) and a UIMAT plan (top right) and corresponding dose volume histograms (bottom) for a lung case (patient 6).

A.3.1.b - Prostate

The dosimetric parameters of UIMAT and clinical VMAT plans for five prostate cases are shown in Table A.4. The multiple conformity indices for patient 14 correspond to the multiple PTVs within the plan. No significant dosimetric difference was observed between UIMAT and VMAT plans for the prostate cases studied. The overall average of the mean OAR doses listed in Table A.4 was reduced by 3.5% (p=0.009) using UIMAT compared with VMAT plans. As a specific example, comparison of the dose distributions

and DVHs between a UIMAT and a VMAT plan for a prostate case is shown in Figure A.5. In this case, the UIMAT plan is dosimetrically similar to the clinical VMAT plan.
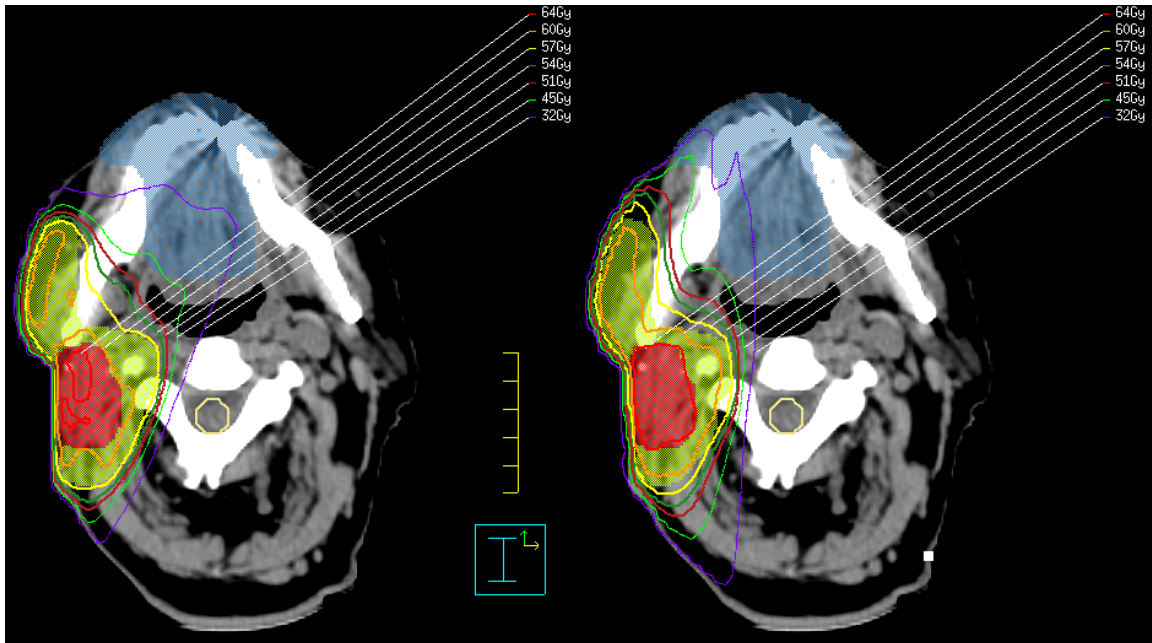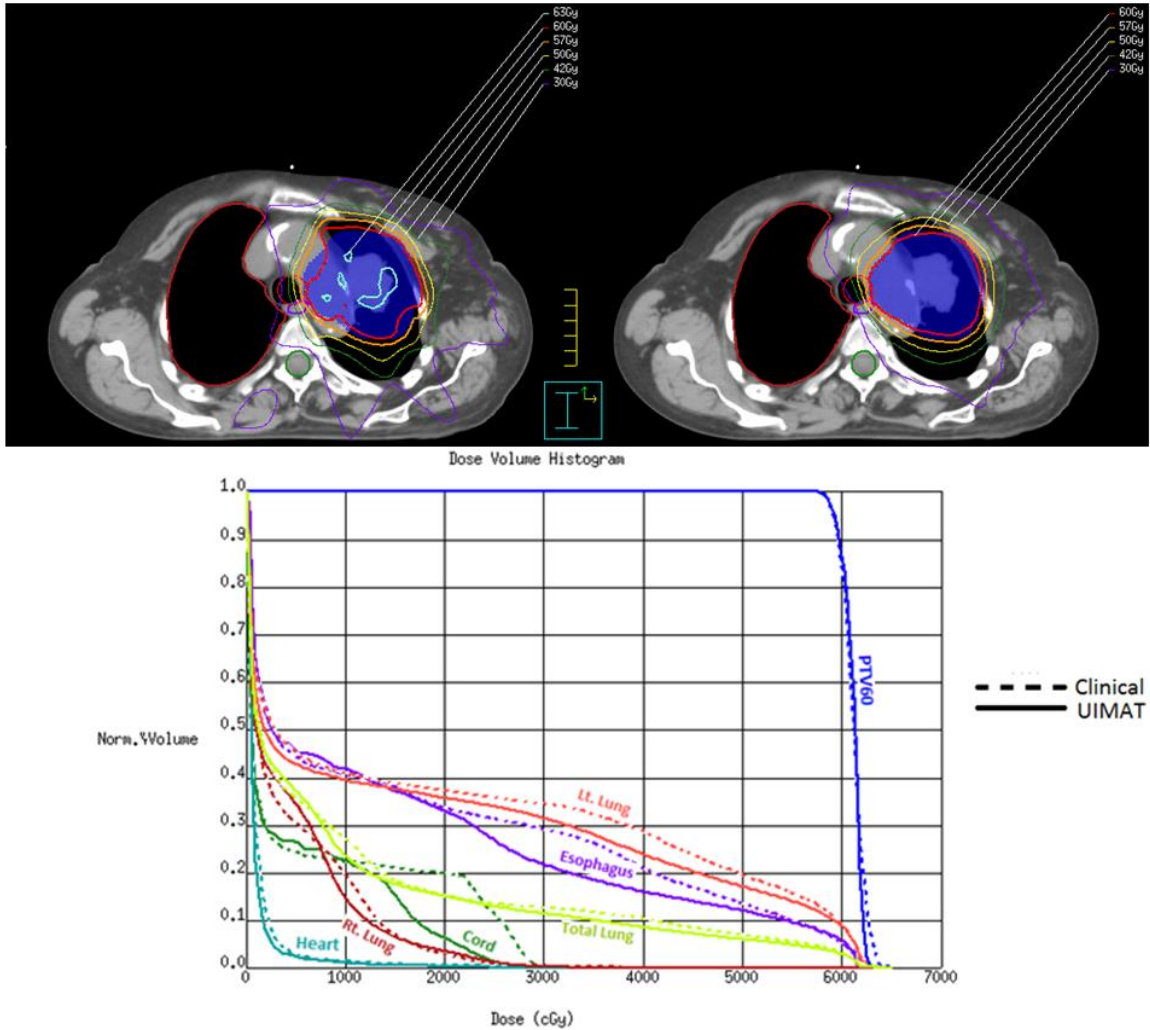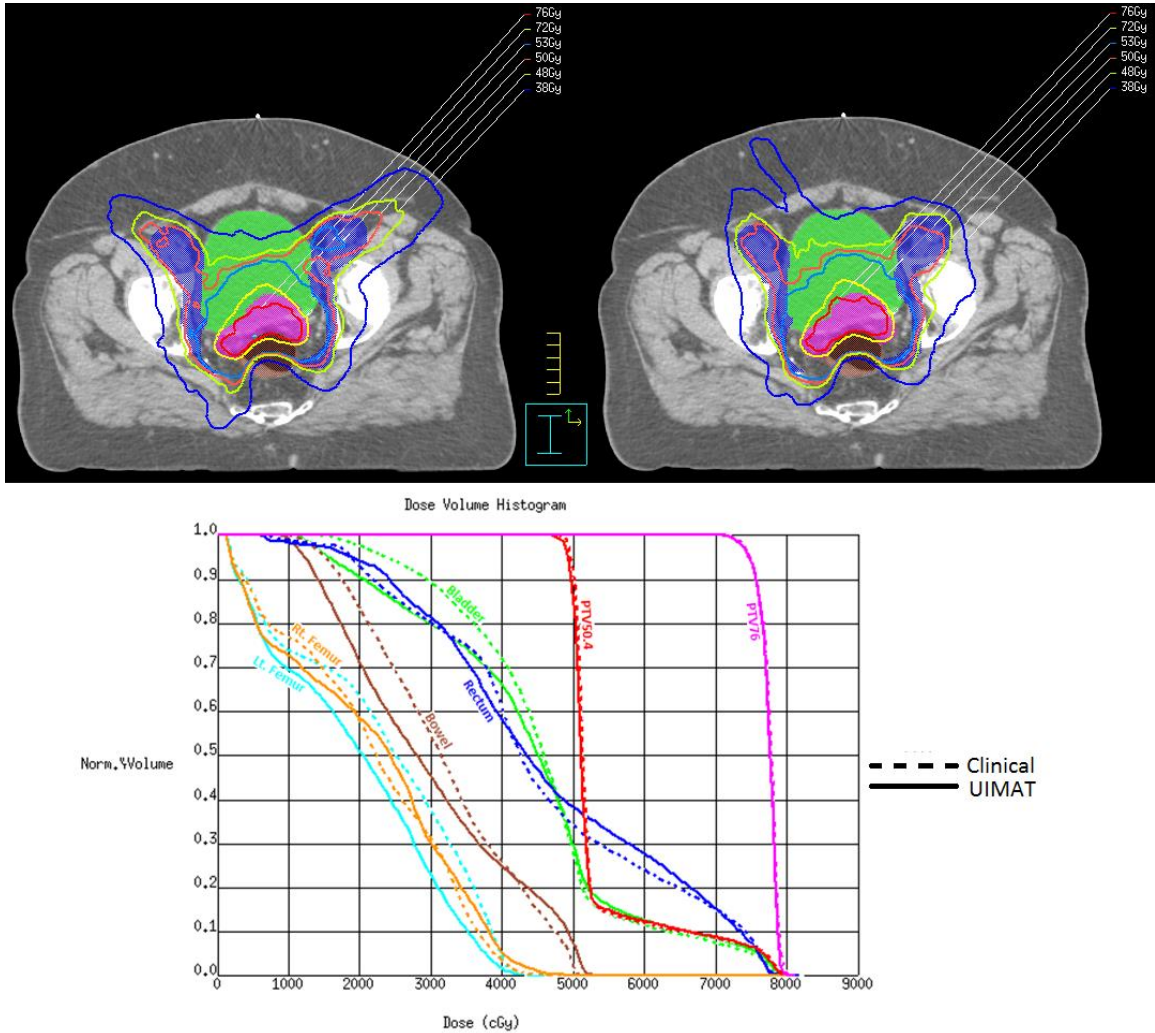

Figure A.5: Comparison of dose distributions between a clinical VMAT plan (top left) and a UIMAT plan (top right) and corresponding dose volume histograms (bottom) for a prostate case (patient 14).

Table A.4: Dose volume parameters of interest for five prostate cases. The bowel was not contoured for two patients as it lay well outside the treatment volume. The conformity indices correspond to the target volumes listed in the third-last column, and similarly for the mean PTV doses. Since not all patients had the same number of PTV dose levels, P values for PTVs were calculated for the highest dose level only.

No.	Plan	Rectum $\bar{D}$ [Gy]	Bladder $\bar{D}$ [Gy]	Bowel $\bar{D}$ [Gy]	Lt. Femur $\bar{D}$ [Gy]	Rt. Femur $\bar{D}$ [Gy]	PTV(s) Pres. [Gy]	Conformity Index	PTV $\bar{D}$ [%]
11	Clinical	41.4	15.0	--	19.0	22.6	76	0.83	101.4
	UIMAT	39.2	12.3	--	16.3	17.6		0.85	101.9
12	Clinical	41.4	54.3	53.1	22.4	16.5	66	0.82	98.2
	UIMAT	42.8	55.5	52.2	20.8	20.8		0.87	98.1
13	Clinical	34.2	34.2	28.8	16.1	15.3	45	0.78	103.4
	UIMAT	32.2	33.4	26.3	16.2	13.8		0.84	101.9
14	Clinical	45.6	45.5	31.6	22.9	21.5	76/50.4	0.91/.0.60	102.0/107.0
	UIMAT	46.4	43.8	29.7	19.4	21.6		0.88/0.59	102.2/106.6
15	Clinical	32.3	17.9	--	23.4	23.3	66	0.91	100.9
	UIMAT	32.1	17.8	--	21.7	22.5		0.84	100.9
Average	Clinical	39.0	33.4	37.85	20.8	19.8		0.81	102.1
	UIMAT	38.6	32.6	36.1	18.9	19.3		0.81	101.9
P value		0.29	0.16	0.03	0.02	0.37		0.39	0.26

Abbreviations: PTV, planning target volume; Lt, left; Rt, right; Pres, prescription; $\bar{D}$, mean dose; UIMAT, unified intensity modulated arc therapy

A.4 Discussion

We have shown that it is feasible to optimize and deliver UIMAT which combines VMAT and IMRT within the same arc. We have also shown how the degree of intensity modulation can be naturally incorporated into an algorithm which dynamically varies the angular density of the beam control points. Compared with clinical VMAT or IMRT plans, UIMAT has the potential to produce efficient and superior radiation dose distributions, especially for complex anatomy such as in head-and-neck cancers. On the other hand, for the sites with more rotational symmetry, such as prostate, UIMAT may not yield significant advantages as it resulted in plans with comparable dosimetric performance but less efficient delivery compared with VMAT.

One of the virtues of our proposal is that the switch from the current VMAT technique to our unified approach would, in principle, be seamless. Treatment planning for UIMAT would be the same as for VMAT as no selection of static beam directions is required. Similarly, radiation therapists delivering the treatment would not need to perform any additional steps beyond what is commonly done for stand-alone VMAT delivery, although they must be made aware of the stopped gantry during IMRT phases of UIMAT delivery. Another benefit of our proposal is the ease at which it can be incorporated into a working clinical system, thus decreasing both cost and time between conception and clinical implementation. Of course, in practice, the introduction of this technique, as with all new techniques, would require additional quality assurance and testing.

Compared with other IMRT/VMAT combination techniques [7-12], our proposal offers simplicity in integration, optimization, and delivery. Our UIMAT proposal is not simply an IMRT/VMAT hybrid technique. It would be more correct to refer to it as a more fully-realized implementation of VMAT with fuller range of gantry speed that even permits gantry stalls, thus allowing for optimal beam modulation. What we have demonstrated is one specific implementation of UIMAT, and in principle, it could be generalized further. UIMAT could be further developed with more robust segmentation and optimization algorithms, as well as more degrees of freedom such as collimator

angle, couch position, and couch angle. Such future developments could hopefully address certain limitations within our initial implementation of UIMAT. For example, once the initial gantry directions are chosen for IMRT phases at the start of optimization, they cannot be altered at a later point in the optimization. For most cases this should not be a problem, except if the objective function changes dramatically between initial and final optimization. It should be noted that the same is true for VMAT and IMRT planning. After the fluence map conversion takes place, it becomes much easier for the optimization routine to become trapped in local minima.

In the planning comparison portion of this work, we acknowledge the usual biases and confounders inherent in such an approach. For example, there is a natural tendency towards demonstrating that a new treatment is superior to the standard-of-care. More effort may be spent optimizing the new technique, or choosing comparison endpoints that naturally favor the new method. Unfortunately, requiring the matching of equal planning effort is not practical, but we were conscious in avoiding "over-optimizing" the UIMAT plans. In this retrospective study, the actual difference in planning time was not logged precisely. Depending on the complexity of the case, clinical planning in our experience requires 1 to 4 hours. To ensure a fair planning comparison, we restricted UIMAT planning times to fall within a similar range.

We acknowledge that the number of cases tested in this feasibility study is very limited and so the statistics reported only highlight general trends. More cases are needed for each treatment site to confirm the conclusions reached. Finally, as mentioned earlier, dynamic jaws are needed when treating large volumes with a single arc due to the finite speed and length of the MLC leaves. This is an obvious advantage for UIMAT as it allows more freedom for collimating the beam; however comparable degrees of freedom were still available in our clinical plans but required more than one arc with differing jaw positions.

Compared to other published techniques [7-12] combining IMRT and VMAT, UIMAT is unique in that it possesses all of the following features: 1) it creates VMAT and IMRT phases automatically; 2) it optimizes VMAT and IMRT phases

simultaneously; 3) the VMAT and IMRT phases are combined and delivered in a single dynamic arc; 4) the algorithm has been implemented on a commercial treatment planning system; 5) the UIMAT plans have been validated using the ArcCheck phantom, delivered in clinical mode on a Varian TrueBeam linear accelerator. Theoretically, it is known that the increased degrees of freedom afforded by the IMRT phases of the arc will in principle lead to a superior plan, all other things being equal. What we have shown is that this appears to be the case, even with this simple initial implementation. Further improvements in the optimization beyond what is possible within a commercial treatment planning software should lead to even better results. Last but not least, our work shows that the UIMAT delivery speed is improved over IMRT or when multiple VMAT arcs are required.

A.5 Conclusion

We have demonstrated the feasibility of a novel radiation therapy delivery technique termed UIMAT. This technique combines VMAT and IMRT optimization concurrently and delivers radiation in a single arc. The optimal fixed-gantry IMRT phases are chosen automatically during the optimization. Optimization of both the VMAT and fixed-gantry IMRT phases of delivery occur simultaneously and the final plan is an integrated UIMAT plan. Initial results show that the UIMAT has the potential to be superior to either stand-alone IMRT or VMAT in terms of dose distribution quality and efficiency of delivery.

A.6 Acknowledgements

A.7 Reference

1. Yu, C.X., *Intensity-modulated arc therapy with dynamic multileaf collimation: an alternative to tomotherapy.* Phys. Med. Biol. , 1995. **40**(9): p. 1435-1499.

2. Otto, K., *Volumetric modulated arc therapy: IMRT in a single gantry arc.* Medical Physics, 2008. **35**(1): p. 310-317.

3.   Shepard, D.M., et al., *An arc-sequencing algorithm for intensity modulated arc therapy.* Med. Phys. , 2007. **34**(2): p. 464-470.

4.   Jiang, X., et al., *Planning analysis for locally advanced lung cancer: dosimetric and efficiency comparisons between intensity-modulated radiotherapy (IMRT), single-arc/partial-arc volumetric modulated arc therapy (SA/PA-VMAT).* Radiation Oncology, 2011. **6**: p. 140.

5.   Craft, D., et al., *Multicriteria VMAT optimization.* Med Phys, 2012. **39**(2): p. 686-96.

6.   Peng, F., et al., *A new column-generation-based algorithm for VMAT treatment plan optimization.* Phys Med Biol, 2012. **57**(14): p. 4569-88.

7.   Li, R. and L. Xing, *Bridging the gap between IMRT and VMAT: dense angularly sampled and sparse intensity modulated radiation therapy.* Med Phys, 2011. **38**(9): p. 4912-9.

8.   Kim, H., et al., *Dose optimization with first-order total-variation minimization for dense angularly sampled and sparse intensity modulated radiation therapy (DASSIM-RT).* Med Phys, 2012. **39**(7): p. 4316-27.

9.   Wang, C., et al., *Arc-modulated radiation therapy (AMRT): a single-arc form of intensity-modulated arc therapy.* Phys Med Biol, 2008. **53**(22): p. 6291-303.

10.   Matuszak, M.M., et al., *FusionArc optimization: a hybrid volumetric modulated arc therapy (VMAT) and intensity modulated radiation therapy (IMRT) planning strategy.* Med Phys, 2013. **40**(7): p. 071713.

11.   Gevaert, T., et al., *Implementation of HybridArc treatment technique in preoperative radiotherapy of rectal cancer: dose patterns in target lesions and organs at risk as compared to helical Tomotherapy and RapidArc.* Radiation Oncology, 2012. **7**: p. 120.

12.   Robar, J.L. and C. Thomas, *HybridArc: a novel radiation therapy technique combining optimized dynamic arcs and intensity modulation.* Med. Dosim. , 2012. **37**(4): p. 358-368.

13.   Bzdusek, K., et al., *Development and evaluation of an efficient approach to volumetric arc therapy planning.* Medical Physics, 2009. **36**(6): p. 2328.

14. Marks, L.B., et al., *Use of normal tissue complication probability models in the clinic.* Int. J. Radiat. Oncol. Biol. Phys, 2010. **76**(3): p. S10-S19.

15. Oozeer, R., et al., *Dosimetric evaluation of conformal radiotherapy: conformity factor.* Cancer Radiother. , 2000. **4**(3): p. 207-216.

16. Low, D.A., et al., *A technique for the quantitative evaluation of dose distributions.* Med. phys., 1998. **25**(5): p. 656-661.

Appendix B – Permission to Reproduce Content

B.1 Permission to reuse figure from Bzdusek et al. in Figure 1.2

(collectively "WILEY"). By clicking "accept" in connection with completing this licensing transaction, you agree that the following terms and conditions apply to this transaction (along with the billing and payment terms and conditions established by the Copyright Clearance Center Inc., ("CCC's Billing and Payment terms and conditions"), at the time that you opened your RightsLink account (these are available at any time at http://myaccount.copyright.com).

Terms and Conditions

- The materials you have requested permission to reproduce or reuse (the "Wiley Materials") are protected by copyright.

- You are hereby granted a personal, non-exclusive, non-sub licensable (on a stand-alone basis), non-transferable, worldwide, limited license to reproduce the Wiley Materials for the purpose specified in the licensing process. This license, **and any CONTENT (PDF or image file) purchased as part of your order,** is for a one-time use only and limited to any maximum distribution number specified in the license. The first instance of republication or reuse granted by this license must be completed within two years of the date of the grant of this license (although copies prepared before the end date may be distributed thereafter). The Wiley Materials shall not be used in any other manner or for any other purpose, beyond what is granted in the license. Permission is granted subject to an appropriate acknowledgement given to the author, title of the material/book/journal and the publisher. You shall also duplicate the copyright notice that appears in the Wiley publication in your use of the Wiley Material. Permission is also granted on the understanding that nowhere in the text is a previously published source acknowledged for all or part of this Wiley Material. Any third party content is expressly excluded from this permission.

- With respect to the Wiley Materials, all rights are reserved. Except as expressly granted by the terms of the license, no part of the Wiley Materials may be copied, modified, adapted (except for minor reformatting required by the new Publication), translated, reproduced, transferred or distributed, in any form or by any means, and no derivative works may be made based on the Wiley Materials without the prior permission of the respective copyright owner.**For STM Signatory Publishers clearing permission under the terms of the STM Permissions Guidelines only, the terms of the license are extended to include subsequent editions and for editions in other languages, provided such editions are for the work as a whole in situ and does not involve the separate exploitation of the permitted figures or extracts,** You may not alter, remove or suppress in any manner any copyright, trademark or other notices displayed by the Wiley Materials. You may not license, rent, sell, loan, lease, pledge, offer as security, transfer or assign the Wiley Materials on a stand-alone basis, or any of the rights granted to you hereunder to any other person.

- The Wiley Materials and all of the intellectual property rights therein shall at all times remain the exclusive property of John Wiley & Sons Inc, the Wiley Companies, or their respective licensors, and your interest therein is only that of having possession of and the right to reproduce the Wiley Materials pursuant to Section 2 herein during the continuance of this Agreement. You agree that you own no right, title or interest in or to the Wiley Materials or any of the intellectual property rights therein. You shall have no rights hereunder other than the license as provided for above in Section 2. No right, license or interest to any trademark, trade name, service mark or other branding ("Marks") of WILEY or its licensors is granted hereunder, and you agree that you shall not assert any such right, license or interest with respect thereto

- NEITHER WILEY NOR ITS LICENSORS MAKES ANY WARRANTY OR REPRESENTATION OF ANY KIND TO YOU OR ANY THIRD PARTY, EXPRESS, IMPLIED OR STATUTORY, WITH RESPECT TO THE MATERIALS OR THE ACCURACY OF ANY INFORMATION CONTAINED IN THE MATERIALS, INCLUDING, WITHOUT LIMITATION, ANY IMPLIED WARRANTY OF MERCHANTABILITY, ACCURACY, SATISFACTORY QUALITY, FITNESS FOR A PARTICULAR PURPOSE, USABILITY, INTEGRATION OR NON-INFRINGEMENT AND ALL SUCH WARRANTIES ARE HEREBY EXCLUDED BY WILEY AND ITS LICENSORS AND WAIVED BY YOU.

- WILEY shall have the right to terminate this Agreement immediately upon breach of this Agreement by you.

- You shall indemnify, defend and hold harmless WILEY, its Licensors and their respective directors, officers, agents and employees, from and against any actual or threatened claims, demands, causes of action or proceedings arising from any breach of this Agreement by you.

- IN NO EVENT SHALL WILEY OR ITS LICENSORS BE LIABLE TO YOU OR ANY OTHER PARTY OR ANY OTHER PERSON OR ENTITY FOR ANY SPECIAL, CONSEQUENTIAL, INCIDENTAL, INDIRECT, EXEMPLARY OR PUNITIVE DAMAGES, HOWEVER CAUSED, ARISING OUT OF OR IN CONNECTION WITH THE DOWNLOADING, PROVISIONING, VIEWING OR USE OF THE MATERIALS REGARDLESS OF THE FORM OF ACTION, WHETHER FOR BREACH OF CONTRACT, BREACH OF WARRANTY, TORT, NEGLIGENCE, INFRINGEMENT OR OTHERWISE (INCLUDING, WITHOUT LIMITATION, DAMAGES BASED ON LOSS OF PROFITS, DATA, FILES, USE, BUSINESS OPPORTUNITY OR CLAIMS OF THIRD PARTIES), AND WHETHER OR NOT THE PARTY HAS BEEN ADVISED OF THE POSSIBILITY OF SUCH DAMAGES. THIS LIMITATION SHALL APPLY NOTWITHSTANDING ANY FAILURE OF ESSENTIAL PURPOSE OF ANY LIMITED REMEDY PROVIDED HEREIN.

- Should any provision of this Agreement be held by a court of competent jurisdiction to be illegal, invalid, or unenforceable, that provision shall be deemed amended to achieve as nearly as possible the same economic effect as the original provision, and the legality, validity and enforceability of the remaining provisions of this Agreement shall not be affected or impaired thereby.

- The failure of either party to enforce any term or condition of this Agreement shall not constitute a waiver of either party's right to enforce each and every term and condition of this Agreement. No breach under this agreement shall be deemed waived or excused by either party unless such waiver or consent is in writing signed by the party granting such waiver or consent. The waiver by or consent of a party to a breach of any provision of this Agreement shall not operate or be construed as a waiver of or consent to any other or subsequent breach by such other party.

- This Agreement may not be assigned (including by operation of law or otherwise) by you without WILEY's prior written consent.

- Any fee required for this permission shall be non-refundable after thirty (30) days from receipt by the CCC.

- These terms and conditions together with CCC's Billing and Payment terms and conditions (which are incorporated herein) form the entire agreement between you and WILEY concerning this licensing transaction and (in the absence of fraud) supersedes all prior agreements and representations of the parties, oral or written. This Agreement may not be amended except in writing signed by both parties. This Agreement shall be binding upon and inure to the benefit of the parties' successors, legal representatives, and authorized assigns.

- In the event of any conflict between your obligations established by these terms and conditions and those established by CCC's Billing and Payment terms and conditions, these terms and conditions shall prevail.

- WILEY expressly reserves all rights not specifically granted in the combination of (i) the license details provided by you and accepted in the course of this licensing transaction, (ii) these terms and conditions and (iii) CCC's Billing and Payment terms and conditions.

- This Agreement will be void if the Type of Use, Format, Circulation, or Requestor Type was misrepresented during the licensing process.

- This Agreement shall be governed by and construed in accordance with the laws of the State of New York, USA, without regards to such state's conflict of law rules. Any legal action, suit or proceeding arising out of or relating to these Terms and Conditions or the breach thereof shall be instituted in a court of competent jurisdiction in New York County in the State of New York in the United States of America and each party hereby consents and submits to the personal jurisdiction of such court, waives any objection to venue in such court and consents to service of process by registered or certified mail, return receipt requested, at the last known address of such party.

136

Further details can be found on Wiley Online Library
http://olabout.wiley.com/WileyCDA/Section/id-410895.html

Other Terms and Conditions:

v1.10 Last updated September 2015

Questions? customercare@copyright.com **or +1-855-239-3415 (toll free in the US) or +1-978-646-2777.**

B.2 Permission to reproduce Chapter 2

Copyright Clearance Center

RightsLink®

Home | Create Account | Help

Title: Evaluation of unified intensity-modulated arc therapy for the radiotherapy of head-and-neck cancer

Author: Michael MacFarlane,Douglas A. Hoover,Eugene Wong,Nancy Read,David Palma,Varagur Venkatesan,Alex Hammond,Jerry J. Battista,Jeff Z. Chen

Publication: Radiotherapy and Oncology

Publisher: Elsevier

Date: May 2016

© 2016 Elsevier Ireland Ltd. All rights reserved.

BACK | CLOSE WINDOW

B.3 Permission to reproduce Chapter 3

Clearance Center Inc., ("CCC's Billing and Payment terms and conditions"), at the time that you opened your RightsLink account (these are available at any time at http://myaccount.copyright.com).

Terms and Conditions

- The materials you have requested permission to reproduce or reuse (the "Wiley Materials") are protected by copyright.

- You are hereby granted a personal, non-exclusive, non-sub licensable (on a stand-alone basis), non-transferable, worldwide, limited license to reproduce the Wiley Materials for the purpose specified in the licensing process. This license, **and any CONTENT (PDF or image file) purchased as part of your order,** is for a one-time use only and limited to any maximum distribution number specified in the license. The first instance of republication or reuse granted by this license must be completed within two years of the date of the grant of this license (although copies prepared before the end date may be distributed thereafter). The Wiley Materials shall not be used in any other manner or for any other purpose, beyond what is granted in the license. Permission is granted subject to an appropriate acknowledgement given to the author, title of the material/book/journal and the publisher. You shall also duplicate the copyright notice that appears in the Wiley publication in your use of the Wiley Material. Permission is also granted on the understanding that nowhere in the text is a previously published source acknowledged for all or part of this Wiley Material. Any third party content is expressly excluded from this permission.

- With respect to the Wiley Materials, all rights are reserved. Except as expressly granted by the terms of the license, no part of the Wiley Materials may be copied, modified, adapted (except for minor reformatting required by the new Publication), translated, reproduced, transferred or distributed, in any form or by any means, and no derivative works may be made based on the Wiley Materials without the prior permission of the respective copyright owner.**For STM Signatory Publishers clearing permission under the terms of the STM Permissions Guidelines only, the terms of the license are extended to include subsequent editions and for editions in other languages, provided such editions are for the work as a whole in situ and does not involve the separate exploitation of the permitted figures or extracts,** You may not alter, remove or suppress in any manner any copyright, trademark or other notices displayed by the Wiley Materials. You may not license, rent, sell, loan, lease, pledge, offer as security, transfer or assign the Wiley Materials on a stand-alone basis, or any of the rights granted to you hereunder to any other person.

- The Wiley Materials and all of the intellectual property rights therein shall at all times remain the exclusive property of John Wiley & Sons Inc, the Wiley Companies, or their respective licensors, and your interest therein is only that of having possession of and the right to reproduce the Wiley Materials pursuant to Section 2 herein during the continuance of this Agreement. You agree that you own no right, title or interest in or to the Wiley Materials or any of the intellectual property rights therein. You shall have no rights hereunder other than the license as provided for above in Section 2. No right, license or interest to any trademark, trade name, service mark or other branding ("Marks") of WILEY or its licensors is granted hereunder, and you agree that you shall not assert any such right, license or interest with respect thereto

- NEITHER WILEY NOR ITS LICENSORS MAKES ANY WARRANTY OR REPRESENTATION OF ANY KIND TO YOU OR ANY THIRD PARTY, EXPRESS, IMPLIED OR STATUTORY, WITH RESPECT TO THE MATERIALS

140

OR THE ACCURACY OF ANY INFORMATION CONTAINED IN THE MATERIALS, INCLUDING, WITHOUT LIMITATION, ANY IMPLIED WARRANTY OF MERCHANTABILITY, ACCURACY, SATISFACTORY QUALITY, FITNESS FOR A PARTICULAR PURPOSE, USABILITY, INTEGRATION OR NON-INFRINGEMENT AND ALL SUCH WARRANTIES ARE HEREBY EXCLUDED BY WILEY AND ITS LICENSORS AND WAIVED BY YOU.

- WILEY shall have the right to terminate this Agreement immediately upon breach of this Agreement by you.

- You shall indemnify, defend and hold harmless WILEY, its Licensors and their respective directors, officers, agents and employees, from and against any actual or threatened claims, demands, causes of action or proceedings arising from any breach of this Agreement by you.

- IN NO EVENT SHALL WILEY OR ITS LICENSORS BE LIABLE TO YOU OR ANY OTHER PARTY OR ANY OTHER PERSON OR ENTITY FOR ANY SPECIAL, CONSEQUENTIAL, INCIDENTAL, INDIRECT, EXEMPLARY OR PUNITIVE DAMAGES, HOWEVER CAUSED, ARISING OUT OF OR IN CONNECTION WITH THE DOWNLOADING, PROVISIONING, VIEWING OR USE OF THE MATERIALS REGARDLESS OF THE FORM OF ACTION, WHETHER FOR BREACH OF CONTRACT, BREACH OF WARRANTY, TORT, NEGLIGENCE, INFRINGEMENT OR OTHERWISE (INCLUDING, WITHOUT LIMITATION, DAMAGES BASED ON LOSS OF PROFITS, DATA, FILES, USE, BUSINESS OPPORTUNITY OR CLAIMS OF THIRD PARTIES), AND WHETHER OR NOT THE PARTY HAS BEEN ADVISED OF THE POSSIBILITY OF SUCH DAMAGES. THIS LIMITATION SHALL APPLY NOTWITHSTANDING ANY FAILURE OF ESSENTIAL PURPOSE OF ANY LIMITED REMEDY PROVIDED HEREIN.

- Should any provision of this Agreement be held by a court of competent jurisdiction to be illegal, invalid, or unenforceable, that provision shall be deemed amended to achieve as nearly as possible the same economic effect as the original provision, and the legality, validity and enforceability of the remaining provisions of this Agreement shall not be affected or impaired thereby.

- The failure of either party to enforce any term or condition of this Agreement shall not constitute a waiver of either party's right to enforce each and every term and condition of this Agreement. No breach under this agreement shall be deemed waived or excused by either party unless such waiver or consent is in writing signed by the party granting such waiver or consent. The waiver by or consent of a party to a breach of any provision of this Agreement shall not operate or be construed as a waiver of or consent to any other or subsequent breach by such other party.

- This Agreement may not be assigned (including by operation of law or otherwise) by you without WILEY's prior written consent.

- Any fee required for this permission shall be non-refundable after thirty (30) days from receipt by the CCC.

- These terms and conditions together with CCC's Billing and Payment terms and conditions (which are incorporated herein) form the entire agreement between you and WILEY concerning this licensing transaction and (in the absence of fraud) supersedes

all prior agreements and representations of the parties, oral or written. This Agreement may not be amended except in writing signed by both parties. This Agreement shall be binding upon and inure to the benefit of the parties' successors, legal representatives, and authorized assigns.

- In the event of any conflict between your obligations established by these terms and conditions and those established by CCC's Billing and Payment terms and conditions, these terms and conditions shall prevail.

- WILEY expressly reserves all rights not specifically granted in the combination of (i) the license details provided by you and accepted in the course of this licensing transaction, (ii) these terms and conditions and (iii) CCC's Billing and Payment terms and conditions.

- This Agreement will be void if the Type of Use, Format, Circulation, or Requestor Type was misrepresented during the licensing process.

- This Agreement shall be governed by and construed in accordance with the laws of the State of New York, USA, without regards to such state's conflict of law rules. Any legal action, suit or proceeding arising out of or relating to these Terms and Conditions or the breach thereof shall be instituted in a court of competent jurisdiction in New York County in the State of New York in the United States of America and each party hereby consents and submits to the personal jurisdiction of such court, waives any objection to venue in such court and consents to service of process by registered or certified mail, return receipt requested, at the last known address of such party.

142

Other Terms and Conditions:

v1.10 Last updated September 2015

Questions? customercare@copyright.com or +1-855-239-3415 (toll free in the US) or +1-978-646-2777.

B.4 Permission to reproduce Chapter 5

Copyright Clearance Center   **RightsLink®**   Home   Create Account   Help

WILEY

Title:	Patient-specific calibration of cone-beam computed tomography data sets for radiotherapy dose calculations and treatment plan assessment
Author:	Michael MacFarlane, Daniel Wong, Douglas A. Hoover, et al
Publication:	Journal of Applied Clinical Medical Physics
Publisher:	John Wiley and Sons
Date:	Feb 26, 2018

Copyright © 2018, John Wiley and Sons

Welcome to RightsLink

Wiley offers a professional reprint service for high quality reproduction of articles from over 1400 scientific and medical journals. Wiley's reprint service offers:

- Peer reviewed research or reviews
- Tailored collections of articles
- A professional high quality finish
- Glossy journal style color covers
- Company or brand customisation
- Language translations
- Prompt turnaround times and delivery directly to your office, warehouse or congress.

Please contact our Reprints department for a quotation. Email corporatesaleseurope@wiley.com or corporatesalesusa@wiley.com or corporatesalesDE@wiley.com .

CLOSE WINDOW

B.5 Permission to reproduce Appendix A

JOHN WILEY AND SONS LICENSE
TERMS AND CONDITIONS

Feb 04, 2019

This Agreement between Michael MacFarlane ("You") and John Wiley and Sons ("John Wiley and Sons") consists of your license details and the terms and conditions provided by John Wiley and Sons and Copyright Clearance Center.

License Number	4521921402521
License date	Feb 04, 2019
Licensed Content Publisher	John Wiley and Sons
Licensed Content Publication	Medical Physics
Licensed Content Title	Feasibility of a unified approach to intensity-modulated radiation therapy and volume-modulated arc therapy optimization and delivery
Licensed Content Author	Douglas A. Hoover, Michael MacFarlane, Eugene Wong, et al
Licensed Content Date	Jan 14, 2015
Licensed Content Volume	42
Licensed Content Issue	2
Licensed Content Pages	9
Type of use	Dissertation/Thesis
Requestor type	Author of this Wiley article
Format	Electronic
Portion	Full article
Will you be translating?	No
Title of your thesis / dissertation	Improving the Plan Quality, Plan Delivery, and Planning Efficiency of External Beam Radiotherapy
Expected completion date	May 2019
Expected size (number of pages)	200
Requestor Location	Michael MacFarlane
Publisher Tax ID	EU826007151
Total	0.00 USD
Terms and Conditions	

TERMS AND CONDITIONS

This copyrighted material is owned by or exclusively licensed to John Wiley & Sons, Inc. or one of its group companies (each a"Wiley Company") or handled on behalf of a society with which a Wiley Company has exclusive publishing rights in relation to a particular work (collectively "WILEY"). By clicking "accept" in connection with completing this licensing transaction, you agree that the following terms and conditions apply to this transaction

(along with the billing and payment terms and conditions established by the Copyright Clearance Center Inc., ("CCC's Billing and Payment terms and conditions"), at the time that you opened your RightsLink account (these are available at any time at http://myaccount.copyright.com).

Terms and Conditions

- The materials you have requested permission to reproduce or reuse (the "Wiley Materials") are protected by copyright.

- You are hereby granted a personal, non-exclusive, non-sub licensable (on a stand-alone basis), non-transferable, worldwide, limited license to reproduce the Wiley Materials for the purpose specified in the licensing process. This license, **and any CONTENT (PDF or image file) purchased as part of your order,** is for a one-time use only and limited to any maximum distribution number specified in the license. The first instance of republication or reuse granted by this license must be completed within two years of the date of the grant of this license (although copies prepared before the end date may be distributed thereafter). The Wiley Materials shall not be used in any other manner or for any other purpose, beyond what is granted in the license. Permission is granted subject to an appropriate acknowledgement given to the author, title of the material/book/journal and the publisher. You shall also duplicate the copyright notice that appears in the Wiley publication in your use of the Wiley Material. Permission is also granted on the understanding that nowhere in the text is a previously published source acknowledged for all or part of this Wiley Material. Any third party content is expressly excluded from this permission.

- With respect to the Wiley Materials, all rights are reserved. Except as expressly granted by the terms of the license, no part of the Wiley Materials may be copied, modified, adapted (except for minor reformatting required by the new Publication), translated, reproduced, transferred or distributed, in any form or by any means, and no derivative works may be made based on the Wiley Materials without the prior permission of the respective copyright owner.**For STM Signatory Publishers clearing permission under the terms of the STM Permissions Guidelines only, the terms of the license are extended to include subsequent editions and for editions in other languages, provided such editions are for the work as a whole in situ and does not involve the separate exploitation of the permitted figures or extracts,** You may not alter, remove or suppress in any manner any copyright, trademark or other notices displayed by the Wiley Materials. You may not license, rent, sell, loan, lease, pledge, offer as security, transfer or assign the Wiley Materials on a stand-alone basis, or any of the rights granted to you hereunder to any other person.

- The Wiley Materials and all of the intellectual property rights therein shall at all times remain the exclusive property of John Wiley & Sons Inc, the Wiley Companies, or their respective licensors, and your interest therein is only that of having possession of and the right to reproduce the Wiley Materials pursuant to Section 2 herein during the continuance of this Agreement. You agree that you own no right, title or interest in or to the Wiley Materials or any of the intellectual property rights therein. You shall have no rights hereunder other than the license as provided for above in Section 2. No right, license or interest to any trademark, trade name, service mark or other branding ("Marks") of WILEY or its licensors is granted hereunder, and you agree that you shall not assert any such right, license or interest with respect thereto

- NEITHER WILEY NOR ITS LICENSORS MAKES ANY WARRANTY OR REPRESENTATION OF ANY KIND TO YOU OR ANY THIRD PARTY,

EXPRESS, IMPLIED OR STATUTORY, WITH RESPECT TO THE MATERIALS OR THE ACCURACY OF ANY INFORMATION CONTAINED IN THE MATERIALS, INCLUDING, WITHOUT LIMITATION, ANY IMPLIED WARRANTY OF MERCHANTABILITY, ACCURACY, SATISFACTORY QUALITY, FITNESS FOR A PARTICULAR PURPOSE, USABILITY, INTEGRATION OR NON-INFRINGEMENT AND ALL SUCH WARRANTIES ARE HEREBY EXCLUDED BY WILEY AND ITS LICENSORS AND WAIVED BY YOU.

- WILEY shall have the right to terminate this Agreement immediately upon breach of this Agreement by you.

- You shall indemnify, defend and hold harmless WILEY, its Licensors and their respective directors, officers, agents and employees, from and against any actual or threatened claims, demands, causes of action or proceedings arising from any breach of this Agreement by you.

- IN NO EVENT SHALL WILEY OR ITS LICENSORS BE LIABLE TO YOU OR ANY OTHER PARTY OR ANY OTHER PERSON OR ENTITY FOR ANY SPECIAL, CONSEQUENTIAL, INCIDENTAL, INDIRECT, EXEMPLARY OR PUNITIVE DAMAGES, HOWEVER CAUSED, ARISING OUT OF OR IN CONNECTION WITH THE DOWNLOADING, PROVISIONING, VIEWING OR USE OF THE MATERIALS REGARDLESS OF THE FORM OF ACTION, WHETHER FOR BREACH OF CONTRACT, BREACH OF WARRANTY, TORT, NEGLIGENCE, INFRINGEMENT OR OTHERWISE (INCLUDING, WITHOUT LIMITATION, DAMAGES BASED ON LOSS OF PROFITS, DATA, FILES, USE, BUSINESS OPPORTUNITY OR CLAIMS OF THIRD PARTIES), AND WHETHER OR NOT THE PARTY HAS BEEN ADVISED OF THE POSSIBILITY OF SUCH DAMAGES. THIS LIMITATION SHALL APPLY NOTWITHSTANDING ANY FAILURE OF ESSENTIAL PURPOSE OF ANY LIMITED REMEDY PROVIDED HEREIN.

- Should any provision of this Agreement be held by a court of competent jurisdiction to be illegal, invalid, or unenforceable, that provision shall be deemed amended to achieve as nearly as possible the same economic effect as the original provision, and the legality, validity and enforceability of the remaining provisions of this Agreement shall not be affected or impaired thereby.

- The failure of either party to enforce any term or condition of this Agreement shall not constitute a waiver of either party's right to enforce each and every term and condition of this Agreement. No breach under this agreement shall be deemed waived or excused by either party unless such waiver or consent is in writing signed by the party granting such waiver or consent. The waiver by or consent of a party to a breach of any provision of this Agreement shall not operate or be construed as a waiver of or consent to any other or subsequent breach by such other party.

- This Agreement may not be assigned (including by operation of law or otherwise) by you without WILEY's prior written consent.

- Any fee required for this permission shall be non-refundable after thirty (30) days from receipt by the CCC.

- These terms and conditions together with CCC's Billing and Payment terms and conditions (which are incorporated herein) form the entire agreement between you and

147

WILEY concerning this licensing transaction and (in the absence of fraud) supersedes all prior agreements and representations of the parties, oral or written. This Agreement may not be amended except in writing signed by both parties. This Agreement shall be binding upon and inure to the benefit of the parties' successors, legal representatives, and authorized assigns.

- In the event of any conflict between your obligations established by these terms and conditions and those established by CCC's Billing and Payment terms and conditions, these terms and conditions shall prevail.

- WILEY expressly reserves all rights not specifically granted in the combination of (i) the license details provided by you and accepted in the course of this licensing transaction, (ii) these terms and conditions and (iii) CCC's Billing and Payment terms and conditions.

- This Agreement will be void if the Type of Use, Format, Circulation, or Requestor Type was misrepresented during the licensing process.

- This Agreement shall be governed by and construed in accordance with the laws of the State of New York, USA, without regards to such state's conflict of law rules. Any legal action, suit or proceeding arising out of or relating to these Terms and Conditions or the breach thereof shall be instituted in a court of competent jurisdiction in New York County in the State of New York in the United States of America and each party hereby consents and submits to the personal jurisdiction of such court, waives any objection to venue in such court and consents to service of process by registered or certified mail, return receipt requested, at the last known address of such party.

Other Terms and Conditions:

v1.10 Last updated September 2015

149

Appendix C – Supplemental Data for Chapter 2

This content of this appendix was previously published with the article "Evaluation of unified intensity-modulated arc therapy for the radiotherapy of head-and-neck cancer" by Michael MacFarlane, Douglas A. Hoover, Eugene Wong, Nancy Read, David Palma, Varagur Venkatesan, Alex Hammond, Jerry J. Battista, and Jeff Z. Chen, Radiotherapy and Oncology, 119 (2): 331-336 (2016). Permission to reproduce this article was granted by Elsevier and is provided in Appendix B.2.
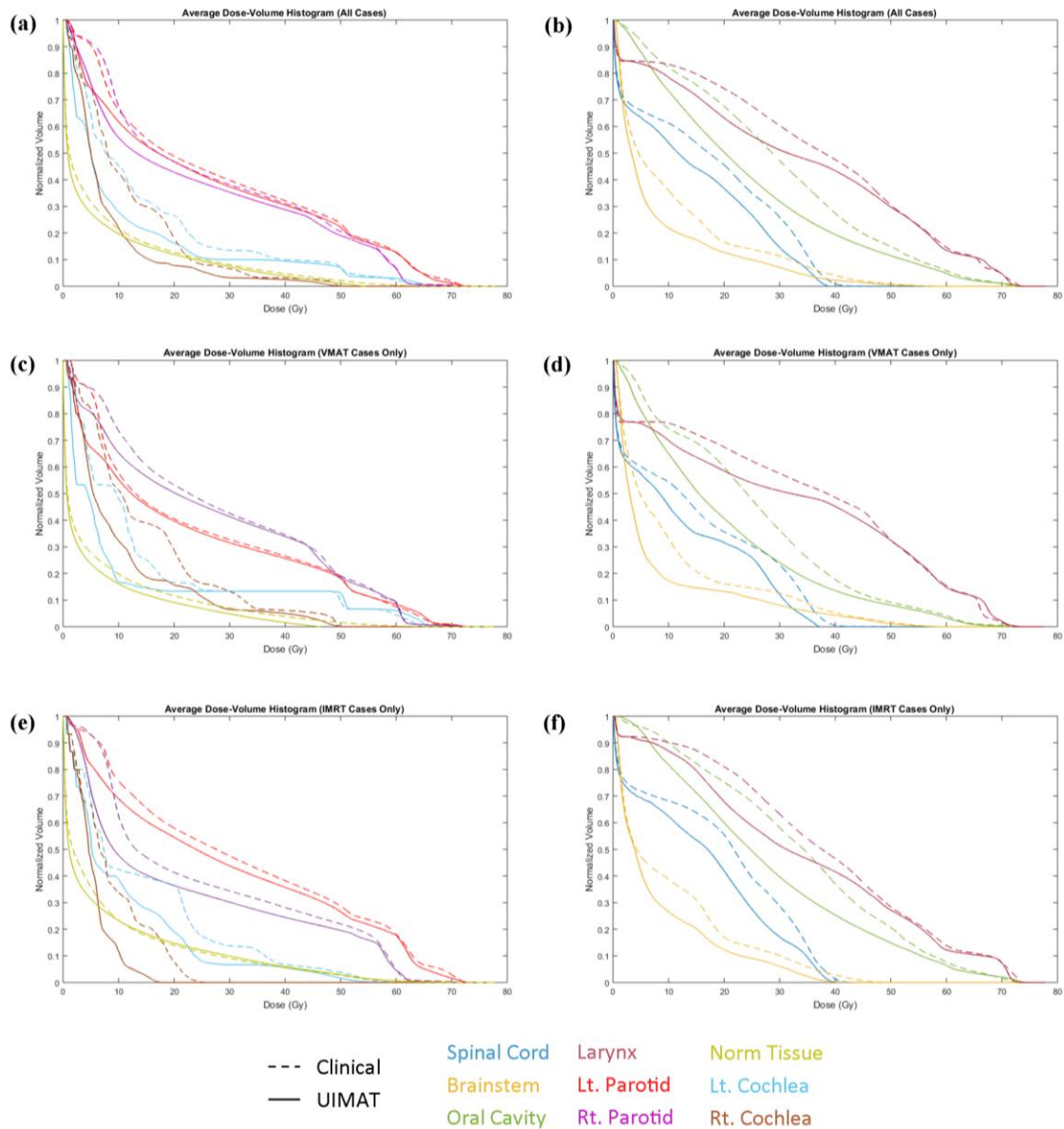
Supplemental Figure 2.1: OAR dose-volume histograms averaged over: a) & b) all cases; c) & d) VMAT cases only; e) & f) IMRT cases only.

Supplementary Table 2.1: Summary of UIMAT and clinically delivered treatment plans. Patients with several prescriptions had multiple target volumes, each with the listed dose levels.

Patient	Site	Dose Prescription [Gy]	Beam Arrangement Clinical	Beam Arrangement UIMAT	Delivery Time [s] Clinical	Delivery Time [s] UIMAT	IMRT QA [%] Clinical	IMRT QA [%] UIMAT
1	Right Parotid	64/60/54	2 - 210° Arcs	1 - 360° Arc	115	145	99.4	97.5
2	Right Parotid	60	2 - 225° Arcs	1 - 230° Arc	121	161	99.3	99.5
3	Neck/Parotids	70/56	2 - 360° Arcs	1 - 360° Arc	194	180	98.5	97.6
4	Larynx/Neck	70/56	2 - 360° Arcs	1 - 360° Arc	177	176	94.4	96.9
5	Right Parotid	50	2 - 180° Arcs	1 - 190° Arc	92	135	98.3	98.7
6	Left Neck	66/64/60/54	2 - 360° Arcs	1 - 360° Arc	182	131	99.6	98.5
7	Whole Neck	70/56	2 - 360° Arcs	1 - 360° Arc	174	198	96.0	96.1
8	Left Parotid	50	2 - 180° Arcs	1 - 180° Arc	109	81	99.4	97.5
9	Hypopharynx	66/60/56	2 - 360° Arc	1 - 360° Arc	166	125	99.3	98.0
10	Right Neck	54	2 - 360° Arcs	1 - 360° Arc	171	159	97.2	96.6
11	Left Neck	50	2 - 210° Arcs	1 - 190° Arc	120	154	99.6	97.4
12	Right Neck	72/65	2 - 360° Arcs	1 - 210° Arc	168	82	98.3	97.8
13	Right Neck	55/45	2 - 180° Arcs	1 - 210° Arc	101	135	100.0	98.0
14	Oral Cavity	66/64/60/54	2 - 360° Arcs	1 - 360° Arc	174	97	97.7	96.0
15	Larynx/Neck	70/56	2 - 360° Arcs	1 - 360° Arc	168	123	98.8	97.2
16	Left Neck	64/60	4F SS-IMRT	1 - 190° Arc	188	108	99.8	97.9
17	Left Head	64/60/54	4F SS-IMRT	1 - 190° Arc	204	144	98.0	97.8
18	Ethmoid	70/63/56	4F SS-IMRT	1 - 210° Arc	127	109	99.6	97.2
19	Left Parotid	50	4F SS-IMRT	1 - 210° Arc	224	167	99.3	97.8
20	Right Neck	50/45	5F SS-IMRT	1 - 230° Arc	269	182	99.3	98.9
21	Right Neck	70/56	5F SS-IMRT	1 - 240° Arc	313	94	99.8	96.7
22	Left Neck	60/54	6F SS-IMRT	1 - 360° Arc	339	136	99.2	97.6
23	Hypopharynx	70/63/56	6F SS-IMRT	1 - 360° Arc	320	214	98.9	95.1
24	Hypopharynx	70/56	6F SS-IMRT	1 - 360° Arc	348	147	98.4	95.7
25	Larynx/Neck	70/63/56	6F SS-IMRT	1 - 360° Arc	287	111	97.9	99.6
26	Right Neck	50/45	4F SS-IMRT	1 - 360° Arc	235	148	98.0	97.9
27	Hypopharynx	60/54	6F SS-IMRT	1 - 360° Arc	358	192	93.4	94.7
28	Left Neck	64/60/54	4F SS-IMRT	1 - 360° Arc	262	202	99.4	97.5
29	Tonsils	70/63/56	6F SS-IMRT	1 - 360° Arc	296	117	97.6	98.3
30	Right Neck	60/54	4F SS-IMRT	1 - 360° Arc	244	154	99.4	96.4

Abbreviations: UIMAT, unified intensity-modulated arc therapy; nF SS-IMRT, n-field step-and-shoot intensity-modulated radiation therapy.

Supplementary Table 2.2: Comparison of dose metrics between the unified plans and the clinically delivered VMAT plans. PTV mean doses and D95 (dose to 95% of the volume) are given as percentages of the prescribed dose to the target volume(s). Max doses are defined as the dose to 2% of the volume. Missing dose metrics are a result of OARs which were not contoured, for example due to an OAR being completely enclosed within the PTV.

No.	Plan	Planning Target Volume(s) Conformity Index	Mean (%)	D95 (%)	Oral Cavity Mean (Gy)	Left Parotid Mean (Gy)	Right Parotid Mean (Gy)	Larynx Mean (Gy)	Cord Max (Gy)	Brainstem Max (Gy)	Left Cochlea Max (Gy)	Right Cochlea Max (Gy)
1	VMAT	0.21/0.77/0.63	99/101/103	97/97/97	28.3	6.9	-	33.8	20.4	14.0	6.2	25.3
	Unified	0.16/0.80/0.63	101/102/104	99/97/98	15.6	2.0	-	26.2	13.5	6.0	2.1	17.6
2	VMAT	0.87	101	98	30.0	5.9	60.9	27.9	31.9	11.1	5.6	27.6
	Unified	0.86	101	97	23.1	2.6	60.8	22.2	23.4	5.1	1.6	10.6
3	VMAT	0.78/0.71	101/105	99/98	39.5	25.3	25.5	48.7	37.0	40.4	27.3	32.4
	Unified	0.74/0.66	101/106	99/99	35.0	22.6	22.6	45.5	32.4	31.4	13.5	26.3
4	VMAT	0.83/0.79	100/102	98/97	33.2	25.9	25.6	-	35.8	25.7	3.8	2.9
	Unified	0.82/0.78	101/103	99/99	21.3	26.1	24.6	-	29.4	11.0	4.0	2.3
5	VMAT	0.74	101	98	5.8	2.0	-	0.4	16.5	20.3	2.3	50.0
	Unified	0.76	102	99	5.0	2.6	-	0.4	9.2	11.7	2.5	50.0
6	VMAT	0.19/0.44/0.77/0.67	102/102/102/103	99/99/98/99	39.5	39.9	30.6	50.5	39.8	42.3	25.2	19.8
	Unified	0.15/0.37/0.73/0.65	101/102/103/103	99/99/97/99	35.8	39.8	30.8	52.2	35.1	39.8	19.5	20.0
7	VMAT	0.84/0.75	101/106	98/98	30.5	29.7	30.4	64.7	37.0	35.0	19.0	9.8
	Unified	0.85/0.75	102/107	98/98	22.7	31.0	32.1	65.2	31.2	24.6	9.6	4.6
8	VMAT	0.72	102	99	5.2	43.9	1.3	0.2	7.3	6.2	17.1	1.2
	Unified	0.68	104	99	3.6	44.3	1.1	0.2	5.6	2.8	9.4	1.0
9	VMAT	0.75/0.55/0.72	100/103/107	97/99/98	37.7	37.3	32.9	65.8	37.5	39.6	11.9	12.2
	Unified	0.74/0.54/0.71	101/105/106	97/101/97	35.7	34.0	29.5	66.7	36.7	31.0	7.3	7.5
10	VMAT	0.92	101	97	4.7	6.6	20.3	0.7	41.6	40.5	4.3	7.9
	Unified	0.87	101	97	3.0	4.2	16.1	1.0	36.8	32.4	1.8	6.2
11	VMAT	0.80	101	98	18.1	-	7.8	31.0	18.3	21.5	50.8	8.2
	Unified	0.79	101	98	14.8	-	2.2	24.1	14.3	7.5	51.6	2.0

No.	Plan	Planning Target Volume(s) Conformity Index	Mean (%)	D95 (%)	Oral Cavity Mean (Gy)	Left Parotid Mean (Gy)	Right Parotid Mean (Gy)	Larynx Mean (Gy)	Cord Max (Gy)	Brainstem Max (Gy)	Left Cochlea Max (Gy)	Right Cochlea Max (Gy)
12	VMAT	0.52/0.83	101/101	97/96	22.6	4.7	-	36.1	19.7	18.6	5.2	25.0
	Unified	0.45/0.85	101/102	98/96	10.2	2.8	-	28.0	14.5	7.9	1.6	12.1
13	VMAT	0.68/0.73	100/109	96/105	8.9	-	46.4	27.8	25.0	4.3	3.1	12.3
	Unified	0.58/0.66	101/110	97/98	8.0	-	46.5	24.1	20.1	4.4	3.1	6.9
14	VMAT	0.42/0.26/0.71/0.65	100/101/102/103	90/99/97/98	44.0	33.4	28.8	55.0	40.2	57.3	64.6	35.0
	Unified	0.27/0.24/0.68/0.66	100/102/103/103	89/99/96/96	43.0	33.2	26.3	55.5	37.7	56.9	65.5	29.5
15	VMAT	0.74/0.73	103/105	101/100	29.2	24.3	25.0	-	37.9	37.1	13.8	16.1
	Unified	0.71/0.70	103/107	100/100	22.7	19.5	20.0	-	32.9	29.7	5.9	8.2
Med.	VMAT	0.73	101.5	98.0	29.2	25.3	27.2	33.8	35.8	25.7	11.9	16.1
	Unified	0.70	102.3	98.2	21.3	22.6	25.5	26.2	29.4	11.7	5.9	8.2
	P-value	0.003	0.001	0.695	0.002	0.173	0.071	0.173	0.001	0.001	0.011	0.001

*Abbreviations: D95, dose to 95% of the volume; VMAT, volumetric modulated arc therapy; Med, Median.

[†] P-values were calculated using the Wilcoxon signed-rank test.

Supplemental Table 2.3: Comparison of dose metrics between the unified plans and the clinically delivered IMRT plans. PTV mean doses and D95 (dose to 95% of the volume) are given as percentages of the prescribed dose to the target volume(s). Max doses are defined as the dose to 2% of the volume. Missing dose metrics are a result of OARs which were not contoured, for example due to an OAR being completely enclosed within the PTV.

No.	Plan	Planning Target Volume(s) Conformity Index	Mean (%)	D95 (%)	Oral Cavity Mean (Gy)	Left Parotid Mean (Gy)	Right Parotid Mean (Gy)	Larynx Mean (Gy)	Cord Max (Gy)	Brainstem Max (Gy)	Left Cochlea Max (Gy)	Right Cochlea Max (Gy)
16	IMRT	0.19/0.11	101/102	96/96	33.9	-	10.2	41.0	40.4	32.1	29.9	5.0
	Unified	0.18/0.11	101/102	96/96	27.5	-	7.8	41.1	37.3	24.2	25.7	4.5
17	IMRT	0.17/0.67/0.60	100/102/102	96/97/97	20.5	-	9.9	32.0	33.9	22.2	40.2	13.4
	Unified	0.16/0.60/0.60	101/102/103	98/99/97	16.7	-	4.9	27.0	28.9	22.2	29.2	7.0
18	IMRT	0.76/0.63/0.54	100/102/112	95/98/103	34.1	28.0	6.3	0.6	34.6	44.0	59.9	25.2
	Unified	0.81/0.65/0.55	101/102/109	96/99/101	32.8	27.1	5.2	0.6	27.0	41.0	56.3	17.7
19	IMRT	0.81	101	95	14.0	-	7.9	24.8	30.9	20.7	23.8	8.2
	Unified	0.83	101	96	12.4	-	3.9	22.3	24.8	8.0	14.1	4.0
20	IMRT	0.81/0.59	101/102	97/99	16.2	8.0	-	34.6	27.6	18.9	8.5	22.9
	Unified	0.79/0.61	101/102	96/99	13.8	3.7	-	30.5	15.9	6.4	2.5	9.7
21	IMRT	0.85/0.63	101/105	95/99	29.5	-	58.0	40.0	25.3	14.6	1.5	24.3
	Unified	0.86/0.68	102/104	97/99	23.3	-	58.1	38.5	23.3	6.6	1.4	11.4
22	IMRT	0.70/0.68	101/103	97/97	41.0	28.3	25.0	55.2	37.1	36.5	13.6	13.8
	Unified	0.76/0.70	101/102	98/97	40.1	26.4	15.7	54.1	30.6	23.5	5.3	5.2
23	IMRT	0.71/0.67/0.53	100/103/104	95/95/97	51.3	33.0	30.2	71.3	41.5	45.0	7.2	9.8
	Unified	0.71/0.68/0.56	99/103/105	95/95/99	45.6	31.0	28.4	70.6	39.4	38.8	5.1	6.2
24	IMRT	0.84/0.60	100/106	95/98	46.0	52.0	39.4	-	40.9	46.9	6.1	6.8
	Unified	0.83/0.63	102/107	97/99	35.4	48.3	36.6	-	39.0	35.9	5.9	5.7
25	IMRT	0.82/0.66/0.71	100/102/105	95/98/96	37.4	25.2	29.4	-	40.5	25.4	8.1	17.5
	Unified	0.83/0.62/0.69	102/104/106	97/100/99	27.7	20.9	26.1	-	39.6	20.2	8.2	11.2
26	IMRT	0.71/0.64	102/105	99/98	39.0	42.7	8.6	37.4	25.3	19.9	26.3	2.0
	Unified	0.78/0.69	102/104	98/99	30.8	40.0	3.2	30.9	21.3	10.6	23.3	1.3

No.	Plan	Conformity Index	Planning Target Volume(s) Mean (%)	D95 (%)	Oral Cavity Mean (Gy)	Left Parotid Mean (Gy)	Right Parotid Mean (Gy)	Larynx Mean (Gy)	Cord Max (Gy)	Brainstem Max (Gy)	Left Cochlea Max (Gy)	Right Cochlea Max (Gy)
27	IMRT	0.74/0.61	99/103	95/97	33.2	29.9	30.7	25.3	38.0	34.4	4.8	3.3
	Unified	0.74/0.59	101/102	97/99	23.5	25.3	26.0	15.3	36.7	32.8	4.5	3.1
28	IMRT	0.54/0.61/0.56	100/101/101	96/97/96	27.7	-	4.7	39.6	34.5	23.5	2.2	0.9
	Unified	0.47/0.67/0.56	102/102/101	98/98/99	23.7	-	2.7	37.6	28.8	11.6	2.1	0.9
29	IMRT	0.76/0.58/0.57	101/106/103	97/101/98	61.3	37.8	29.6	58.1	39.6	46.6	32.8	9.5
	Unified	0.77/0.56/0.59	103/105/104	98/102/98	57.7	36.1	21.0	55.8	35.3	32.4	16.5	7.0
30	IMRT	0.75/0.59	100/102	96/98	23.1	3.4	58.6	30.3	35.3	3.4	0.7	2.4
	Unified	0.73/0.56	101/103	97/100	10.0	2.6	58.3	20.9	30.3	4.5	0.6	2.0
Med.	IMRT	0.67	101.8	96.7	33.9	29.1	27.2	37.4	35.3	25.4	8.5	9.5
	Unified	0.67	102.2	98.0	27.5	26.7	18.4	30.9	30.3	22.2	5.9	5.7
P-value		0.256	0.011	0.004	0.001	0.005	0.001	0.002	0.001	0.001	0.001	0.001

*Abbreviations: D95, dose to 95% of the volume; IMRT, intensity-modulated radiation therapy; Med, Median.

[†] P-values were calculated using the Wilcoxon signed-rank test.

Appendix D – Supplemental Data for Chapter 3

This content of this appendix was previously published with the article "A fast inverse direct aperture optimization algorithm for intensity-modulated radiation therapy" by Michael MacFarlane, Douglas Hoover, Eugene Wong, Pedro Goldman, Jerry J. Battista, and Jeff Z. Chen, *Medical Physics,* Early View (2019). Permission to reproduce this article was granted by John Wiley and Sons and is provided in Appendix B.3.
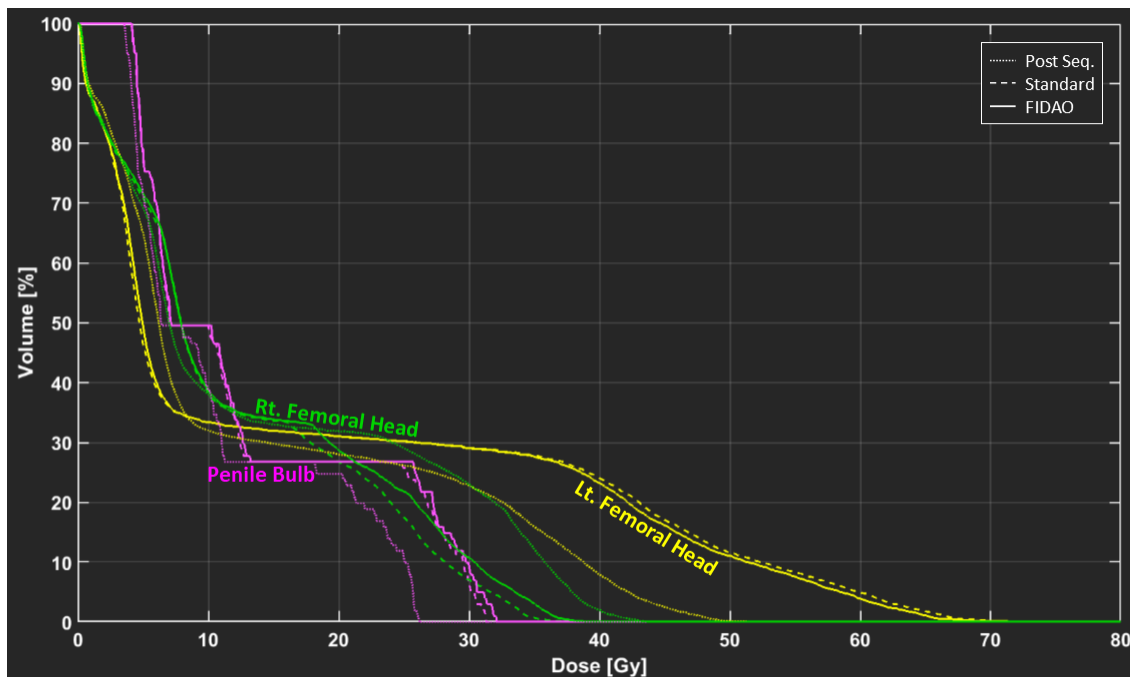
Supplemental Figure 3.1: Dose-volume histograms of the prostate case after undergoing FMO and aperture sequencing (dotted) and when optimized with the FIDAO (solid) and the standard (dashed) DAO algorithms.
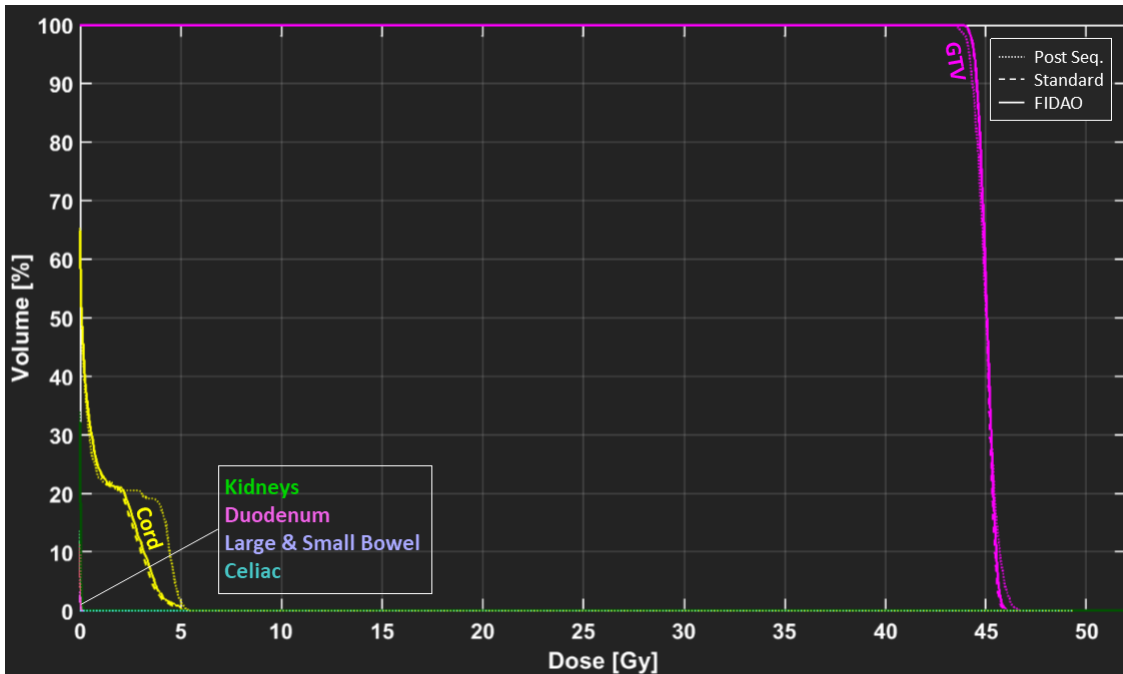
Supplemental Figure 3.2: Dose-volume histograms of the liver case after undergoing FMO and aperture sequencing (dotted) and when optimized with the FIDAO (solid) and the standard (dashed) DAO algorithms.
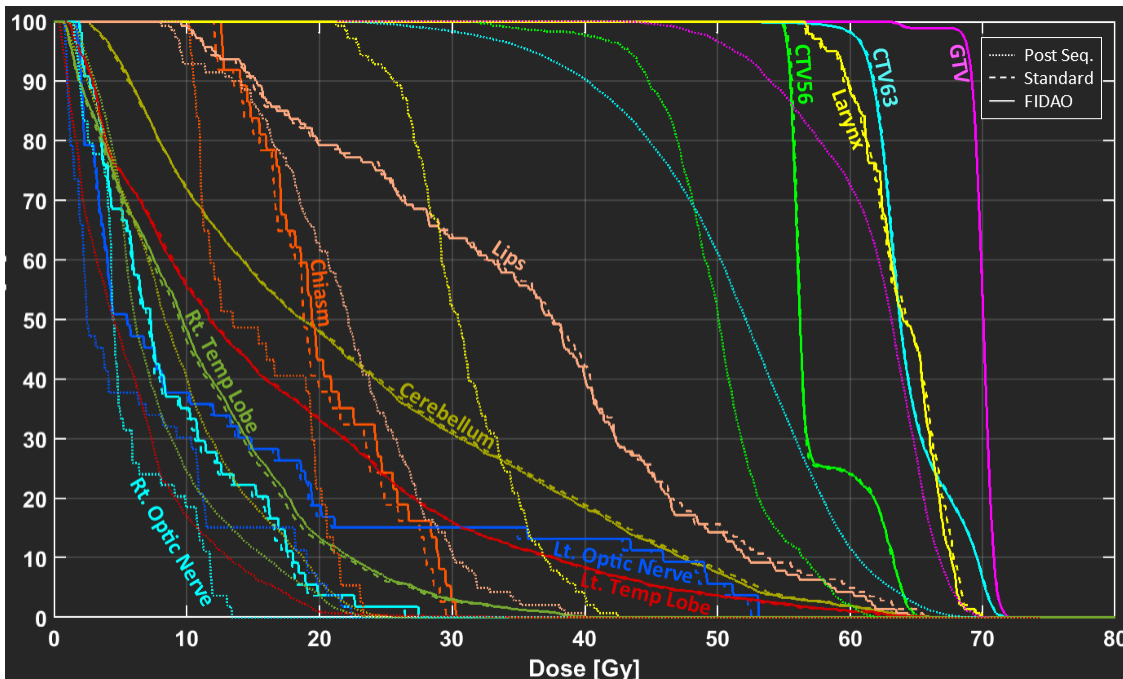
Supplemental Figure 3.3: Dose-volume histograms of the head-and-neck case after undergoing FMO and aperture sequencing (dotted) and when optimized with the FIDAO (solid) and the standard (dashed) DAO algorithms.

Supplemental Table 3.1: PTV dosimetric and volume statistics for each plan. Note that P.S. stands for the Post Sequencing plan. R50 is defined as the ratio of the 50% prescription isodose line to the PTV volume.

Case	PTV	No. Of Voxel	Volume [cc]	D98 [Gy] P.S.	Std.	FIDAO	D02 [Gy] P.S.	Std.	FIDAO	Conformity Index P.S.	Std.	FIDAO	Homogeneity Index P.S.	Std.	FIDAO	R50 P.S.	Std.	FIDAO
TG119	PTV50	7429	94.7	40.0	46.3	46.3	50.8	52.8	52.8	0.4	0.7	0.8	17.4	9.0	9.5	4.5	4.8	4.7
Prostate	PTV56	9491	1020.7	32.3	53.0	52.5	54.4	60.4	60.6	0.0	0.2	0.2	33.4	8.4	9.1	9.8	12.8	12.9
	PTV68	6770	259.6	50.2	64.0	64.2	68.0	69.7	69.9	0.3	0.6	0.6	20.9	6.1	6.1	6.7	10.0	10.1
Liver	PTV45	6954	156.5	38.7	43.2	43.4	46.2	46.1	46.2	0.8	0.7	0.8	11.4	4.1	4.2	3.2	5.4	5.4
Head-and-neck	PTV56	2104	94.7	38.5	54.9	54.8	53.4	57.1	57.3	0.0	0.0	0.0	20.1	2.9	3.2	18.5	40.5	40.5
	PTV63	22682	1020.7	26.4	59.1	58.8	60.9	67.5	67.4	0.0	0.5	0.5	44.4	9.7	9.9	1.5	3.5	3.5
	PTV70	5768	259.6	45.6	67.4	67.3	68.2	71.4	71.4	0.1	0.7	0.7	26.1	4.5	4.5	5.2	12.6	12.6

Supplemental Table 3.2: OAR dose statistics for each plan and structure.

		TG119		Prostate								Liver											
	OAR	Core	Body	Normal Tissue	Bladder	Lt. Femoral Head	Nodes	Penile Bulb	Rectum	Rt. Femoral Head	Prostate Bed	Celiac	Heart	Lt. Kidney	Rt. Kidney	Large Bowel	Liver	Skin	Small Bowel	Spinal Cord	Stomach	Duodenum	Normal Tissue
Mean [Gy]	P.S.	16.1	4.1	8.2	30.1	13.7	47	11.1	19.6	14.0	63.2	0.0	7.5	0.0	0.0	0.0	7.4	1.5	0.0	1.0	0.7	0.0	0.7
	Std.	12.7	3.9	10.1	32.9	17.4	57.3	13.0	34.7	12.0	68.0	0.0	2.5	0.0	0.0	0.0	4.4	1.2	0.0	0.8	0.8	0.0	0.7
	FIDAO	13.0	4.0	10.1	32.9	17.2	57.2	13.2	35.0	12.7	68.0	0.0	2.6	0.0	0.0	0.0	4.5	1.2	0.0	0.8	0.8	0.0	0.7
Max [Gy]	P.S.	27.1	49.6	72.1	66.0	51.7	66.6	26.2	56.6	44.4	69.8	0.0	44.5	0.2	0.0	0.1	46.9	45.2	0.1	5.4	12.2	0.4	29.5
	Std.	26.8	60.4	81.3	69.3	74.6	71.5	31.3	65.4	39.7	70.6	0.0	45.3	0.3	0.0	0.1	46.4	77.0	0.1	5.0	23.0	0.3	77.0
	FIDAO	27.3	58.9	80.5	68.9	73.2	71.6	32.1	65.8	40.3	70.5	0.0	45.4	0.3	0.0	0.1	46.4	77.6	0.1	5.2	23.0	0.3	77.6
Int. Dose	P.S.	2.8×10^6					6.6×10^6										3.1×10^6						
	Std.	2.7×10^6					8.0×10^6										2.9×10^6						
	FIDAO	2.7×10^6					8.0×10^6										3.0×10^6						

Head-and-neck

		OAR	Brainstem	Cerebellum	Chiasm	Normal Tissue	Larynx	Lt. Lens	Rt. Lens	Lips	Lt. Optic Nerve	Rt. Optic Nerve	Lt. Parotid	Rt. Parotid	Spinal Cord	Lt. Temp Lobe	Rt. Temp Lobe	Lt. TM Joint
Mean [Gy]	P.S.		8.9	9.5	15.4	8.6	30.9	0.3	0.4	22.1	6.5	5.7	13.4	12.1	11.8	5.9	7.9	35.5
	Std.		6.6	23.2	20.0	18.2	64.0	0.6	0.9	35.4	13.2	8.8	21.8	21.9	16.7	16.6	10.9	54.8
	FIDAO		6.7	23.0	20.7	18.1	64.0	0.6	1.0	35.1	13.4	9.0	22.1	22.0	17.0	16.5	11.2	54.5
Max [Gy]	P.S.		18.3	26.7	23.3	65.9	42.5	0.3	0.5	40.1	22.4	13.5	35.6	31.0	27.1	40.4	24.4	39.6
	Std.		26.0	67.5	29.5	81.4	70.0	0.7	1.2	65.5	52.6	26.5	59.4	60.0	37.5	66.7	40.6	63.3
	FIDAO		26.2	67.2	30.3	80.4	69.9	0.7	1.2	64.4	53.1	27.5	59.8	60.1	38.4	67.4	40.8	62.6

Int. Dose	P.S.	3.5×10^{6}
	Std.	5.7×10^{6}
	FIDAO	5.7×10^{6}

Appendix E – Supplemental Data for Chapter 5

This content of this appendix was previously published with the article "Patient-specific calibration of cone-beam computed tomography data sets for radiotherapy dose calculations and treatment plan assessment" by Michael MacFarlane, Daniel Wong, Douglas A. Hoover, Eugene Wong, Carol Johnson, Jerry J. Battista, and Jeff Z. Chen, *Journal of Applied Clinical Medical Physics*, **19** (2): 249-257 (2018). Permission to reproduce this article was granted by John Wiley and Sons and is provided in Appendix B.4.

Supplemental Table 5.1: Summary of Patient Treatment Information

No.	Primary Disease Site	Delivery Method	Re-planned After
1	Tongue	2 Coplanar 360° Arcs	18/35 Fxns
2	Mouth Floor	2 Coplanar 360° Arcs	9/30 Fxns
3	Right Neck	2 Coplanar 360° Arcs	27/35 Fxns
4	Tongue	2 Coplanar 360° Arcs	29/35 Fxns
5	Oropharynx	2 Coplanar 360° Arcs	17/35 Fxns
6	Mouth	2 Coplanar 180° Arcs	12/30 Fxns
7	Tonsils	2 Coplanar 360° Arcs	21/35 Fxns
8	Tonsils	2 Coplanar 360° Arcs	17/35 Fxns
9	Tongue	2 Coplanar 360° Arcs	14/35 Fxns
10	Tonsils	2 Coplanar 360° Arcs	26/35 Fxns
11	Tonsils	2 Coplanar 360° Arcs	20/35 Fxns
12	Tongue	2 Coplanar 360° Arcs	27/35 Fxns
13	Tongue	2 Coplanar 360° Arcs	24/35 Fxns
14	Neck	2 Coplanar 360° Arcs	21/35 Fxns
15	Nasal Cavity	2 Non-coplanar Arcs	17/30 Fxns

Abbreviations: Fxns, fractions.

Supplemental Table 5.2: Summary of the planning CT acquisition.

No.	Device	Acquisition Date	Energy [kV]	X-Ray Current [mA]	Exposure Time [ms]	Exposure [mAs]	Slices	Voxel Size [mm]
1	Brilliance Big Bore	11/27/2012	120	283	1060	300	146	1.01 x 1.01 x 3
2	Brilliance Big Bore	4/5/2016	120	245	1224	300	141	1.10 x 1.10 x 3
3	Brilliance Big Bore	5/15/2015	120	281	1068	300	135	1.00 x 1.00 x 3
4	Brilliance Big Bore	5/11/2016	120	242	1240	300	155	1.22 x 1.22 x 3
5	Brilliance Big Bore	8/14/2013	120	283	1060	300	126	1.02 x 1.02 x 3
6	Brilliance Big Bore	9/25/2013	120	281	1068	300	151	0.97 x 0.97 x 3
7	Brilliance Big Bore	12/9/2013	120	244	1230	300	140	1.09 x 1.09 x 3
8	Brilliance Big Bore	12/3/2013	120	281	1068	300	158	1.00 x 1.00 x 3
9	Brilliance Big Bore	1/27/2014	120	281	1068	300	136	0.93 x 0.93 x 3
10	Brilliance Big Bore	5/13/2014	120	283	1060	300	134	1.02 x 1.02 x 3
11	Brilliance Big Bore	6/8/2015	120	244	1230	300	120	1.18 x 1.18 x 3
12	Brilliance Big Bore	6/24/2015	120	208	1447	301	135	1.30 x 1.30 x 3
13	Brilliance Big Bore	4/11/2016	120	281	1068	300	140	0.93 x 0.93 x 3
14	Brilliance Big Bore	4/11/2016	120	283	1060	300	121	0.93 x 0.93 x 3
15	Brilliance Big Bore	9/23/2015	120	244	1230	300	124	1.05 x 1.05 x 3

Supplemental Table 5.3: Summary of the re-planning CT acquisition.

No.	Device	Acquisition Date	Energy [kV]	X-Ray Current [mA]	Exposure Time [ms]	Exposure [mAs]	Slices	Voxel Size [mm]
1	Brilliance Big Bore	1/8/2013	120	244	1230	300	153	1.20 x 1.20 x 3
2	Brilliance Big Bore	5/26/2016	120	244	1230	300	137	1.08 x 1.08 x 3
3	Brilliance Big Bore	7/8/2015	120	244	1230	300	167	1.13 x 1.13 x 3
4	Brilliance Big Bore	6/29/2016	120	244	1230	300	131	1.10 x 1.10 x 3
5	Brilliance Big Bore	9/19/2013	120	244	1230	300	158	1.13 x 1.13 x 3
6	Brilliance Big Bore	10/21/2013	120	281	1068	300	144	1.04 x 1.04 x 3
7	Brilliance Big Bore	1/28/2014	120	244	1230	300	156	1.19 x 1.19 x 3
8	Brilliance Big Bore	1/10/2014	120	281	1068	300	153	0.98 x 0.98 x 3
9	Brilliance Big Bore	2/28/2014	120	244	1230	300	137	1.16 x 1.16 x 3
10	Brilliance Big Bore	6/27/2014	120	281	1068	300	134	1.03 x 1.03 x 3
11	Brilliance Big Bore	7/24/2015	120	244	1230	300	146	1.05 x 1.05 x 3
12	Brilliance Big Bore	8/11/2015	120	281	1068	300	137	0.97 x 0.97 x 3
13	Brilliance Big Bore	5/26/2016	120	244	1230	300	143	1.15 x 1.15 x 3
14	Brilliance Big Bore	5/10/2016	120	281	1068	300	145	1.03 x 1.03 x 3
15	Brilliance Big Bore	11/3/2015	120	245	1224	300	125	1.11 x 1.11 x 3

Supplemental Table 5.4: Summary of the CBCT acquisition.

No.	Device	Acquisition Date	Energy [kV]	X-Ray Current [mA]	Exposure Time [ms]	Exposure [mAs]	Slices	Voxel Size [mm]
1	Clinac iX	1/8/2013	100	20	7000	140	70	0.65 x 0.65 x 2.5
2	Truebeam	5/26/2016	100	20	7450	149	93	0.51 x 0.51 x 2.0
3	Truebeam	7/15/2015	100	20	7450	149	93	0.51 x 0.51 x 2.0
4	Truebeam	7/5/2016	100	20	7500	150	93	0.51 x 0.51 x 2.0
5	Clinac iX	9/19/2013	100	20	7050	141	70	0.65 x 0.65 x 2.5
6	Truebeam	10/21/2013	100	20	7250	145	89	0.51 x 0.51 x 2.0
7	Clinac iX	1/28/2014	100	20	7000	140	70	0.65 x 0.65 x 2.5
8	Truebeam	1/10/2014	100	10	7200	72	70	0.49 x 0.49 x 2.5
9	Clinac iX	2/28/2014	100	10	7000	70	70	0.65 x 0.65 x 2.5
10	Clinac iX	6/26/2014	100	20	7250	145	70	0.65 x 0.65 x 2.5
11	Clinac iX	7/23/2015	100	20	6950	139	70	0.65 x 0.65 x 2.5
12	Clinac iX	8/11/2015	100	20	7200	144	70	0.65 x 0.65 x 2.5
13	Clinac iX	5/26/2016	100	10	7000	70	70	0.65 x 0.65 x 2.5
14	Clinac iX	5/10/2016	100	20	7200	144	70	0.65 x 0.65 x 2.5
15	Clinac iX	11/3/2015	100	20	7000	140	70	0.65 x 0.65 x 2.5

Appendix F – Curriculum Vitae

Michael J. MacFarlane, MSc

PhD Candidate – Medical Biophysics
University of Western Ontario
London ON, Canada

Home Address

██████ @uwo.ca

Work Address

EDUCATION

Candidate for Doctor of Philosophy   *Sept. 2014 – Apr. 2019*
Medical Biophysics
University of Western Ontario, London ON.
Supervisors: Dr. Jeff Z. Chen & Dr. Jerry J. Battista
Thesis Title: Towards on-line plan adaptation of unified intensity-modulated arc therapy using a
*   fast-direct aperture optimization algorithm.*

Master of Science   *Sept. 2014 – Aug. 2018*
Clinical Medical Biophysics (CAMPEP Accredited)
University of Western Ontario, London ON.
GPA: 3.97

Bachelor of Science   *Sept. 2009 – May 2014*
Honours Mathematical Physics (Co-operative Program)
University of Waterloo, Waterloo ON.
GPA: 2.68

EMPLOYMENT

Teaching Assistant – linac Quality Assurance Program   *Jan. 2016 – Aug. 2018*
University of Western Ontario, London ON
Responsibilities: *Train and coordinate students with performing mechanical and dosimetric quality assurance on medical linear accelerators (Varian TrueBeam and iX machines). Resolve machine interlocks or out-of-tolerance measurements during QA.*

Medical Physics Assistant (Co-operative Work Placement)   *Sept. 2011 – Aug. 2014*
London Regional Cancer Program, London ON
Responsibilities: *Develop scripts in Pinnacle that create, evaluate and help visualize external beam radiotherapy treatment plans (e.g. automatic VMAT planning for head-and-neck, prostate, lung SBRT; report of DVH metrics and NTCP calculations). Lead research on two projects: intensity-modulated grid therapy & UIMAT. Perform patient plan QA with MapCheck and ArcCheck phantoms. Performed QA on medical linear accelerators (Varian Truebeam, iX, & 2100C). Created a paperless system for reporting linac QA.*

Research Programmer (Co-operative Work Placement)   *Jan. 2011 – May 2014*
Communication Research Center, Ottawa ON
Responsibilities: *Develop video processing software for a prototype 3D television. Prepare documentation and visual demonstrations for potential investors.*

RECOGNITIONS & AWARDS

Doctoral Research Award   *May 2017*
Canadian Institutes of Health Research (CIHR)
Monetary Value: $105,000 (CAD)

Top Oral Presentation Award   *July 2014*
Canadian Organization of Medical Physicist (COMP) – 2014 Annual Scientific Meeting
Monetary Value: $400 (CAD)

Top Poster Presentation Award   *July 2014*
Cancer Research and Technology Transfer (CaRTT) – Annual Research & Education Day
Monetary Value: $100 (CAD)

PUBLICATIONS & PROCEEDINGS

Papers:
- MacFarlane M, Hoover D, Wong E, et al. "Improving unified intensity-modulated arc therapy (UIMAT) for wider clinical application". (Working Paper)
- MacFarlane M, Hoover D, Wong E, et al. "A fast inverse direct aperture optimization algorithm for volume-modulated arc therapy". (Working Paper)
- MacFarlane M, Hoover D, Wong E, et al. "A fast inverse direct aperture optimization algorithm for intensity-modulated radiation therapy." *Med. Phys. 2019; 46 (3): 1127-39.*
- MacFarlane M, Wong D, Hoover D, et al. "Patient-specific calibration of cone-beam computed tomography data sets for radiotherapy dose calculations and treatment plan assessment". *J. Appl. Clin. Med. Phys. 2018; 19(2): 249-57.*
- MacFarlane M, Hoover D, Wong E, et al. "Evaluation of unified intensity-modulated arc therapy for the radiotherapy of head-and-neck cancer". *Radiother. Oncol. 2016; 119 (2): 331-336.*
- Xhaferllari I, Chen J, MacFarlane M, et al. "Dosimetric planning study of respiratory-gated volumetric modulated arc therapy for early-stage lung cancer with stereotactic body radiation therapy". *Pract. Rad. Oncol. 2015; 5(3): 156-61*
- Hoover D, MacFarlane M, Wong E, et al. "Feasibility of a unified approach to intensity-modulated radiation therapy and volume-modulated arc therapy optimization and delivery". *Med. Phys. 2015; 42(2): 726-734.*

National & International Conference Proceedings:
- MacFarlane M, Hoover D, Wong E, et al. "Improving Unified Intensity Modulated Arc Therapy (UIMAT) for Wider Clinical Application. (ePoster)" *AAPM 2018 Annual Scientific Meeting Proceedings.*
- MacFarlane M, Hoover D, Wong E, et al. "Preliminary Results from a Fast Inverse Direct Aperture Optimization (FIDAO) Algorithm. (ePoster)" *AAPM 2018 Annual Scientific Meeting Proceedings.*

- MacFarlane M, Hoover D, Wong E, et al. "Feasibility of a Fast Inverse Direct Aperture Optimization Algorithm Using Matrix Inversion. (ePoster)" *AAPM 2017 Annual Scientific Meeting Proceedings.*
- MacFarlane M, Hoover D, Wong E, et al. "Patient-specific calibration of cone-beam computed tomographic (CBCT) image sets for on-line dose tracking and plan assessment. (Oral – Best in Physics)" *COMP 2016 Annual Scientific Meeting Proceedings.*
- MacFarlane M, Lam J, Dar AR, et al. "Feasibility Study of Intensity-Modulated Grid-Therapy for Bulky Lung Tumors. (Poster)" *Astro 2015 Annual Meeting Proceedings.*
- MacFarlane M, Hoover D, Wong E, et al. "Evaluation of unified intensity-modulated arc therapy (UIMAT) for the treatment of head-and-neck cancer. (Oral)" *IUPESM 2015 World Congress Proceedings.*
- Chen J, MacFarlane M, Wong E, et al. "Unified Optimization and Delivery of Intensity-modulated Radiation Therapy and Volume-modulated Arc Therapy. (Oral – Best in Physics)" *COMP 2014 Annual Scientific Meeting Proceedings.*

RELEVANT TRAINING & EXPERIENCE

Anatomy and Radiology Contouring Bootcamp for Radiation Oncology Residents　　　　*Oct 2018*
Western University, London ON
Topics: *Delineating target volumes, areas at risk for subclinical disease & critical structures.*

AAPM 2018 Summer School　　　　*July 2018*
Vanderbilt University, Nashville TN
Topics: *Image Guidance in Radiation Therapy: Techniques, Accuracy, and Limitations.*

Journal Club Member & Coordinator (2015-2016)　　　　*Sept. 2015 – Present*
London Regional Cancer Program, London ON
Coordinated and chaired presentations on student work and recent publications.

PROFESSIONAL ORGANIZATIONS

American Association of Physicist in Medicine　　　　*Jan. 2016 – Present*
Student Member

Canadian Organization of Medical Physicists　　　　*Mar. 2015 – Present*
Student Member